Inorganic Carbon System Dynamics of Southern Hudson Bay and James Bay

by

Nicholas Decker

A Thesis submitted to the Faculty of Graduate and Postdoctoral Studies of the University of Manitoba in partial fulfilment of the requirements of the degree of

Master of Science in Geography

Department of Environment and Geography
University of Manitoba
Winnipeg

Supervised by

Dr. Kristina Brown
Assistant Professor
Centre for Earth Observation Sciences
Department of Environment and Geography
University of Manitoba
Winnipeg, MB, Canada

Dr. Tim Papakyriakou
Professor
Centre for Earth Observation Sciences
Department of Environment and Geography
University of Manitoba
Winnipeg, MB, Canada

Advisory Committee

Dr. Dave Capelle
Research Scientist
Freshwater Institute
Fisheries and Oceans Canada
Winnipeg, MB, Canada
&
Adjunct Professor
Department of Environment and Geography
University of Manitoba
Winnipeg, MB, Canada

Dr. Zou Zou Kuzyk
Professor
Centre for Earth Observation Sciences
Department of Earth Sciences
University of Manitoba
Winnipeg, MB, Canada

Thesis Abstract

Driven by the difference in the partial pressure of CO_2 (pCO_2) between the atmosphere and the ocean, 26% of anthropogenic carbon dioxide (CO_2) emissions have been absorbed by the world's oceans. The Arctic Ocean is responsible for 5-14% of the ocean CO_2 sink despite accounting for 4.3% of the global surface ocean area due to its cool temperatures and low salinity relative to other oceans. As CO_2 is absorbed by seawater, it forms carbonic acid resulting in reduced carbonate ion availability and lower pH. Increasing anthropogenic CO_2 emissions have impacted seawater carbonate chemistry, resulting in acidic conditions in which calcifying organisms have difficulties forming hard structures. The peripheral Arctic seas Southern Hudson Bay and James Bay (SHB-JB) are experiencing rapid climate change, including decreased sea ice cover, altered river runoff, and increased temperatures. However, our ability to assess ecosystem response to changing Arctic conditions is limited as SHB-JB remain understudied with respect to the inorganic carbon system.

The objective of this thesis was to evaluate the marine inorganic carbon system of SHB-JB using three years (2021–2023) of ship-based measurements. Continuous surface mixed layer measurements indicated that SHB-JB were weak sources of CO_2 to the atmosphere during August. Temperature was the main driver of surface water pCO_2, while dissolved inorganic carbon (DIC) and total alkalinity (TA) decreased with proximity to river inflows. Saturation state (Ω) indicated undersaturation ($\Omega<1$) of aragonite across James Bay, while calcite undersaturation was restricted to the Moose and Eastmain River estuaries. Freshwater impacts on seawater inorganic carbon differed based on watershed properties; rivers entering eastern James Bay were more acidic than rivers entering western James Bay, which caused a greater reduction in coastal Ω. This difference reflects watershed geology; western James Bay is underlain by carbonate till, whereas eastern James Bay is underlain by silicate bedrock. The results of this thesis provide a baseline assessment of summertime marine inorganic carbon and acidification state within James Bay while supporting previous carbon system studies in Hudson Bay. Continued monitoring of the SHB-JB carbonate system is required to provide insight into how Arctic ecosystems respond to advancing climate change.

Land Acknowledgement

This research was conducted on campus at the University of Manitoba, located on the original lands of Anishinaabeg, Ininiwak, Anisininewuk, Dakota Oyate, Dene, and Inuit, and on the National Homeland of the Red River Métis. Field work for this project was conducted in Hudson Bay and James Bay, the home of the Inuit people of Inuit Nunangat and the Omushkego Cree communities of Northern Ontario.

The University of Manitoba recognizes that the Treaties signed on these lands are a lifelong, enduring relationship, and we are dedicated to upholding their spirit and intent. We acknowledge the harms and mistakes of the past and the present. With this understanding, we commit to supporting Indigenous excellence through active Reconciliation, meaningful change, and the creation of an environment where everyone can thrive. Our collaboration with Indigenous communities is grounded in respect and reciprocity and this guides how we move forward as an institution.

Personal Acknowledgements

First and foremost, thank you to my partner Kira Peters, who is always pushing me to be the best I can. I would like to thank my advisors Dr. Brown and Dr. Papakyriakou for their continued guidance, support, and mentorship throughout this project. Their expertise, thoughtful feedback, and motivation were invaluable to the development of this work. This project would not have been possible without Dr. Brown encouraging me to set and achieve realistic but challenging goals. I am also grateful to my committee members, Dr. Capelle and Dr. Kuzyk, for their time and insight. I would like to thank my colleagues and friends at the U of M and CEOS for their encouragement, discussions, and camaraderie throughout my graduate studies. Thank you to Kate Yezhova for assisting with field work, and Dr. Burgers and Rachel Mandryk from DFO-FWI for assisting with laboratory analysis. Finally, I am deeply grateful to my family (Alexandra, Colleen, Frank, and Kathleen) and friends for their patience, encouragement, and support.

Table of Contents

List of Figures and Tables

Chapter 1

Chapter 2

Chapter 3

Chapter 4

Chapter 1: Introduction

1.1 Motivation

Anthropogenic carbon dioxide (CO_2) emissions are increasing the concentration of CO_2 in the atmosphere at an unprecedented rate, resulting in accelerated uptake of CO_2 by ocean surface waters (Friedlingstein et al., 2023). As CO_2 dissolves into the ocean, it reacts with water to form carbonic acid. The formation of carbonic acid decreases ocean pH and the saturation state (Ω) of carbonate ($CaCO_3$) minerals, notably calcite and aragonite (Ω_{Cal} + Ω_{Arag}; Zeebe & Wolf-Gladrow, 2001). Coastal marine ecosystems are home to calcifying organism such as snails, mollusks, corals, and bivalves (Comeau et al., 2012). A drop in both ocean pH and Ω_{Cal} + Ω_{Arag} can pose a threat to these organisms; however, the specific response varies by species, and is not well understood (Azevedo et al., 2015). The combination of the Arctic Ocean's cool temperatures, freshened surface waters, and increased CO_2 uptake contribute to increased sensitivity to carbonate mineral undersaturation (Yamamoto-Kawai et al., 2009), making continued anthropogenic CO_2 emissions potentially hazardous for marine calcifers (Azevedo et al., 2015; Terhaar et al., 2021).

The contemporary CO_2 sink status, pH, and Ω conditions of the Arctic Ocean are uniquely sensitive to change because of the combination of cold water with lower salinity (relative to other oceans), due in part by a disproportionate amount of river inflow for the size of the ocean basin (Azetsu-Scott et al., 2010). River input is a significant source of dissolved and particulate carbon to the ocean and climate change has resulted in increased terrestrial carbon transport via rivers, which has had significant consequences on Arctic shelf seas (McGuire et al., 2009). Additional terrestrial carbon delivered by rivers, particularly organic carbon, increases the partial pressure of CO_2 (pCO_2) and decreases pH in coastal surface waters upon degradation (Capelle et al., 2020; Duarte et al., 2013). Large freshwater input will also stratify the ocean by suppressing vertical mixing, contributing to observations of lowered pH and Ω, as well as increased alkalinity in bottom waters as organic carbon (both autochthonous and allochthonous) is remineralized at depth (Capelle et al., 2020; Carmack et al., 2016). Surface water experiences decreased pH and reduced buffering capacity as alkalinity decreases, weakening seawater's resistance to further decreases in pH with increasing CO_2 (Zeebe & Wolf-Gladrow, 2001). In bottom waters, reduced pH and carbonate mineral saturation state creates corrosive conditions, potentially becoming dangerous to calcifying organisms (Lischka et al., 2011; Zeebe & Wolf-Gladrow, 2001).

Monitoring the response of seawater pCO_2, pH and Ω, as well as the biogeochemical properties of inflowing river water, is critical to understanding changes in the region's CO_2 source or sink status and the susceptibility of coastal waters to becoming increasingly acidic with ongoing climate change (Bauer et al., 2013; Duarte et al., 2013; Tank et al., 2012; Vonk & Gustafsson, 2013).

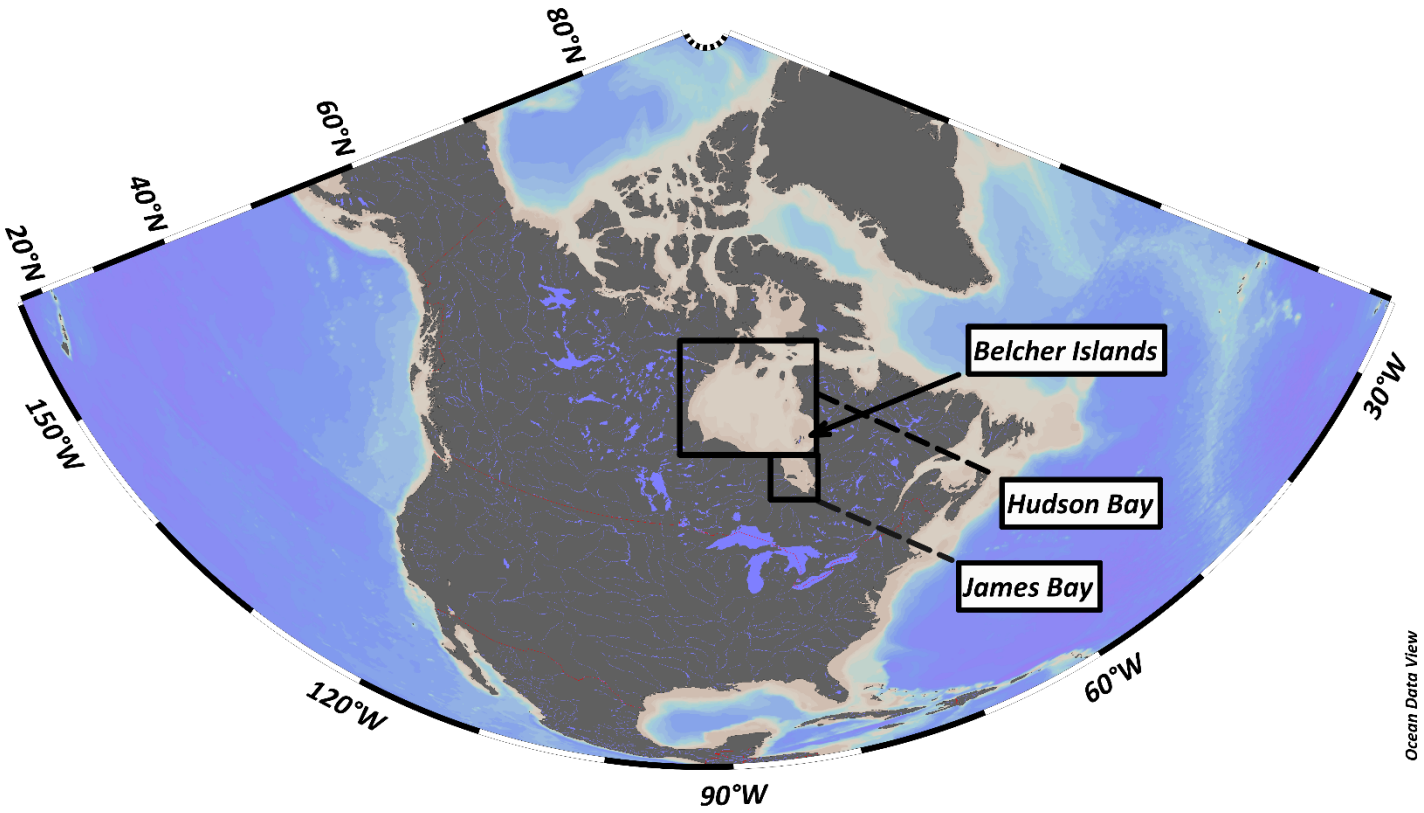

Figure 1.1: Hudson Bay, James Bay, and The Belcher Islands.

Like the broader Arctic Ocean, the sub-Arctic seas of Southern Hudson Bay and James Bay (SHB-JB; Figure 1.1), also receive a disproportionate amount of river input relative to their size, making them similarly sensitive to shifts in pCO_2, pH and Ω with continued freshening (Azetsu-Scott et al., 2014; Capelle et al., 2020; Déry et al., 2005). Additionally, the permafrost-laden peatlands of the Hudson Bay Lowlands (HBL) lie adjacent to SHB-JB. The HBL are the world's second largest peatland complex, which hold a significant proportion of the global store of terrestrial permafrost carbon, estimated at 33 Gt C (as partially decomposed vegetation; Packalen et al., 2014). Ongoing permafrost thaw, forest fires, and/or other consequences of climate change, result in increased carbon emissions from SHB-JB either through direct evasion to the atmosphere as carbon dioxide (CO_2) and methane (CH_4), and/or by relocation of the carbon to the ocean by riverine transport, potentially triggering a strong positive climate feedback loop (Natali et al., 2021; Schuur et al., 2015; Virkkala et al., 2025; Vonk & Gustafsson, 2013). Further degradation of terrestrial carbon in the coastal ocean not only weakens the ocean's carbon uptake capacity, but also elevates the risk of these waters becoming more acidic (Bauer et al., 2013; Duarte et al., 2013; McGuire et al., 2009; Vonk & Gustafsson, 2013). In

general, SHB-JB remain understudied; previous work in Hudson Bay has described large-scale patterns in carbonate chemistry and riverine alkalinity supply (e.g., Azetsu-Scott et al. 2014; Capelle et al. 2020; Granskog et al. 2011), but no comprehensive examination of the marine inorganic carbon system has been conducted in James Bay.

This thesis reports the first ship-based examination of the James Bay carbonate system and provides new insight into the Hudson Bay carbonate system. Further, this thesis presents the first multi-year data set from the region in the late summer (August), contrasting with previously published datasets from the spring (May - July) and fall (September). Using physical and chemical oceanographic data collected, this thesis aims to characterize and explain the distribution of key carbonate system variables within Southern Hudson Bay and James Bay to fill a regional knowledge gap and contribute to the broader understanding of how high-latitude coastal systems respond to increasing atmospheric anthropogenic CO_2.

1.2 Thesis Objectives

The objective of this thesis is to evaluate the inorganic carbon system dynamics within James Bay and Southern Hudson Bay through an examination of the main physical and biogeochemical factors influencing its behaviour. This main objective will be met through the following sub-objectives:

- Describe the surface water distribution of the partial pressure of carbon dioxide (pCO_2), including the region's status as a CO_2 source or sink in relation to the atmosphere, and the major factors that contribute to its variability.
- Assess the factors that determine the distribution of key carbonate system variables such as calcium carbonate saturation state (Ω), pH, DIC, and TA and assess whether the waters in the region present corrosive conditions for calcifying organisms.

1.3 Thesis Outline

This thesis is composed of five chapters; Chapter 1 and 2 provide context and rationale for the thesis while Chapters 3 through 5 summarise findings in the form of journal articles. *Chapter 2: Background* provides foundational carbonate system information required for understanding the remaining chapters, along with a comprehensive overview of our knowledge of Hudson Bay's carbonate system.

The first research paper, *Chapter 3: Seawater CO_2 Uptake and Emissions,* examines the distribution and dominant controls on surface seawater CO_2 in southern Hudson Bay and James Bay. Additionally, this chapter includes air–sea CO_2 exchange calculations to provide insight into the direction and magnitude of CO_2 being exchanged between the ocean and atmosphere over the study period. This manuscript addresses objective 1 and is prepared for publication in *Elementa: Science of the Anthropocene*.

Following this, *Chapter 4: Riverine controls on widespread carbonate mineral undersaturation in James Bay* addresses objective 2. Total alkalinity (TA) and total dissolved inorganic carbon (DIC) were used to calculate Ω and pH and assess the carbonate mineral saturation state of the region. This section examines the distribution as well as physical and biogeochemical controls on Ω and pH within Southern Hudson Bay and James Bay. This chapter reports the first observations of surface water aragonite undersaturation within the study region which is an observation attributed to the region's large freshwater influxes.

Lastly, *Chapter 5: Summary and Conclusions* provides a summary of the previous chapter's main results. This section identifies the limitations of our work, areas requiring further attention, and additional context for how our results contribute to furthering our understanding of the inorganic carbon system. Contributions of co-authors to each of the thesis chapters are stated in Appendix A.

1.4 References

Azetsu-Scott, K., Clarke, A., Falkner, K., Hamilton, J., Jones, E. P., Lee, C., Petrie, B., Prinsenberg, S. J., Starr, M., & Yeats, P. (2010). Calcium carbonate saturation states in the waters of the Canadian Arctic Archipelago and the Labrador Sea. *Journal of Geophysical Research*, *115*(C11021). https://doi.org/10.1029/2009JC005917

Azetsu-Scott, K., Starr, M., Mei, Z. P., & Granskog, M. (2014). Low calcium carbonate saturation state in an Arctic inland sea having large and varying fluvial inputs: The Hudson Bay system. *Journal of Geophysical Research: Oceans*, *119*(9), 6210–6220. https://doi.org/10.1002/2014JC009948

Azevedo, L. B., De Schryver, A. M., Hendriks, A. J., & Huijbregts, M. A. J. (2015). Calcifying species sensitivity distributions for ocean acidification. *Environmental Science and Technology*, *49*(3), 1495–1500. https://doi.org/10.1021/es505485m

Bauer, J. E., Cai, W. J., Raymond, P. A., Bianchi, T. S., Hopkinson, C. S., & Regnier, P. A. G. (2013). The changing carbon cycle of the coastal ocean. *Nature 2013 504:7478*, *504*(7478), 61–70. https://doi.org/10.1038/nature12857

Capelle, D. W., Kuzyk, Z. Z. A., Papakyriakou, T., Guéguen, C., Miller, L. A., & Macdonald, R. W. (2020). Effect of terrestrial organic matter on ocean acidification and CO_2 flux in an Arctic shelf sea. *Progress in Oceanography*, *185*. https://doi.org/10.1016/j.pocean.2020.102319

Carmack, E. C., Yamamoto-Kawai, M., Haine, T. W. N., Bacon, S., Bluhm, B. A., Lique, C., Melling, H., Polyakov, I. V., Straneo, F., Timmermans, M. L., & Williams, W. J. (2016). Freshwater and its role in the Arctic Marine System: Sources, disposition, storage, export, and physical and biogeochemical consequences in the Arctic and global oceans. *Journal of Geophysical Research: Biogeosciences*, *121*(3), 675–717. https://doi.org/10.1002/2015JG003140

Comeau, S., Alliouane, S., & Gattuso, J. P. (2012). Effects of ocean acidification on overwintering juvenile Arctic pteropods Limacina helicina. *Marine Ecology Progress Series*, *456*, 279–284. https://doi.org/10.3354/MEPS09696

Déry, S. J., Stieglitz, M., Mckenna, E. C., & Wood, E. F. (2005). *Characteristics and Trends of River Discharge into Hudson, James, and Ungava Bays, 1964-2000*.

Duarte, C. M., Hendriks, I. E., Moore, T. S., Olsen, Y. S., Steckbauer, A., Ramajo, L., Carstensen, J., Trotter, J. A., & McCulloch, M. (2013). Is Ocean Acidification an Open-Ocean Syndrome? Understanding Anthropogenic Impacts on Seawater pH. *Estuaries and Coasts*, *36*(2), 221–236. https://doi.org/10.1007/s12237-013-9594-3

Friedlingstein, P., O'Sullivan, M., Jones, M. W., Andrew, R. M., Bakker, D. C. E., Hauck, J., Landschützer, P., Le Quéré, C., Luijkx, I. T., Peters, G. P., Peters, W., Pongratz, J., Schwingshackl, C., Sitch, S., Canadell, J. G., Ciais, P., Jackson, R. B., Alin, S. R., Anthoni, P.,

… Zheng, B. (2023). Global Carbon Budget 2023. *Earth System Science Data*, *15*(12), 5301–5369. https://doi.org/10.5194/essd-15-5301-2023

Lischka, S., Büdenbender, J., Boxhammer, T., & Riebesell, U. (2011). Impact of ocean acidification and elevated temperatures on early juveniles of the polar shelled pteropod Limacina helicina: Mortality, shell degradation, and shell growth. *Biogeosciences*, *8*(4), 919–932. https://doi.org/10.5194/bg-8-919-2011

McGuire, A. D., Anderson, L. G., Christensen, T. R., Dallimore, S., Guo, L., Hayes, D. J., Heimann, M., Lorenson, T. D., Macdonald, R. W., & Roulet, N. (2009). Sensitivity of the carbon cycle in the Arctic to climate change. *Ecological Monographs*, *79*(4), 523–555. https://doi.org/10.1890/08-2025.1

Natali, S. M., Holdren, J. P., Rogers, B. M., Treharne, R., Duffy, P. B., Pomerance, R., & MacDonald, E. (2021). Permafrost carbon feedbacks threaten global climate goals. *Proceedings of the National Academy of Sciences*, *118*(21), e2100163118. https://doi.org/10.1073/pnas.2100163118

Packalen, M. S., Finkelstein, S. A., & McLaughlin, J. W. (2014). Carbon storage and potential methane production in the Hudson Bay Lowlands since mid-Holocene peat initiation. *Nature Communications*, *5*. https://doi.org/10.1038/ncomms5078

Schuur, E. A. G., McGuire, A. D., Schädel, C., Grosse, G., Harden, J. W., Hayes, D. J., Hugelius, G., Koven, C. D., Kuhry, P., Lawrence, D. M., Natali, S. M., Olefeldt, D., Romanovsky, V. E., Schaefer, K., Turetsky, M. R., Treat, C. C., & Vonk, J. E. (2015). Climate change and the permafrost carbon feedback. *Nature*, *520*(7546), 171–179. https://doi.org/10.1038/nature14338

Tank, S. E., Raymond, P. A., Striegl, R. G., McClelland, J. W., Holmes, R. M., Fiske, G. J., & Peterson, B. J. (2012). A land-to-ocean perspective on the magnitude, source and implication of DIC flux from major Arctic rivers to the Arctic Ocean. *Global Biogeochemical Cycles*, *26*(4). https://doi.org/10.1029/2011GB004192

Terhaar, J., Torres, O., Bourgeois, T., & Kwiatkowski, L. (2021). Arctic Ocean acidification over the 21st century co-driven by anthropogenic carbon increases and freshening in the CMIP6 model ensemble. *Biogeosciences*, *18*(6), 2221–2240. https://doi.org/10.5194/bg-18-2221-2021

Virkkala, A.-M., Rogers, B. M., Watts, J. D., Arndt, K. A., Potter, S., Wargowsky, I., Schuur, E. A. G., See, C. R., Mauritz, M., Boike, J., Bret-Harte, M. S., Burke, E. J., Burrell, A., Chae, N., Chatterjee, A., Chevallier, F., Christensen, T. R., Commane, R., Dolman, H., … Natali, S. M. (2025). Wildfires offset the increasing but spatially heterogeneous Arctic–boreal CO2 uptake. *Nature Climate Change*, *15*(2), 188–195. https://doi.org/10.1038/s41558-024-02234-5

Vonk, J. E., & Gustafsson, Ö. (2013). Permafrost-Carbon Complexities. *Nature Geoscience*, *6*, 675–676.

Yamamoto-Kawai, M., McLaughlin, F. A., Carmack, E. C., Nishino, S., & Shimada, K. (2009). Aragonite Undersaturation in the Arctic Ocean: Effects of Ocean Acidification and Sea Ice Melt. *Science*, *326*(5956), 1098–1100. https://doi.org/10.1126/science.1174190

Zeebe, R. E., & Wolf-Gladrow, D. (2001). *CO_2 in seawater: Equilibrium, Kinetics, Isotopes* (D. Halpern, Ed.). Elsevier.

Chapter 2: Background Information

2.1. The Marine Inorganic Carbon System

This section provides an overview of the current knowledge of the oceanic carbonate system including its components, global and regional controls, and the mechanisms of ocean carbonate system change including ocean acidification. In an effort to reach a state of equilibrium, the ocean and atmosphere will exchange CO_2 to reach a state where the dissolved CO_2 within the surface ocean is equivalent to the partial pressure of CO_2 in the atmosphere above it (AMAP, 2013). This reaction is represented by the equation (Zeebe & Wolf-Gladrow, 2001):

Eq. 2.1 $$CO_{2(g)} \rightleftharpoons CO_{2(aq)} + H_2O_{(l)} \rightleftharpoons H_2CO_3^* \rightleftharpoons HCO_3^- + H^+ \rightleftharpoons CO_3^{2-} + 2H^+$$

Equation 2.1 illustrates the processes that occur when CO_2 dissolves into the ocean. Upon dissolution, CO_2 reacts with water to form carbonic acid (H_2CO_3; Zeebe & Wolf-Gladrow, 2001). It is difficult to differentiate between aqueous CO_2 and carbonic acid analytically, so they are expressed together as the hypothetical species $H_2CO_3^*$. This species is represented by the equation (Zeebe & Wolf-Gladrow, 2001):

Eq. 2.2 $$H_2CO_3^* = CO_{2(aq)} + H_2CO_3$$

Upon formation in water, carbonic acid will behave as a weak acid, dissociating to produce bicarbonate (HCO_3^-), carbonate (CO_3^{2-}), and hydrogen (H^+) ions depending on the solution pH (Eq 2.1). These reversible CO_2 equilibria define the activity of H^+ $\{H^+\}$ in seawater, but they can also be expressed as stoichiometric equilibria that relate to measured concentrations of ions in solution defined at specific temperature, salinity, and pressure (Table 2.1).

Table 2.1: *Carbonate system equilibrium reactions and their respective stoichiometric equilibrium constants under defined temperature, salinity, and pressure conditions (Zeebe & Wolf-Gladrow, 2001)*

$\boldsymbol{CO_{2(g)} + H_2O \leftrightarrow H_2CO_3^*}$	$K_0 = \frac{[H_2CO_3^*]}{pCO_2}$
$\boldsymbol{H_2CO_3^* \leftrightarrow H^+ + HCO_3^-}$	$K_1^* = \frac{[H^+][HCO_3^-]}{[H_2CO_3^*]}$
$\boldsymbol{HCO_3^- \leftrightarrow H^+ + CO_3^{2-}}$	$K_2^* = \frac{[H^+][CO_3^{2-}]}{[HCO_3^-]}$

In each of these equations, K_x represents a stoichiometric equilibrium constant for the specific reaction, pCO_2 is the partial pressure of CO_2 in seawater, and [x] denotes the concentration of an ion within a solution (Zeebe & Wolf-Gladrow, 2001). Stoichiometric equilibrium constants are defined for specific temperature, pressure, and salinity conditions, and are directly related to the ion concentration in solution under those physical conditions. Given stoichiometric equilibrium constants (K_1^*, K_2^*) and any two of the six components of the carbonate system (detailed below), the remaining variables may be calculated. The measurable components of the carbonate system are as follows:

- Dissolved Inorganic Carbon (DIC), the total amount of inorganic carbon expressed as the sum of the concentrations of all inorganic carbon species:

  Eq. 2.3 $$DIC = [CO_2] + [HCO_3^-] + [CO_3^{2-}]$$

- Total Alkalinity (TA), the total effective charge of the solution. The exact composition of alkalinity changes based on the dominant ionic species in solution, but it can broadly be explained as the capacity for the water to resist changes in pH as protons are added:

  Eq. 2.4 $$TA = [HCO_3^-] + 2[CO_3^{2-}] + [B(OH)_4^-] + [OH^-] - [H^+] + minor\ components$$

- pH, the negative log concentration of hydrogen ions (here measured on the Total scale)

  Eq. 2.5 $$pH = -\log[H^+]_T$$

- pCO_2, the partial pressure of carbon dioxide within the water, where partial pressure refers to the pressure of CO_2 in the gas phase in equilibrium with the sample of water:

  Eq. 2.6 $$pCO_2 = \frac{[H_2CO_3^*]}{K_0}$$

  - fCO_2, the fugacity of the carbon dioxide in the water, is the amount of CO_2 in the surface ocean. Fugacity and partial pressure are similar in concept and measurement. Because of this, fugacity and partial pressure may be used interchangeably for most applications. Fugacity is typically ~3 to 4‰ smaller than the partial pressure over a temperature range 0 – 30°C.

Oceanographers commonly use TA and DIC to calculate the other components of the system defined in equation 2.1, as these variables can be precisely measured and exhibit conservative behavior in relation to temperature, salinity, and pressure (Dickson et al., 2007). The conservative nature of these variables under changing temperature and pressure makes them ideal for laboratory analyses, where temperature and pressure conditions are not impacting the measurement. By contrast, pH and pCO_2/fCO_2 analyses yield concentration values that are temperature and pressure dependant and thus must be measured in situ (Dickson et al., 2007). Together, TA, DIC, and stoichiometric equilibrium constants (defined for various temperature, salinity, and pressure conditions in the global ocean) may be used to calculate the remaining carbonate system variables (pCO_2 and pH) as well as variables important to monitoring ocean acidification (Ω).

2.1.1. Ocean Acidification

Ocean acidification occurs as a result of changes in the ocean's chemistry due to increasing seawater CO_2 concentrations (AMAP, 2018). As CO_2 concentrations in the ocean's surface waters are also increased by natural processes, anthropogenic ocean acidification is defined as the component of pH reduction caused by human activity (AMAP, 2018). Since the beginning of the industrial revolution (~1750 Common Era; CE), the global surface ocean pH has been reduced by 0.1 units (Jiang et al., 2019). Due to low water temperature and salinity, the Arctic Ocean is uniquely sensitive to changing acidity and may see a surface water pH reduction of up to 0.5 units by 2100 CE (IPCC RCP8.5; AMAP, 2018) which is a much faster rate than the global surface ocean (0.3; IPCC RCP8.5; Jiang et al., 2019). Acidifying conditions are linked to the health of the ecosystem through the saturation state (Ω) of carbonate minerals, aragonite and calcite ($CaCO_3$), a mineral used by many organisms to form their hard structures (AMAP, 2013; Azetsu-Scott et al., 2014; Azevedo et al., 2015). Saturation state is calculated as a product of the concentration of calcium (Ca^{2+}) and carbonate (CO_3^{2-}) ions in solution divided by K_{SP}, the equilibrium solubility product (Zeebe & Wolf-Gladrow, 2001):

Eq. 2.7 $$\Omega = \frac{[Ca^{2+}][CO_3^{2-}]}{K_{SP}}$$

K_{SP} may be estimated as a product of the saturation concentrations of Ca^{2+} and CO_3^{2-} for a given temperature, pressure, and salinity (Mucci et al., 1989):

Eq. 2.8 $$K_{SP} = [Ca^{2+}]_{sat}[CO_3^{2-}]_{sat}$$

Therefore, when $[Ca^{2+}]$ and $[CO_3^{2-}]$ are at their saturation concentrations (i.e., $[Ca^{2+}][CO_3^{2-}] = [Ca^{2+}]_{sat}[CO_3^{2-}]_{sat}$), Ω = 1. When seawater Ω is greater than one (Ω > 1), water is

said to be 'saturated' with respect to $CaCO_3$. When seawater is 'undersaturated' with respect to $CaCO_3$ ($\Omega < 1$), calcifers may struggle to form their hard structures. However, specific responses to acidifying conditions vary by species (Azetsu-Scott et al., 2014; Azevedo et al., 2015). The $CaCO_3$ saturation state (Ω; Eq. 2.7) decreases when CO_2 dissolves into seawater (Eq 2.1), and carbonate ions in solution (CO_3^{2-}) are sacrificed to consume protons (H^+) released by carbonic acid dissolution (see equations in Table 1). Thus, an increase in aqueous CO_2 increases the solubility of carbonate minerals (aragonite and calcite) as modeled by the following reaction (Jutterström & Anderson, 2005):

Eq. 2.9 $$CaCO_{3(s)} + CO_{2(aq)} + H_2O \rightleftharpoons Ca^{2+} + 2HCO_3^-$$

Plotting the equations from Table 1 provides insights into the relationship between Ω and pH (Figure 2.1). As CO_2 is dissolved into seawater, protons are added to solution, the proportion of CO_3^{2-} decreases as HCO_3^- increases (Eq. 2.1), and seawater pH drops (see Eq. 2.5). The effects of temperature and salinity upon the equilibrium concentrations of inorganic carbon species may be visualized by altering the temperature and salinity at which stoichiometric equilibrium constants (K_1^* and K_2^*) are calculated, as represented by the Bjerrum plot shown in Figure 2.1. Stoichiometric equilibrium constants may be interpreted as the point where the relative concentration of two species is equal (i.e., the intersection of two identically coloured lines). When temperature and salinity decrease, the pH at which the K_1^* and K_2^* are located shifts correspondingly, resulting in a change in relative concentration of each carbonate species.

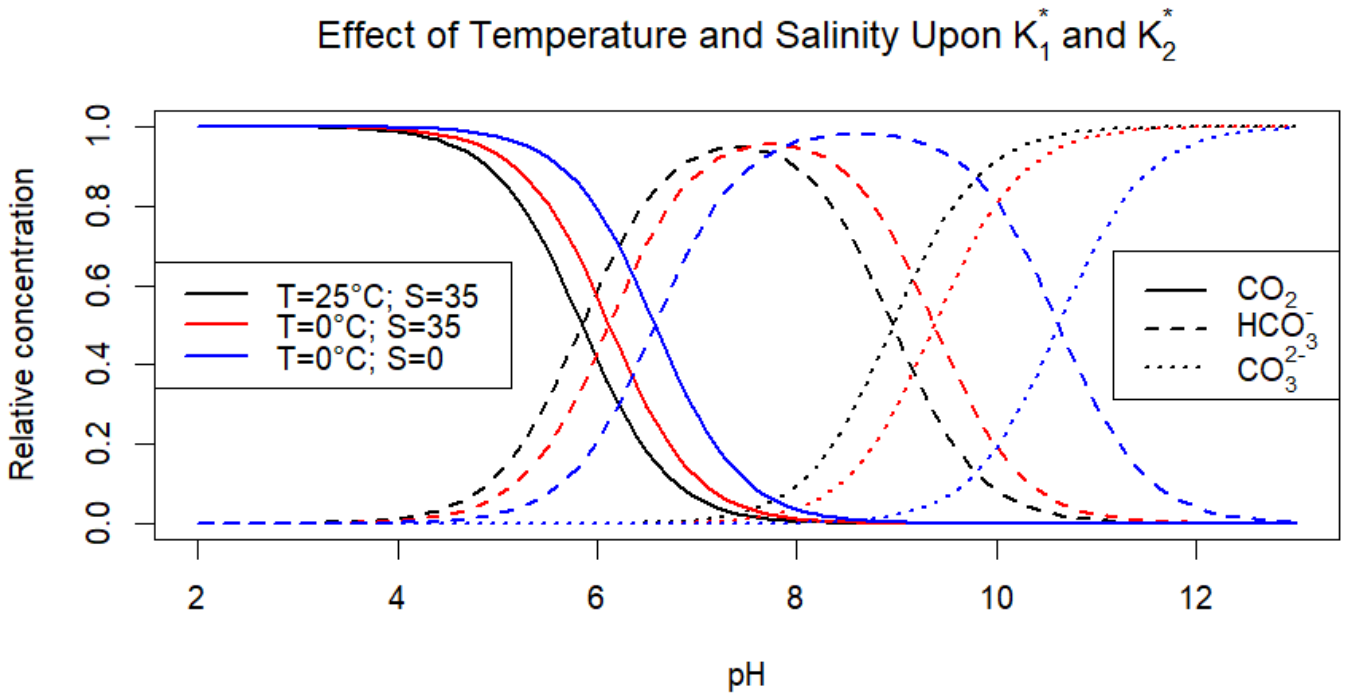

Figure 2.1: Bjerrum plot indicating the effect of temperature and salinity on the relative concentrations of carbonate species (Gattuso et al., 2021). Y axis is exaggerated to enable better visualization of differences between lines.

For example, when ocean water with a pH of ~8.1 undergoes cooling from 25°C to 0°C (from the black line to the red line), the equilibria between HCO_3^- and CO_3^{2-} (defined by K_2^*) favours HCO_3^-. Thus, the concentration of CO_3^{2-} ions decreases while the relative concentration of HCO_3^- increases. Likewise, when salinity is lowered from S = 35 to S = 0 by dilution with pure freshwater (from the black line to the blue line), HCO_3^- is favoured, causing the relative concentration of CO_3^{2-} ions to decrease. These changes are a result of the change in activity of hydrogen ions $\{H^+\}$ as physical conditions of T, S, & P change. Ultimately, the decrease in CO_3^{2-} ion concentration reduces the buffering capacity of seawater. As more CO_2 dissolves into solution, forming carbonic acid, CO_3^{2-} ions are no longer available to consume the additional H^+ ions, so solution pH is lowered (seawater becomes more acidic). Because of this, cool and fresh Arctic Ocean waters are expected to be more sensitive to ocean acidification and carbonate mineral undersaturation than relatively warmer, saltier waters with the same inorganic carbon concentration.

2.2. Key Processes affecting the Marine Inorganic Carbon System

2.2.1. Solubility Pump

Within the ocean, seawater pCO_2 is altered mainly though physical and biological processes called “pumps”, which move inorganic carbon against its oceanic concentration gradient from surface to depth. Although the ocean contains ~40 times more carbon than the atmosphere within its dissolved inorganic carbon (DIC) pool (Friedlingstein et al., 2023), air–sea CO_2 exchange is governed by the pCO_2 gradient between the atmosphere and the ocean surface rather than the total carbon inventory, permitting the ocean to take up CO_2 in spite of an already large DIC pool. Once in the ocean, CO_2 taken up through air-sea exchange can then be transferred, against the concentration gradient, to the deep ocean through these "pump” processes. For example, the “solubility pump” transfers newly absorbed CO_2 from the surface to the ocean interior through density-driven circulation and vertical exchange. At high latitudes, surface waters become denser through cooling and brine rejection during sea-ice formation, which promotes convection, resulting in deep water formation (Anderson & Macdonald, 2015). These processes export carbon-rich surface waters away from the atmosphere on seasonal to centennial timescales.

The solubility pump is particularly effective in the Arctic because low temperatures enhance CO_2 solubility, seasonal sea-ice formation increases surface water density through brine rejection, and wintertime cooling and wind forcing deepen the mixed layer, ventilating subsurface waters (Anderson & Macdonald, 2015). Once exported below the surface layer, strong stratification from freshwater inputs can isolate carbon-rich waters from the atmosphere, helping maintain relatively low surface pCO_2 that supports continued atmospheric CO_2 uptake (Anderson & Macdonald, 2015).

2.2.2. Biological Pump

The “biological pump" also works against the surface ocean – deep ocean gradient to enrich deep water with inorganic carbon, relative to the surface (Raven & Falkowski, 1999). The biological pump describes the net result of biologically-driven processes on ocean DIC. Photosynthesis is the main mechanism through which autotrophic organisms (algae, phytoplankton, etc.) utilize dissolved nutrients (nitrate and phosphate) and CO_2 to form organic matter:

Eq. 2.10
$$106CO_2 + 16NHO_3 + H_3PO_4 + 122H_2O \rightleftarrows C_{106}H_{263}O_{110}N_{16}P + 138O_{2\,(g)}$$

The coefficients within this equation are representative of the “Redfield ratio” which is the average ratio of P:N:C:-O_2 (1:16:106:-138) utilized by algae metabolisms (Redfield, 1958). While originally determined for the northern Atlantic Ocean, the Redfield ratio has been demonstrated to be consistent across the global ocean (Sterner et al., 2008). When the forward reaction proceeds (i.e., photosynthesis), inorganic components (CO_2 and H_2O) are consumed to create organic matter. This process, termed primary production and is limited by the presence of light and availability of nutrients. As such, primary production is generally restricted to the upper water column (the euphotic zone) where sunlight is present. In the Arctic, nutrient delivery is primarily controlled through upwelling of nutrient rich waters (Tremblay et al., 2015), lateral transport (Torres-Valdés et al., 2013), and in some environments, river runoff (Le Fouest et al., 2013). Photosynthesis occurring as a result of these external nutrient inputs is called “new production.”

When the reverse reaction proceeds, heterotrophic organisms (e.g., fish or bacteria) consume oxygen to break down organic matter and produce CO_2 and nutrients. This process, “respiration” or “remineralization,” occurs via both single celled and multicellular organisms in both the surface and deep ocean, as sunlight is not required for the reaction to proceed. Thus, remineralization results in nutrient accumulation in deep waters; however, nutrients remineralized in the upper water column may be recycled by primary producers, resulting in “regenerated production.” The difference between total primary production (regenerated + new) and respiration is referred to as net community production (NCP) and may be used to estimate the export of carbon out of the surface ocean.

Ultimately, this delivery of carbon from the surface and deep ocean via sinking organic material that is remineralized to CO_2 at depth, is the main effect of the biological pump. Under a strong biological pump, vertical transport and remineralization of organic matter will result in an increase in DIC and decrease in pH of deep waters, while primary production in the surface ocean decreases DIC and increases pH.

Within the Arctic Ocean, seasonal processes also impact primary production and thus the efficiency of the biological pump. The high latitude of the region results in periods of 24hr sunlight in the summer and 24hr of darkness in the winter, supporting increased primary production in the summer if nutrients are also available. In the winter, brine rejection from sea ice formation mixes the upper ocean water column potentially bringing deeper ocean nutrients into the surface layer. As snow covered sea ice limits light transmission, respiration may cause further concentration of nutrients in the surface ocean until sea ice concentration begins to decrease, particularly in coastal and shelf regions receiving substantial terrestrial organic matter inputs. These processes are particularly important in SHB-JB where shallow bathymetry, strong freshwater input, and seasonal sea ice modulate both primary productivity and carbon export. River discharge supplies nutrients and organic matter to the ocean, stimulating primary production during the open-water season while enhancing stratification (Azetsu-Scott et al., 2014; Capelle et al., 2020). Seasonal sea-ice formation promotes brine rejection and convective mixing, which can ventilate subsurface waters and redistribute remineralized nutrients to the surface, priming production during spring melt (Tremblay et al., 2015).

2.2.3. Freshwater Input

The Arctic Ocean receives a disproportionately large amount of freshwater for its size. Despite accounting for only 4% of the global ocean (by surface area), the Arctic Ocean receives 11% of global river runoff (Jakobsson, 2002). Freshwater inflow lowers the ocean's overall buffering capacity (decrease in TA) resulting in increased sensitivity to OA (Carmack et al., 2016). Additionally, large quantities of freshwater may stratify the water column, limiting mixing between the surface and deep layers. Changes due to human activity and climate warming in recent years have led to alterations in freshwater runoff to the Arctic Ocean, with pan-Arctic river discharge showing a sustained long-term increase, in some years exceeding historical (1980–1989) averages by ~10–20% (Holmes et al., 2015).

2.2.4. Gas Exchange

The oceans play a major role in regulating atmospheric CO_2. However, the direction (i.e., absorption or release) and strength of CO_2 movement is determined regionally through physical and biological factors (Sarmiento & Gruber, 2006). For example, polar ocean surface waters are depleted in CO_2 with respect to the atmosphere due to their decreased water temperature and salinity relative to mid-latitude regions (Sarmiento & Gruber, 2006). To remedy this gradient with the atmosphere, the polar oceans are able to absorb increasing amounts of CO_2 (Takahashi et al., 1993), a proportion of which will be from anthropogenic emissions. However, the length of time needed to equilibrate CO_2 with the atmosphere is approximately 6 months resulting in seawater rarely being in equilibrium with the atmosphere (Sarmiento & Gruber, 2006). Thus, CO_2 exchange from the atmosphere to the ocean is the primary driver of OA in Arctic Ocean surface waters (AMAP, 2018).

2.3. *References*

AMAP. (2013). *Arctic Monitoring and Assessment Programme (AMAP) Assessment 2013: Arctic Ocean Acidification*. www.amap.no

AMAP. (2018). *AMAP Assessment 2018: Arctic Ocean Acidification*.

Anderson, L. G., & Macdonald, R. W. (2015). Observing the Arctic Ocean carbon cycle in a changing environment. *Polar Research*, *34*(1), 26891. https://doi.org/10.3402/polar.v34.26891

Azetsu-Scott, K., Starr, M., Mei, Z. P., & Granskog, M. (2014). Low calcium carbonate saturation state in an Arctic inland sea having large and varying fluvial inputs: The Hudson Bay system. *Journal of Geophysical Research: Oceans*, *119*(9), 6210–6220. https://doi.org/10.1002/2014JC009948

Azevedo, L. B., De Schryver, A. M., Hendriks, A. J., & Huijbregts, M. A. J. (2015). Calcifying species sensitivity distributions for ocean acidification. *Environmental Science and Technology*, *49*(3), 1495–1500. https://doi.org/10.1021/es505485m

Capelle, D. W., Kuzyk, Z. Z. A., Papakyriakou, T., Guéguen, C., Miller, L. A., & Macdonald, R. W. (2020). Effect of Terrestrial Organic Matter on Ocean Acidification and CO2 Flux in an Arctic Shelf Sea. *Progress in Oceanography*, *185*. https://doi.org/10.1016/j.pocean.2020.102319

Carmack, E. C., Yamamoto-Kawai, M., Haine, T. W. N., Bacon, S., Bluhm, B. A., Lique, C., Melling, H., Polyakov, I. V., Straneo, F., Timmermans, M. L., & Williams, W. J. (2016). Freshwater and its role in the Arctic Marine System: Sources, disposition, storage, export, and physical and biogeochemical consequences in the Arctic and global oceans. *Journal of Geophysical Research: Biogeosciences*, *121*(3), 675–717. https://doi.org/10.1002/2015JG003140

Dickson, A., Sabine, C., & Christian, J. (2007). *Guide to best practices for ocean CO_2 measurements*. North Pacific Marine Science Organization.

Friedlingstein, P., O'Sullivan, M., Jones, M. W., Andrew, R. M., Bakker, D. C. E., Hauck, J., Landschützer, P., Le Quéré, C., Luijkx, I. T., Peters, G. P., Peters, W., Pongratz, J., Schwingshackl, C., Sitch, S., Canadell, J. G., Ciais, P., Jackson, R. B., Alin, S. R., Anthoni, P., … Zheng, B. (2023). Global Carbon Budget 2023. *Earth System Science Data*, *15*(12), 5301–5369. https://doi.org/10.5194/essd-15-5301-2023\

Holmes, R. M., Shiklomanov, A., Tank, S. E., McClelland, J. W., & Tretiakov, M. (2015). River Discharge, Arctic Report Card: Update for 2015.

Jakobsson, M. (2002). Hypsometry and volume of the Arctic Ocean and its constituent seas. *Geochemistry, Geophysics, Geosystems*, *3*(5), 1–18. https://doi.org/10.1029/2001gc000302

Jiang, L.-Q., Carter, B. R., Feely, R. A., Lauvset, S. K., & Olsen, A. (2019). Surface ocean pH and buffer capacity: Past, present and future. *Scientific Reports*, *9*(1), 18624. https://doi.org/10.1038/s41598-019-55039-4

Jutterström, S., & Anderson, L. G. (2005). The saturation of calcite and aragonite in the Arctic Ocean. *Marine Chemistry*, *94*(1–4), 101–110. https://doi.org/10.1016/j.marchem.2004.08.010

Le Fouest, V., Babin, M., & Tremblay, J.-É. (2013). The fate of riverine nutrients on Arctic shelves. *Biogeosciences*, *10*(6), 3661–3677. https://doi.org/10.5194/bg-10-3661-2013

Mucci, A., Canuel, R., & Zhong, S. (1989). The solubility of calcite and aragonite in sulfate-free seawater and the seeded growth kinetics and composition of the precipitates at 25°C. *Chemical Geology*, *74*(3–4), 309–320. https://doi.org/10.1016/0009-2541(89)90040-5

Raven, J. A., & Falkowski, P. G. (1999). Oceanic sinks for atmospheric CO_2. *Plant, Cell & Environment*, *22*(6), 741–755. https://doi.org/10.1046/j.1365-3040.1999.00419.x

Redfield, A. C. (1958). The Biological Control of Chemical Factors in the Environment. *American Scientist*, *46*(3), 205–221.

Sarmiento, J. L., & Gruber, N. (2006). *Ocean biogeochemical dynamics*. Princeton University Press.

Sterner, R. W., Andersen, T., Elser, J. J., Hessen, D. O., Hood, J. M., McCauley, E., & Urabe, J. (2008). Scale-dependent carbon:nitrogen:phosphorus seston stoichiometry in marine and freshwaters. *Limnology and Oceanography*, *53*(3), 1169–1180. https://doi.org/10.4319/lo.2008.53.3.1169

Takahashi, T., Olafsson, J., Goddard, J. G., Chipman, D. W., & Sutherland, S. C. (1993). Seasonal Variation of CO_2 and Nutrients in the High-Latitude Surface Oceans: A Comparative Study. *Global Biogeochemical Cycles*, *7*(4), 843–878.

Torres-Valdés, S., Tsubouchi, T., Bacon, S., Naveira-Garabato, A. C., Sanders, R., McLaughlin, F. A., Petrie, B., Kattner, G., Azetsu-Scott, K., & Whitledge, T. E. (2013). Export of nutrients from the Arctic Ocean. *Journal of Geophysical Research: Oceans*, *118*(4), 1625–1644. https://doi.org/10.1002/jgrc.20063

Tremblay, J.-É., Anderson, L. G., Matrai, P., Coupel, P., Bélanger, S., Michel, C., & Reigstad, M. (2015). Global and regional drivers of nutrient supply, primary production and CO2 drawdown in the changing Arctic Ocean. *Progress in Oceanography*, *139*, 171–196. https://doi.org/10.1016/j.pocean.2015.08.009

Zeebe, R. E., & Wolf-Gladrow, D. (2001). *CO_2 in seawater: Equilibrium, Kinetics, Isotopes* (D. Halpern, Ed.). Elsevier.

Chapter 3: CO_2 evasion from a shallow sub-arctic sea during August (2021-2023)

N. Decker[1], T. Papakyriakou[1], D. Capelle[2], Z. Kuzyk[1], C.J. Mundy[1], K. Yezhova[1], K. Brown[1]*
**Corresponding Author (deckern@myumanitoba.ca)*
[1]Centre for Earth Observation Science (CEOS), Department of Environment and Geography, University of Manitoba, Winnipeg, Manitoba, Canada
[2]Freshwater Institute, Fisheries and Oceans Canada, Winnipeg, Manitoba, Canada
This chapter is prepared for publication is the journal: *Elementa: Science of the Anthropocene*
Please see appendix A for the contributions of each collaborating author.

Abstract

Anthropogenic carbon dioxide (CO_2) emissions have led to a global increase in atmospheric CO_2 concentrations since the pre-industrial era, with the concentration of CO_2 in the surface ocean increasing in response. Physical, biological, and biogeochemical processes contribute to regionally variable surface ocean CO_2 exchanges with the atmosphere, causing some regions to take up CO_2 more effectively than others. This heterogeneity is difficult to integrate into global ocean models, however, as field observations of CO_2 fluxes over regions such as the Arctic Ocean and sub-Arctic seas are lacking. One important regional gap is the Hudson Bay marine region in central Canada, where cold temperatures and relatively fresh waters may enhance CO_2 uptake relative to other regions. However, its exceptionally shallow, estuarine character may limit its capacity for carbon sequestration. Here we present the first observations of surface water CO_2 partial pressure (pCO_2), salinity, and temperature in Southern Hudson Bay and James Bay (SHB – JB), which borders Canada's most carbon-rich watersheds in the Hudson Bay Lowlands (HBL). Although surface water pCO_2 varied within and between the three summers (August) of observation (2021, 2022, and 2023), mean pCO_2 (457, 453, and 477 µatm) was always above atmospheric CO_2 concentration (~416 µatm). Mean calculated CO_2 fluxes from the ocean to the atmosphere for August 2021, 2022, and 2023 were +2.8 ±3.8, +1.5 ±3.3, and +3.7 ±3.7 mmol CO_2 m^{-2} d^{-1}, respectively. These results indicate that SHB – JB were weak sources of CO_2 to the atmosphere during August, in contrast to what has been observed in the spring and fall in central Hudson Bay. Increased water temperature due to river input explained much of the variability in pCO_2 across the region; however, additional processes, such as primary production, mixing, and freshwater addition also contributed significantly to the regional variability in surface ocean pCO_2 during this time of year. This work highlights the need for regional scale pCO_2 measurements in Arctic and sub-Arctic seas due to the regional and seasonal variation in freshwater cycling and terrestrial carbon input. These types of observations will be necessary to adequately represent regional variability in global ocean models to improve regional and global CO_2 flux estimates.

3.1 Introduction

The concentration of carbon dioxide (CO_2) in the atmosphere has increased by almost 40% over pre-industrial levels, largely due to the burning of fossil fuels (9.9 Gt C yr^{-1}; Doney et al., 2009; Friedlingstein et al., 2023; Paustian et al., 2000). In turn, the oceanic uptake of CO_2 has also increased as the surface ocean seeks to reach equilibrium with the atmosphere (Friedlingstein et al., 2023). The oceans have played a major role in modulating atmospheric CO_2 since industrialization, accounting for the uptake of 185 ±35 Gt C, roughly equivalent to 26% of total anthropogenic emissions since 1850 (Friedlingstein et al., 2025; Sarmiento & Gruber, 2006). Despite accounting for 4.3% of the global surface ocean, the Arctic Ocean is estimated to contribute between 5 - 14% of the global CO_2 sink, accounting for an uptake of 166 ±60 Tg C per year (Bates & Mathis, 2009; Jakobsson, 2002; MacGilchrist et al., 2014). However, large uncertainties remain in the Arctic carbon budget (MacGilchrist et al., 2014) and ongoing ocean warming makes the region's future CO_2 uptake potential uncertain (Yasunaka et al., 2023). In particular, the Arctic coastal seas, which make up ≈53% of the Arctic Ocean, remain understudied (Bates & Mathis, 2009; Jakobsson, 2002; Yasunaka et al., 2023) and are especially vulnerable to change as amplified warming in polar regions continues to impact both the delivery of carbon to, and cycling of carbon within, the coastal marine system (Bauer et al., 2013; Nielsen et al., 2024). Changes brought on by anthropogenic climate warming in the Arctic such as increased runoff (Déry et al., 2016) and delivery of terrestrial carbon (Vonk et al., 2025), warming (McLaughlin & Packalen, 2021), and a longer ice-free season (Markus et al., 2009) have already weakened the coastal Arctic ocean's carbon uptake capacity (Vonk et al., 2025). Enhanced monitoring of Arctic coastal biogeochemical systems is needed to better understand how their CO_2 uptake capacity will respond to continued climate warming (Friedlingstein et al., 2025; Vonk et al., 2025).

Southern Hudson Bay and James Bay (Figure 3.1) are shallow sub-Arctic seas that drain the world's second largest contiguous peatland and store of soil organic carbon (McLaughlin & Packalen, 2021), much of which is locked in permafrost (Schuur et al., 2015). Yet they are notably underrepresented in global ocean and pan arctic CO_2 flux estimates (Takahashi et al., 2009; Yasunaka et al., 2023). Recent studies suggest Hudson Bay and Hudson Strait are moderate to weak CO_2 sinks during the open water season relative to other Arctic shelf regions (Ahmed et al., 2021). However, the inorganic carbon system of James Bay remains unstudied, and the potential for terrestrial carbon inputs from the HBL to SHB-JB are sufficiently large as to represent a large source of error when constructing carbon budgets for the Hudson Bay marine region (Capelle et al., 2020). Here, our goal is to document, for the first time, the role of the SHB-JB region as a sink or source of CO_2 during the mid-summer and to establish the main drivers of surface water pCO_2 variability within the region at that time of year.

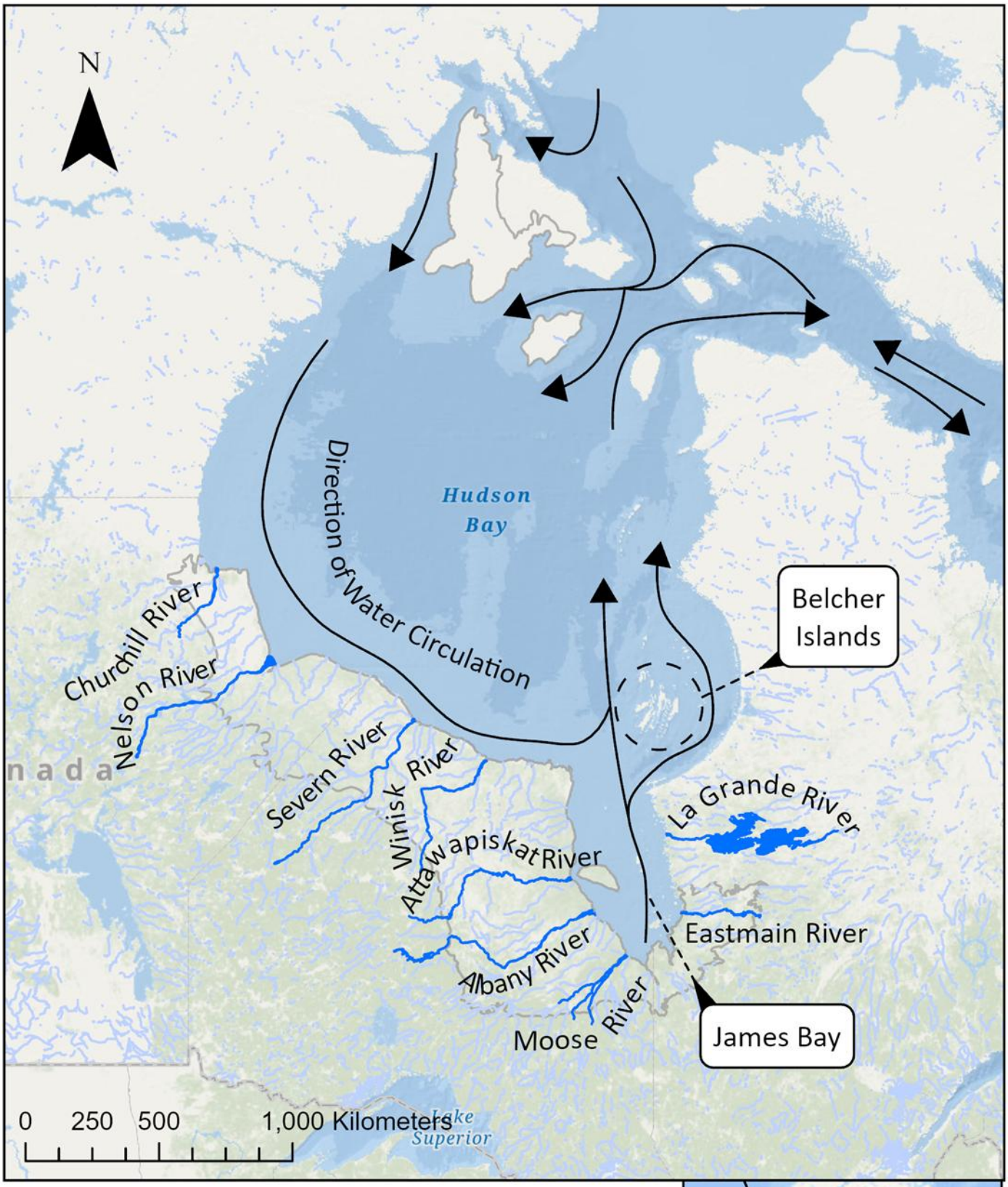

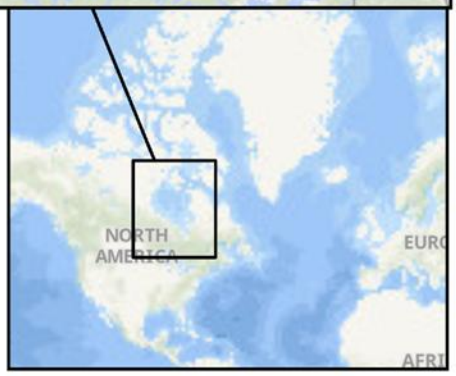

Figure 3.1: Hudson Bay, James Bay, and the Belcher Islands. Circulation pattern adapted from Ridenour et al., 2019. River boundaries adapted from Statistics Cananda 2016 census. Spatial Reference: Name: WGS 1984 Web Mercator Auxiliary Sphere, Map Units: Meter. Sources: Esri, TomTom, Garmin, GEBCO, National Geographic, NOAA, FAO, USGS, EPA, NRCan, Parks Canada, NaturalVue, and the GIS User Community

3.2 Study Area: Hudson Bay and James Bay

Seawater enters Hudson Bay from the Arctic Ocean via Foxe Basin, and from the North Atlantic Ocean via Hudson Strait, following a cyclonic (counter-clockwise) circulation pattern within the bay during the summer months (Figure 3.1; Ridenour et al., 2019). A portion of this water enters James Bay, a peripheral sea at the southern tip of Hudson Bay, from the northwest before transiting cyclonically, ultimately exiting from the northeast, and circulating northwards past the Belcher Islands. Water then passes north along the eastern flank of Hudson Bay, before entering Hudson Strait and finally flowing into the Labrador Sea (Ridenour et al., 2019). The region receives a disproportionately large amount of freshwater compared to other Arctic regions through several large rivers that drain into Hudson Bay (Churchill, Nelson, Winisk; ~266 km^3 yr^{-1}) and James Bay (Albany, Moose, Eastmain, La Grande; ~260 km^3 yr^{-1}), accounting for 46% of total Canadian river runoff to the Arctic (Déry et al., 2016). Consequently, the surface salinity of Hudson Bay and James Bay (average ~25) is much lower than the global average for ocean surface waters (~35; Sarmiento & Gruber, 2006). This region is seasonally covered with sea ice from late October-December to early June, with peaks in ice thickness in May; however, ice thickness begins declining in James Bay a month earlier than Hudson Bay (Gagnon & Gough, 2006; Landy et al., 2017). Sea ice reaches a maximum thickness of 1 m in James Bay and 1.5 m in Hudson Bay, increasing with latitude in James Bay and longitude (east – west) in Hudson Bay (Gagnon & Gough, 2006; Martini, 1986). A freshwater flux of ~ 1200 km^3 or more is withdrawn from, or added to, the water column due to sea ice formation and melt in Hudson Bay, seasonally altering surface ocean salinity (Granskog et al., 2011; Prinsenberg, 1988). The combination of river input and sea ice melt works to stratify the surface of the bays, creating a CO_2 depleted surface layer through the dilution of seawater (Ahmed et al., 2020).

Local river water drainage to southwestern Hudson Bay and James Bay is through the Hudson Bay Lowlands (HBL). The HBL is the world's second largest contiguous northern peatland with an estimated total carbon storage of ~30 Pg C, equivalent to 20% of North American soil carbon stocks (Packalen et al., 2014). Above 51°N, this large peatland spans the gradient of continuous to sparse permafrost that is susceptible to thaw due to climate warming; together with increased occurrence of wildfires, permafrost thaw is thought to be weakening the region's role as a CO_2 sink (Tarnocai, 2006; Virkkala et al., 2025). Arctic rivers carry considerable amounts of carbon (inorganic and organic) seaward to the bays (Vonk et al., 2025); however, the downstream impact of thawing permafrost on the river carbon load has not been quantified. While changes in the delivery of terrestrial carbon will impact seawater pCO_2 in the bays (e.g., Capelle et al., 2020), there remains limited inorganic carbon measurements in southern Hudson Bay (Ahmed et al., 2020, 2021; Else et al., 2008) and no published baseline observations in James Bay against which to assess such impacts.

3.3 Methods

3.3.1 Surface Water Measurements

Data collection occurred during August 2021, 2022, and 2023 on board the r/v William Kennedy. Detailed sample collection procedures are described in Ausen et al. 2023, Kamula et al. 2022, and Mundy et al. 2024. Surface water was pumped through the ship's hull (~2m depth) continuously throughout the study at a rate of 1 L min^{-1} and passed through a ProOceanus® CO_2-Pro FT sensor (0.01 ppm CO_2 resolution, 0 – 1000 ppm CO_2, ±0.5%), which uses a gas-permeable membrane and infrared gas detector. The sensor is automatically compensated for drift from zero, by performing a zero calibration every 6 hours (~1 – 3 ppm drift over 6 hr). This instrument provided CO_2 molar ratio measurement from the water every five to seven minutes while the ship was in operation. The CO_2 partial pressure (pCO_2) was calculated as the product of the CO_2 molar ratio (in ppm) in the total pressure of the gas stream supplied by the sensor. The sensor headspace air is not dried and therefore the pCO_2 did not need water vapour correction. The resulting pCO_2 was merged with the ship's GPS and navigation data, as well as a thermosalinograph (TSG) (Sea-Bird Electronics, SBE 21 SeaCAT Thermosalinograph) that provided temperature (±0.01 °C) and conductivity measurements (±0.001 S m^{-1}) used to estimate salinity (GSW Toolbox, *Section 3.2.4*). Here we report salinity values on the Practical Salinity Scale (PSS-78), without units. Underway system data were screened to remove periods of instrument maintenance, periods when the ship was at a port, and periods when the water flow rate dropped below 1 L min^{-1}. The total uncertainty associated with the surface water pCO_2 measurements is summarized in supplementary information (Supplementary Table B.1). Intersystem comparisons of the ProOceanus® CO_2-Pro FT sensor indicate good agreement between the CO_2-Pro FT sensor and other, more commonly used underway systems (i.e. General Oceanics; Arruda et al., 2019).

When compared with CTD temperature measurements, the TSG temperature measurements were consistently 0.5 to 1°C warmer, likely due to the travel time between the hull mounted intake and the instrument's sensor. To account for the increased temperature observed by the TSG, the CTD temperature was used to correct the TSG temperature data. Linear regression models were used to estimate the relationship between TSG and CTD temperature measurements. The resulting relationships were used to correct the TSG temperature measurements to in situ conditions for each year.

3.3.2 CTD Casts & Water Sampling

Hydrographic profiles were collected using a Sea-Bird SBE 19plus V2 SeaCAT profiler CTD (Conductivity, Temperature, Depth) deployed by winch off the ship's stern at station stops. The CTD was equipped with a Biospherical Instruments Inc. scalar photosynthetically active radiation (PAR) sensor, a Sea-Bird/WET Labs chlorophyll a (CHL-a) fluorometer, a Sea-Bird SBE 43 dissolved oxygen (DO) sensor, and a Chromophoric Dissolved Organic Matter (CDOM)

fluorometer. CTD measurements from within the surface mixed layer (average SML = 9.1 ± 6m, 7.5 ± 5m, and 7.1 ± 4m in 2021, 2022, 2023, respectively) were synchronized with the underway systems to correlate surface water CDOM, DO, and CHL-a estimations with surface water pCO_2 observations.

Water samples were collected in profiles for the determination of salinity and stable water isotopes ($\delta^{18}O$-H_2O, herein $\delta^{18}O$) using a SBE32 Rosette with 5L Niskin bottles, and a tap within the laboratory of the ship, fed through the same intake as the pCO_2 and TSG sensors. Samples collected for $\delta^{18}O$ determination were analysed with respect to the V-SMOW ratio of ^{18}O to ^{16}O at the University of Ottawa's Ján Veizer Stable Isotope Laboratory using a Finnigan MAT Delta plus XP + Gasbench (±2.0 ‰) following analytical methods outlined in de Groot (2004). Salinity samples were analysed at the University of Manitoba (2021 and 2023) on a Guildline 8410A Portasal (±0.003) and at Amundsen Science (2022) on a Guildline 8400B Autosal (±0.002).

3.3.3 Atmospheric Measurements

CO_2 flux studies require wind-speed and atmospheric CO_2 measurements. Wind speed was obtained from the National Centres for Environmental Prediction's (NCEP) North American Regional Reanalysis (NARR) database (8 times daily, 32 km resolution; Mesinger et al., 2006). As no atmospheric CO_2 observations are available for SHB-JB, we used the global atmospheric CO_2 concentration obtained from the National Oceanic and Atmospheric Administration's (NOAA) historic atmospheric CO_2 archive for the month of sampling (Lan et al., 2025).

3.3.4 Sea Ice Cover Period

To assist in examining the influence sea ice melt on surface water pCO_2, the extent of Hudson Bay sea ice cover was determined for the study period. The sea ice cover period was determined using the University of Bremen's Advanced Microwave Scanning Radiometer 2 (AMSR-2) sea ice database. Sea ice concentration was reported using a 6.25 km grid (Spreen et al., 2008). A mean weekly sea ice concentration of 15% was selected as the threshold for sea ice presence (> 15%) or absence (<15%).

3.3.5 Data Analysis & Calculations

3.3.5.1 Sea Ice melt and Meteoric water fractions

Surface water salinity and isotopic composition were used to track the distribution of meteoric water (river input, direct precipitation). Water mass fractions were estimated using three linear equations in tandem with three endmembers: seawater (SW), meteoric water (MW), and sea ice melt (SIM) (Table B.1), following Ostlund & Hut (1984):

Eq. 3.1 $$f_{SW} + f_{MW} + f_{SIM} = 1$$

Eq. 3.2 $$f_{SW}S_{SW} + f_{MW}S_{WM} + f_{SIM}S_{SIM} = S_{observed}$$

Eq. 3.3 $$f_{SW}\delta^{18}O_{sw} + f_{MW}\delta^{18}O_{MW} + f_{SIM}\delta^{18}O_{SIM} = \delta^{18}O_{observed}$$

here f denotes the fraction of the associated component, S is the salinity, and $\delta^{18}O$ is the stable isotope composition of water. Endmembers for SIM and SW used in calculations are modified from (Ahmed et al., 2020). The MW endmember used in our study reflects observations from the Moose River estuary at 0 salinity, as this is the largest river close to the cruise track (Table 3.1).

Table 3.1: Endmembers used for water mass fraction determination. Seawater (SW) and Sea Ice Melt (SIM) endmembers were determined based on field observations of Hudson Bay seawater and sea ice by Ahmed et al. (2020). Meteoric Water (MW) endmember was determined through linear regression of observations in the Moose River estuary. Distribution of SW, MW, and SIM may be found in Appendix B.

	Salinity	*$\delta^{18}O$ (‰)*
Seawater (SW)	32.1 ±0.1	-2.5 ±0.2
Meteoric Water (MW)	0	12.3 ±0.3
Sea Ice Melt (SIM)	1.4 ±0.5	-0.8 ±0.2

3.3.5.2 pCO_2 Temperature Normalization

To account for effects of temperature changes on surface ocean pCO_2 dynamics, pCO_2 values were normalized to temperature following Takahashi et al. (2002):

Eq. 3.4 $$pCO_{2_{Temp}} = pCO_{2_{mean}} * e^{0.0423(T_{observed} - T_{mean})}$$

Eq. 3.5 $$pCO_{2_{Net}} = pCO_{2_{observed}} * e^{0.0423(T_{mean} - T_{observed})}$$

Where the mean pCO_2 (pCO_{2Mean}) or observed pCO_2 ($pCO_{2Observed}$) values are transformed by the empirically determined relationship between temperature and pCO_2 in seawater ($e^{0.0424}$), scaled by the difference in observed ($T_{observed}$) and mean temperatures (T_{mean}, yearly, Table 3.2). This normalization produces two values, pCO_{2Temp}, representative of processes related to temperature's influence on surface water pCO_2; and pCO_{2Net}, representative of the

remaining (net) effects upon surface water pCO_2 after temperature variability has been accounted for. The "net" effects incorporate all changes in surface water pCO_2 due to primary production, respiration, alkalinity change, dilution through freshwater addition, mixing, and air – sea exchange of CO_2 (Henson et al., 2018; Takahashi et al., 2002). The ratio of pCO_{2Temp} to pCO_{2Net} indicates the relative strength of the temperature effect upon surface water pCO_2 variability. In other words, when $pCO_{2Temp} > pCO_{2Net}$, temperature variation dominates the observed pCO_2 variability in the dataset; whereas when $pCO_{2Temp} < pCO_{2Net}$, other physical and biological factors (net) exert stronger controls over the observed variation in surface pCO_2 (Henson et al., 2018; Takahashi et al., 2002).

Table 3.2: Summary statistics for surface water properties as observed from the underway thermosalinograph and flow-through pCO_2 systems. Sub–regions are defined in Figure 3.3.

Region	Year	Salinity				Temperature (°C)				pCO_2 (µatm)			
		Min	*Mean*	*s.d.*	*Max*	*Min*	*Mean*	*s.d.*	*Max*	*Min*	*Mean*	*s.d.*	*Max*
James Bay	*2021*	9.7	22.3	3.5	26.2	5.9	10.0	2.4	18.5	300.7	469.6	54	601.5
	2022	12.1	20.7	3.2	25.7	5.9	10.6	2.6	15.9	215.8	484.7	57	592.2
	2023	16.4	22.4	2.3	26.3	5.9	10.6	2.6	16.2	443.4	502.9	40	587.2
	All	9.7	21.5	3.3	26.3	5.9	10.4	2.5	18.5	215.8	483.6	55	601.5
Belcher Islands	*2021*	n.d.											
	2022	22.4	27.0	1.6	29.0	1.9	6.3	2.6	12.0	349.7	422.2	22	469.3
	2023	44.5	26.6	1.2	29.4	5.0	8.8	1.8	14.1	416.7	473.1	27	532.1
	All	22.4	26.8	1.4	29.4	1.9	7.8	2.5	14.1	349.7	452.3	36	532.1
Southern Hudson Bay	*2021*	21.8	27.0	2.2	31.4	4.4	7.5	1.4	11.1	374.2	438.2	28	496.2
	2022	19.4	27.1	2.2	30.4	4.8	7.8	1.3	12.2	350.6	421.6	29	479.5
	2023	19.6	27.1	1.3	29..7	4.4	10.4	1.4	14.2	416.7	469.1	23	534.8
	All	19.4	27.1	1.9	31.4	4.4	8.6	1.9	14.2	350.6	445.0	34	534.8
All Regions	*2021*	9.7	24.2	3.8	31.4	4.4	9.0	2.4	18.9	300.7	456.7	48	601.5
	2022	12.1	23.9	4.1	30.4	1.9	8.8	3.1	15.9	215.8	453.4	54	592.2
	2023	16.4	26.0	2.3	29.7	4.4	9.6	2.1	16.2	416.7	477.3	31	587.2
	All	9.7	24.7	3.7	31.4	1.9	9.1	2.6	18.5	215.8	462.8	47	601.5

3.3.5.3 *CO_2 Flux Calculation*

The exchange of CO_2 gas between the surface ocean and atmosphere was calculated using the thin boundary model (bulk flux equation, Eq. 3.6) and gas exchange relationship (Eq. 3.7) outlined by Wanninkhof (2014):

Eq. 3.6 $$F_{atm-ocean} = kK_0(\mathrm{pCO_{2sw}} - \mathrm{pCO_{2atm}})$$

Eq. 3.7 $$k = 0.251U_{10m}^2(Sc/660)^{-0.5}$$

Where F is the exchange (flux) of CO_2 between the atmosphere and surface of the ocean measured in CO_2 per square metre per unit time (e.g., mmol m^{-2} d^{-1}), k is the transfer velocity (m d^{-1}), K_0 is the aqueous phase solubility of CO_2 in water (mol m^{-3} atm^{-1}), and pCO_{2sw} – pCO_{2atm} is the difference between seawater and atmospheric pCO_2 (µatm; Wanninkhof, 2014). In Equation 3.7, transfer velocity (k; cm hr^{-1}) is calculated using wind speed 10m above sea surface (U_{10m}) and the Schmidt number (Sc), a gas and temperature specific parameter representative of the kinematic viscosity of water divided by the molecular diffusion coefficient of the respective gas (Wanninkhof, 2014). Schmidt number and CO_2 solubility constants were obtained from Wanninkhof (2014) and Weiss (1974), respectively. Fluxes represent an exchange of a certain magnitude, over a time interval, in a specific direction; therefore, using these equations it is possible to estimate the total exchange of carbon, quantified as either an absorption flux (negative, into the ocean) or an emission flux (positive, towards the atmosphere).

3.3.6 Analysis Programs

All data analyses were done using R (v 4.43) and Ocean Data View (ODV, v 5.8.1). Mixed layer depth was determined from CTD casts using ODV with the depth at the maximum estimated Brunt-Väisälä (BV) frequency to indicate the bottom of the surface mixed layer (Roch et al., 2023). A minimum depth (3m) threshold was set to avoid underestimations, while a maximum BV (14 cycles hr^{-1}) threshold was set to avoid overestimations due to conductivity increases at depth. The difference between oxygen saturation concentration and observed dissolved oxygen, apparent oxygen utilization (AOU), was calculated in ODV from CTD-derived temperature, salinity, and dissolved oxygen measurements. To understand potential controls on surface water pCO_2, we applied linear regression models examining the relationship between observed pCO_2 and other ecosystem variables such as temperature, salinity, CDOM, CHL-a, and f_{MW}. A strong correlation between pCO_2 and an ecosystem variable does not imply causation; however, the likelihood of causation may be evaluated using known biogeochemical processes tied to that respective variable. Pearson's Product Moment Correlation Coefficient (PPMCC) was used to examine the strength of the association between pCO_2 and controlling variables and assess model performance in relation to other studies (Asuero et al., 2006). The strength of the

correlation between the two variables (r) is related to the goodness of fit of the linear regression model (Supplementary Table B.2). Analysis of Variance (ANOVA) was performed in R to compare the mean pCO_2 and CO_2 Flux between regions and years. Tukey's honestly significant difference (HSD) test was used to identify and quantify which ANOVA comparisons are statistically different.

3.4 Results

3.4.1 Surface Water Temperature and Salinity

In general, surface water temperature increased as the ship moved from higher salinity waters (S ~25; T = 9C) towards local river mouths (S < 10; T up to 20°C; Figure 3.2). Maximum surface salinity values reached S ≈ 31 were found in Hudson Bay open waters (Figure 3.2). Throughout the cruise the water column was generally stratified, with a mean mixed-layer depth exceeding 2m (Bouchard et al. in prog.), indicating the measurements made by the underway system were capturing the surface mixed layer.

To assist in identifying trends within the dataset, the study region was subdivided into three sub-domains with distinct temperature and salinity water properties (Figure 3.3, Table 3.2). The James Bay region comprises the area south of latitude 55°N and is characterized by relatively warm and fresh water; the Belcher Islands region is bounded by the 55°N James Bay boundary in the south and 81°W in the west, and is characterized by relatively uniform, cooler, and more saline waters. Finally, the southern Hudson Bay region extends north of 55°N and west of 81°W with a relatively wider range of cool, saline water as compared to the Belcher Islands region (Table 3.2).

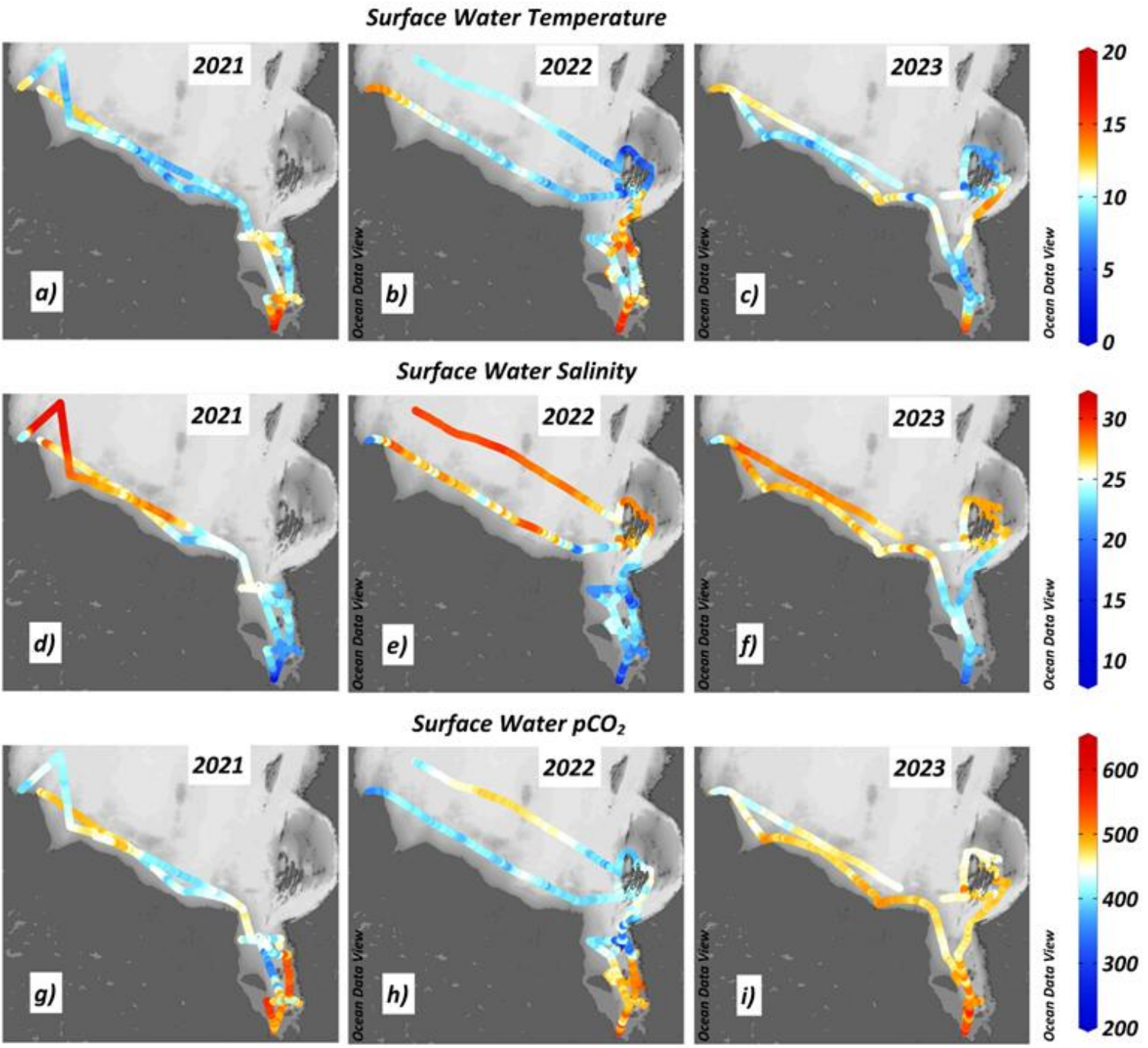

Figure 3.2: Summary of surface water properties from the James Bay Expeditions, 2021 – 2023, *as observed from the underway thermosalinograph and flow-through pCO_2 systems. (a – c) surface water temperature (°c) for 2021 – 2023 respectively; (d – f) water salinity for 2021 – 2023 respectively;(g – i) surface water pCO_2 (µatm) for 2021 – 2023 respectively.*

3.4.2 Surface Water Composition

3.4.2.1 Sea Ice Melt

Sea ice breakup dates (determined as < 15% sea ice concentration, see *Section 3.1.4*) were determined to be the first week of June in each year; however, only a rough estimate of sea ice breakup date is possible due to the under-performance of AMSR-2 in Hudson Bay (Ahmed et al., 2021). Weekly ice charts published in Forget et al. (2024) confirm in-situ observations of drift ice persisting near the shore in southern Hudson Bay, from Churchill River to the Winisk River in August 2022. These ice floes were likely remnants of the thick (>10 m), sediment-laden sea ice typically found in the area in June (Barber et al., 2021). The difficult navigation conditions presented by the ice floes in August 2022 account for the northerly deviation of the 2022 cruise track away from the southern Hudson Bay coast, relative to the other years (Figure 3.2). The sea ice also potentially contributes to the lower mean surface ocean temperature and salinity observed in 2022 relative to other years (Table 3.2). Across the entire region, mean surface water SIM contribution was calculated to be 0 % (± 4 %) in 2021, 2022, and 2023, with a maximum SIM contribute of 13 % observed in northwest James Bay in 2022.

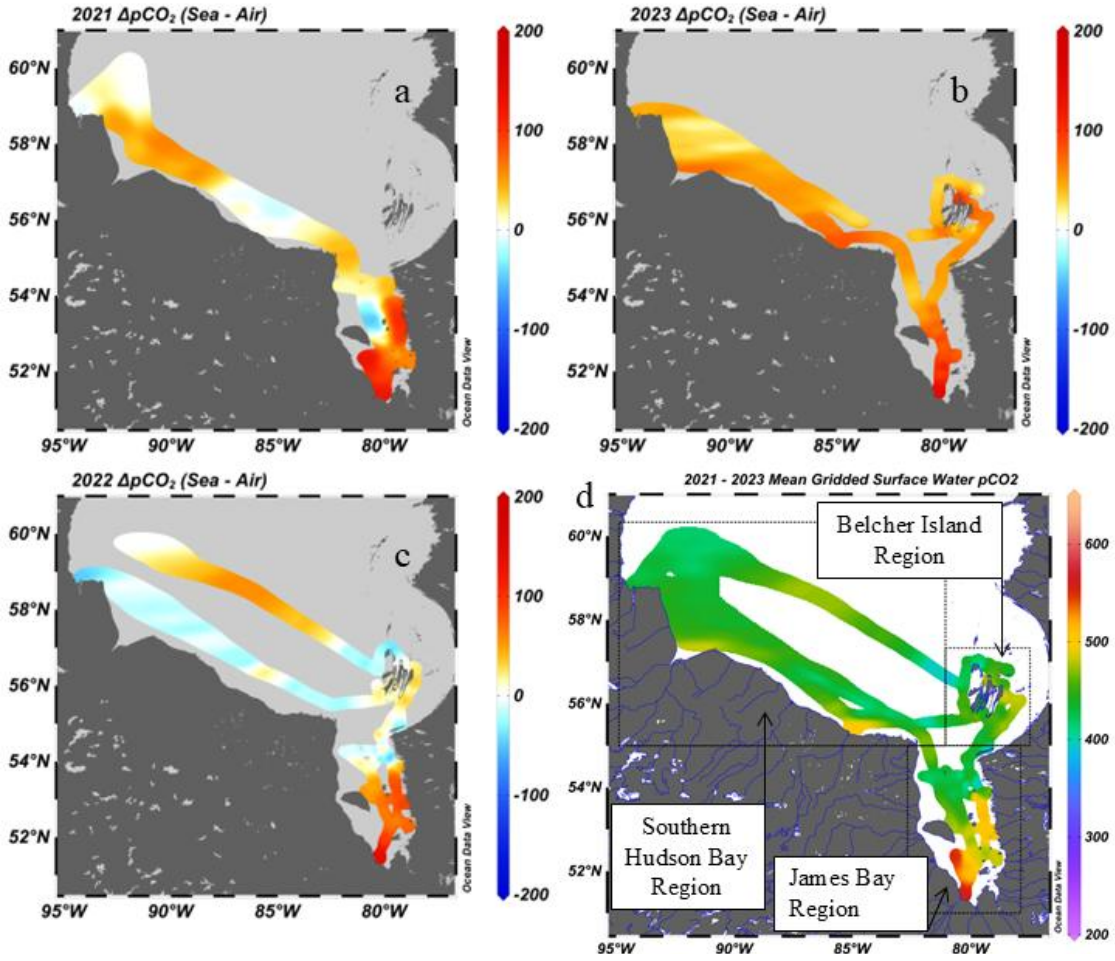

Figure 3.3: (a – c) Difference between seawater pCO_2 (µatm) and atmospheric CO_2 (414, 416, 417 ppm for 2021, 2022, and 2023, respectively (Lan et al., 2025). (d) Mean gridded surface water pCO_2 (µatm) for August of 2021 – 2023. Sub-regions indicated by dotted lines.

3.4.2.2 Meteoric Water

Meteoric water fractions were highest near the Winisk, Moose, and Eastmain Rivers (88 - 99% MW), decreasing to ≈30% meteoric water content at the centre of James Bay (Supplementary Figure B.1). The proportion of meteoric water decreased northwards from the southern end of James Bay, with a slightly higher amount found on the east side, where water is circulating northwards out of the bay (Ridenour et al., 2019). Given the low SIM fractions observed in each year, we can infer that low salinity observations from the underway TSG (Figure 3.2) were associated with increased meteoric water concentrations around the southern coast of James Bay where large rivers enter the bay (Moose River, Eastmain River; Figure 3.1) and along the east coast where La Grande River has its outlet (Figure 3.1). Elevated CDOM concentrations in these low-salinity coastal areas (Figure 3.4) confirm that this meteoric water is associated with low salinity observations, as rivers typically have much higher CDOM concentrations than seawater due to high CDOM inputs from terrestrial organic material (Granskog et al., 2007). CDOM and salinity observations also indicate increased river water presence in surface waters along the northeast coast of James Bay (20%), where surface water exits the bay and is advected northward towards the Belcher Islands (Supplementary Figure B.1). In contrast, along the northwest side of JB, where there is sometimes inflow from southern Hudson Bay (Ridenour et al., 2019), the maximum meteoric water content was 15% (Supplementary Figure B.1).

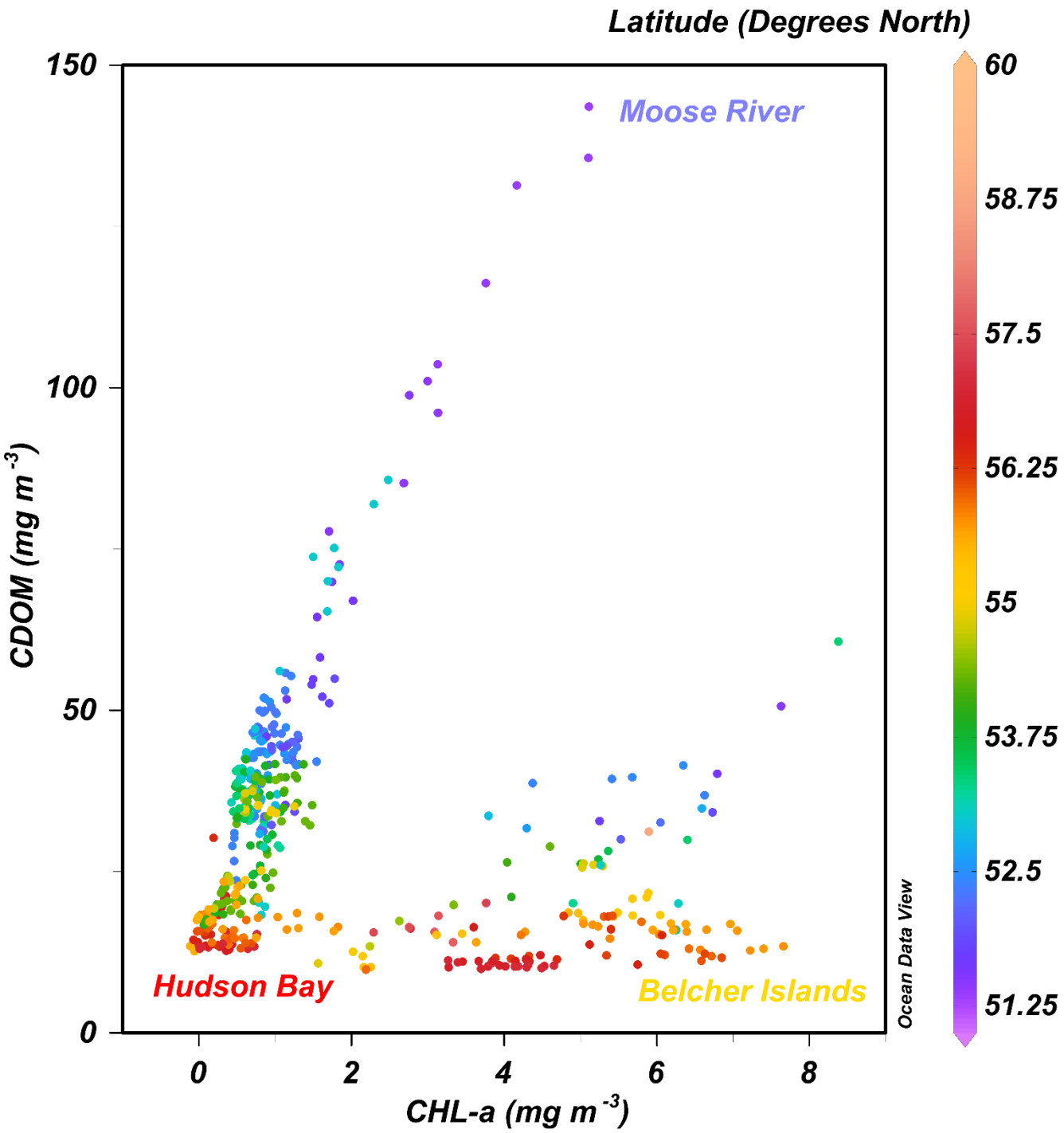

Figure 3.4: Surface water measurements of CHL-a (mg/m^3) and CDOM (mg/m^3), colored by Latitude. Two clear mixing lines are present. Northern observations near the Belcher Islands (red dots) have low CDOM at all CHL-a values, whereas southern observations from James Bay (purple, blue dots) fall along a mixing line between low CDOM, low CHL-a waters and high CDOM, medium CHL-a waters. These high CDOM, medium CHL-a data reflect direct terrestrial inputs from the Moose River. The high CHL-a medium CDOM measurements were taken at the center of James Bay, where primary production was high.

3.4.3 Surface Water pCO_2

3.4.3.1 Distribution, Trends, and Range of Surface Water pCO_2

Measured underway pCO_2 followed the distribution of temperature and salinity (inverse) in all years, where pCO_2 was positively correlated with water temperature and an inversely correlated with salinity. Observed surface water pCO_2 ranged from ~216 to 602 µatm over the study, while mean surface ocean pCO_2 exceeded atmospheric CO_2 concentration in each of the three years of observations (atmospheric average ≈ 417 ppm, Table 3.2; Lan et al., 2025). Higher pCO_2 measurements typically occurred near rivers, whereas low pCO_2, below atmospheric levels, were only occasionally observed in open Hudson Bay waters (Figure 3.3). ANOVA reveals surface water pCO_2 varied significantly both between regions and years, while Tukey HSD post-hoc analysis revealed pCO_2 varied significantly in intercomparisons between all regions and all years (Supplementary Table 3). Areas of low pCO_2 were generally found at the centre of James Bay across all three years; however, James Bay surface water pCO_2 (483.6 µatm ±55) was significantly higher than Southern Hudson Bay (445.0 µatm ±34) and the Belcher Islands (452.3 µatm ±36). Linear regression models examining the relationship between pCO_2 and temperature and salinity indicate a moderate relationship between both variables (R^2 = 0.24, RMSE = 41 µatm) with neither variable behaving as a stronger predictor for pCO_2 (Figure 3.6).

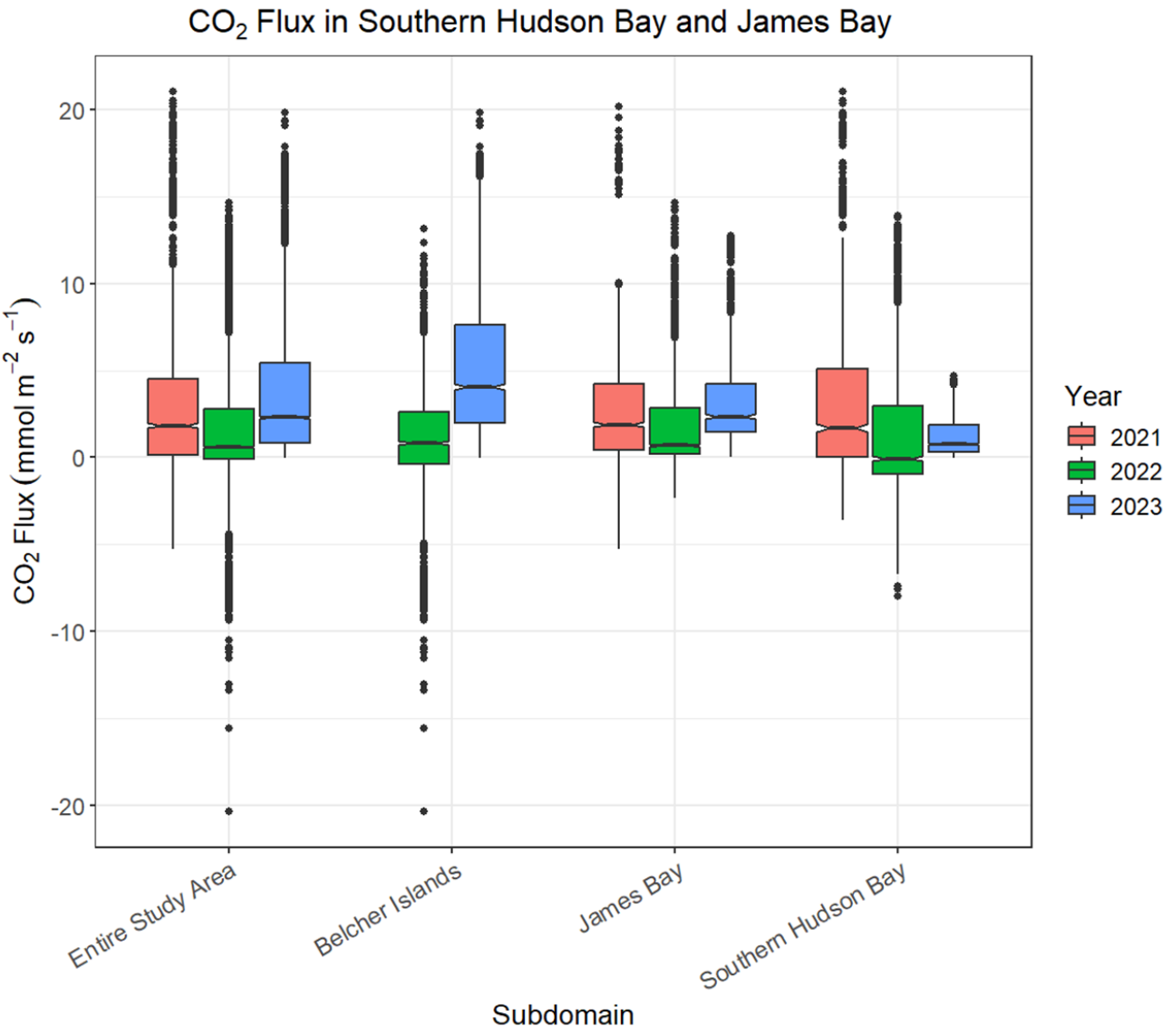

Figure 3.5: Box plots of CO_2 exchange (flux) as calculated for the 2021 – 2023 James Bay Expeditions. The middle line within each box is the mean of the dataset; the box itself represents the interquartile range; the whiskers represent the range of the data; and the dots represent outliers. Mean CO_2 flux was above 0 for all years and all regions indicating the region was a weak net CO_2 source to the atmosphere during the sampling periods.

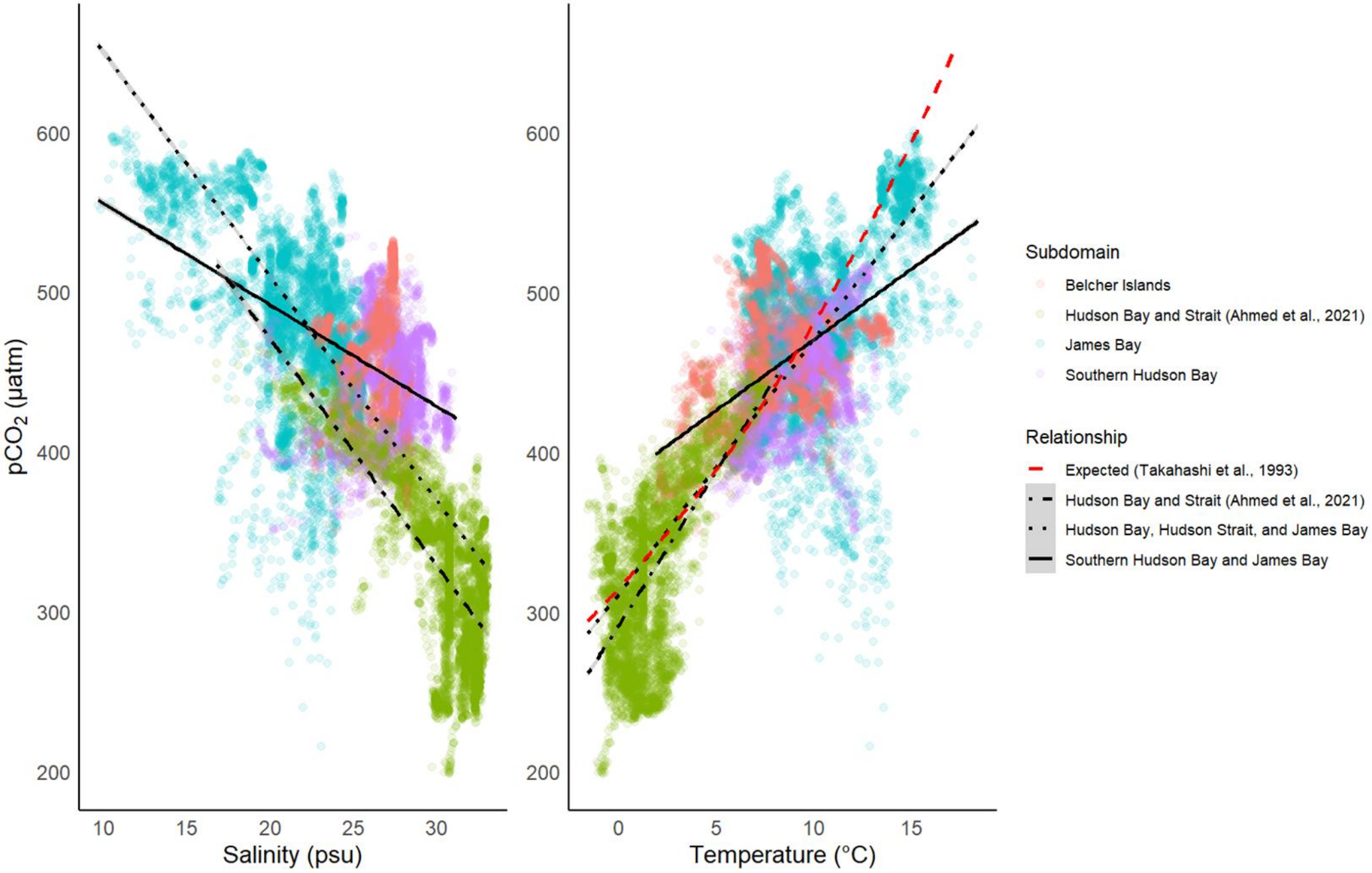

Figure 3.6: Linear regression models estimating the relationship between surface salinity and surface water temperature (°C) with surface water pCO_2 (µatm). The solid black line shows the relationships from this study. The expected relationship between temperature and pCO_2 (based on mean water temperature and pCO_2) is shown by the red dashed line (Takahashi et al., 1993). Relationships for observations from Hudson Bay and Hudson Strait in June 2020 (Ahmed et al., 2021) are shown with a black dashed-dotted line, while the relationships for the combined data set (current study and Ahmed et al. 2021) are shown with a black dotted line. Statistics are given in Table 4.

3.4.3.2 CO_2 Fluxes between the Ocean and Atmosphere

Our data indicate that Southern Hudson Bay and James Bay were, on average, weak CO_2 sources to the atmosphere during the study period but displayed considerable variability (Figure 3.5). ANOVA and Tukey HSD were used to identify significant differences between regional observations of CO_2 flux. Southern Hudson Bay was the weakest source of CO_2 while the Belcher Islands surface waters were the strongest CO_2 source across all years. Additionally, a statistically significant increase in CO_2 efflux (+4.3 mmol $m^{-2}d^{-1}$) was observed between 2022 and 2023 in Belcher Islands surface water (Supplementary table B.4). Generally, the mean summertime CO_2 effluxes were highest in 2023 (+3.7 ±3.7 mmol $m^{-2}d^{-1}$), lowest in 2022 (+1.5 ±3.3 mmol $m^{-2}d^{-1}$), with 2021 (+2.8 ±3.8 mmol $m^{-2}d^{-1}$) in between the two (Table 3.3).

Table 3.3: Comparison of CO_2 exchange between the sea and atmosphere in Southern Hudson Bay and James Bay (SHB-JB) and other northern marine regions.

Study	*Shelf Sea*	*Season*	*Mean Flux (mmol CO_2 $m^{-2}day^{-1}$)*
Murata & Takizawa (2003)	Beaufort Sea	Summer	-12.0 (± 3.6)
Else et al. (2008)	Hudson Bay	Fall	-0.7 (±0.4)
Burgers et al. (2017)	Canadian Arctic Archipelago and Baffin Bay	Summer (2013)	-12
		Summer (2014)	-3
Ahmed et al. (2021)	Hudson Bay and Hudson Strait	Spring – Early Summer	-5.1 (± 9.3)
This Study	Entire Study Area	Late Summer	2.5 (± 3.7)

3.4.3.3 Normalized pCO_2

As detailed in section *3.2.2.*, temperature effects on pCO_2 variability can be accounted for using pCO_{2Temp} and pCO_{2Net} (Figure 3.7). When of pCO_{2Temp} exceeds pCO_{2Net}, temperature variation dominates surface water pCO_2 variability. Areas with low pCO_{2Temp} and high pCO_{2Net} are influenced more strongly by factors other than temperature variation. Figure 3.7 identifies temperature as a dominant control on pCO_2 variability within southern James Bay and northern James Bay. Conversely, heightened pCO_{2Net} observations were made in surface water of at the centre of James Bay and surrounding much of the Belcher Islands. Here other processes contribute to pCO_2 variability to a greater degree than temperature.

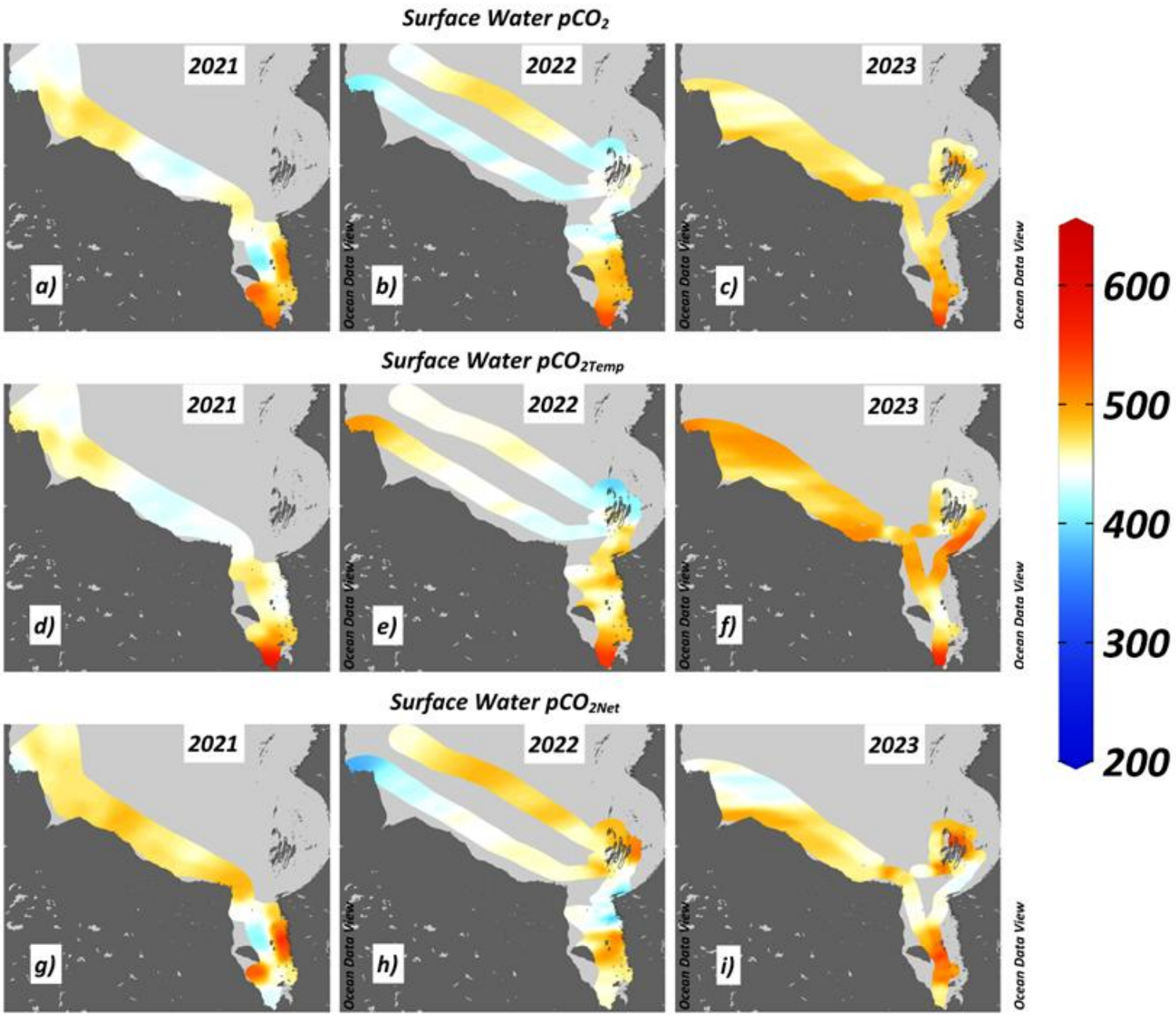

Figure 3.7: (a – c) Surface water pCO_2. (d – f) Surface water pCO_{2Temp}. (g – i) Surface water pCO_{2Net}. All units are µatm.

3.5 Discussion

Observations from this study identified that the Southern Hudson Bay and James Bay region was a weak source of CO_2 to the atmosphere during August of three consecutive years (2021, 2022, and 2023). These observations contrast with previous studies that found Hudson Bay and other Arctic coastal shelf environments to be CO_2 sinks (Table 3.3). In the following sections we examine the dominant controls on surface water pCO_2 in southern Hudson Bay and James Bay and compare our findings to similar study regions.

3.5.1 Temperature and Salinity Controls on Surface pCO_2

Temperature and salinity exhibit strong controls on surface water pCO_2 through their effect on the solubility of CO_2 in seawater. Cold, fresher water holds higher concentrations of dissolved gases. Previous studies within Hudson Bay identified relationships between surface water pCO_2 and temperature/salinity, with salinity having a higher correlation index (Ahmed et al., 2021; Else et al., 2008; Table 3.4). These past Hudson Bay observations are consistent with results from the Canadian Arctic Archipelago (Geilfus et al., 2018). Here, as expected, we also find correlations between temperature/salinity and surface ocean pCO_2 within all three of our subregions (Figure 3.6, Table 3.4). However, Ahmed et al. (2021) observed stronger relationships between Hudson Bay surface water pCO_2 and both temperature (r^2 = 0.42) or salinity (r^2 = 0.51) than we observed in this study (r^2 = 0.24; Table 3.4). It is notable that we experienced generally warmer waters (T = 1.9 – 18.5°C) during this study compared to the previous study (T = -1.8 – 11.1°C, Ahmed et al., 2021), likely due to a combination of both sampling later in the season (August vs. June-July) and lower latitude. Our data had a similar salinity range to Ahmed et al. (2021), however, the previous study followed shortly after sea-ice breakup and consequently had significant sea ice melt contributing to low salinity observations, whereas the bulk of our low salinity measurements were attributed to river inflow. Combining observations from the previous study and the current study together yields a stronger predictive relationship between both surface water temperature (r^2= 0.56, Table 3.4) or salinity (r^2= 0.56, Table 3.4) and pCO_2 than either study provides individually. This combined dataset represents a new region, comprised of Hudson Bay, James Bay, and Hudson Strait (HB-JB-HS, Table 3.4, Figure 3.6). Within HB-JB-HS, both temperature and salinity describe 56% of surface water pCO_2 variation, however, the Pearson Correlation Coefficient test identified temperature to have a stronger linear correlation with pCO_2 than salinity. Thus, 56% of surface water pCO_2 variation across the HB-JB-HS region can be predicted by surface water temperature variation.

Table 3.4: Summary of linear regression, root mean square error (RMSE), and Pearson's product moment correlation coefficient (PPMCC) analysis for all regions. Ahmed et al., (2021) subregion contains Hudson Bay and Hudson Strait.

Sub-Region		R^2	RMSE (µatm)	r (PPMCC)
All Data	T	0.24	41	0.49
	S	0.24	41	-0.49
Southern Hudson Bay	T	0.27	29	0.51
	S	0.02	33	0.13
James Bay	T	0.17	50	0.41
	S	0.29	46	-0.54
Belcher Islands	T	0.16	33	0.40
	S	0.01	35	-0.09
Ahmed et al. (2021)	T	0.42	39	0.65
	S	0.51	36	-0.71
Hudson Bay, James Bay, and Hudson Strait	T	0.56	44	0.83
	S	0.56	53	-0.75

More insight can be gained into temperature's control on surface water pCO_2 by normalizing the regional variability in pCO_2 to variability in measured temperature. Temperature effects on pCO_2 variability can be accounted for using pCO_{2Temp} (Figure 3.7). When pCO_{2Temp} exceeds pCO_{2Net}, temperature variation dominates surface water pCO_2 variability. Areas where pCO_{2Net} exceeds pCO_{2Temp} are influenced more strongly by factors other than temperature variation. Figure 3.7 identifies temperature as a dominant control on pCO_2 variability within southern James Bay. Conversely, the pCO_{2Net} at the centre of James Bay and surrounding much of the Belcher Islands exceeded pCO_{2Temp}, indicating that other processes contribute strongly to pCO_2 variability more than temperature.

For regions with $pCO_{2Temp} > pCO_{2Net}$, temperature variation and corresponding pCO_2 variation may be influenced by the proximity of rivers. For example, in Figure 3.7, peaks in the pCO_{2Temp} are evident during each year of the study when we were within the region of influence of the Moose River plume (Figure 3.7). Peaks in the pCO_{2Temp} are also evident in the area of influence of the Churchill River plume (all years), and near the Nelson River and Winisk River plumes in 2023.

For regions with $pCO_{2Temp} < pCO_{2Net}$, where other ecosystem processes exert additional influence on pCO_2 distributions than temperature variation, the centre of James Bay and the Belcher Islands stands out in 2022 and 2023, especially in contrast to the regions near river inflows (Figure 3.7). Surface water pCO_2 in these regions may be more strongly influenced by factors such as primary production, tidal mixing, and upwelling, and less influenced by temperature effects, as has been observed in the Canadian Arctic Archipelago and the sub-arctic

Atlantic Ocean, where seasonal biological controls overshadow the effects of temperature during the summer (Ahmed et al., 2019; Takahashi et al., 2002). Surface water pCO_2 in southern Hudson Bay also primarily reflects other (net) processes across all years (discussed further below), with the exception of 2023, when the pCO_{2Temp} indicates temperature was the dominant factor influencing pCO_2 variation.

3.5.2 "Net" effect of physical and biological processes on surface water pCO_2

The "net" effect of other processes on surface water pCO_2 (Eq. 3.5) captures the impact of processes other than temperature that contribute to variability in surface water pCO_2. These include biological processes such as primary production and respiration, changes in alkalinity due to freshwater addition, ocean mixing (via tides, wind, or upwelling), and air – sea exchange of CO_2 (Henson et al., 2018). By examining each of these processes independently, we attempt to identify which of these processes exert the most influence on pCO_2 within the southern Hudson Bay, James Bay, and the Belcher Islands areas.

3.5.2.1 Primary production and respiration

The biological pump decreases pCO_2 within the surface ocean as photosynthesis repackages CO_2 into organic matter and exports it below the mixed layer (Legendre, 2024). CHL-a and Fluorescent Dissolved Organic Matter (FDOM) concentrations have been used as proxies for primary production in other studies in the region (Ahmed et al., 2021). Here DO and CHL-a data collected from the ship's CTD also can be used here to investigate the impact of primary production on surface pCO_2 distributions. FDOM was not available in this study, but CDOM was used in its place, recognizing that river water dominates the CDOM signal near the coast and primary production signals are secondary (Granskog et al., 2007). Apparent Oxygen Utilization (AOU) may also serve as an indicator of biological activity; where positive AOU values represent oxygen (O_2) consumption (e.g. bacterial respiration), and negative AOU values represent O_2 production (e.g. photosynthesis). Oxygen data are not available for 2022.

CHL-a fluorescence measurements from the ship's CTD showed high (~5 mg m^{-3}) CHL-a near rivers, decreasing to ~2 mg m^{-3} at the centre of James Bay, before nearing 0 mg m^{-3} in surface water surrounding the Belcher Islands (Figure 3.4). At the centre of James Bay, pCO_2 was observed to be undersaturated in tandem with increased CHL-a concentrations, signalling significant biological activity within the area. Further, surface mixed layer AOU within the centre of James Bay was the lowest observed throughout the cruise. The strongly negative values indicate significant rates of O_2 production at the centre of James Bay. AOU increases both surrounding the Belcher Islands, and with proximity to river mouths, indicating O_2 consumption dominates over O_2 production in these areas. AOU was highest south of the Belcher Islands, coinciding with a region of heightened pCO_{2Net} (Figure 3.7), indicating respiration may be a dominant control on surface water pCO_2 around the Belcher Islands. Notably, neither AOU nor

CHL-a predict surface water pCO_2 with a high degree of accuracy in our study, compared with Ahmed et al., (2021), who found both CHL-a and FDOM to be minor predictors of surface water pCO_2 within central Hudson Bay and Hudson Strait. In contrast, our observations produce poor correlations between surface water pCO_2 and CDOM (R^2 = 0.19) or CHL-a (R^2 = 0.052) within the southern Hudson Bay and James Bay region. Likewise, while DO indicates areas of primary production and respiration, DO alone was found to be a poor predictor of surface water pCO_2 within southern Hudson Bay and James Bay (R^2 = 0.048).

3.5.2.2 Mixing

Physical mixing processes, such as those driven by winds or tides, may play an important role in Southern Hudson Bay as a potential driver of pCO_2 distributions. Wind-driven upwelling can bring deep, cold, saline water with high pCO_2 to the surface where it could result in a positive CO_2 flux to the atmosphere (Prinsenberg, 1986; Sarmiento & Gruber, 2006). Upwelling events have been observed in northern Hudson Bay during the spring, summer, and fall seasons (Ahmed et al., 2021; Prinsenberg, 1986). These consistent upwelling conditions are created by the prevailing westerlies, driving surface water away from the west coast of Hudson Bay (Ahmed et al., 2021). Wind-driven upwelling events may have occurred along the northeast shore of the Belcher Islands during the study period (Supplemental Figures B.2 & B.3), potentially contributing to conditions of increased pCO_{2Net} via vertical mixing (Figure 3.7). However, the region of heightened pCO_{2Net} around the southern Belcher Islands is inconsistent with the wind direction required to create upwelling in both 2022 and 2023. Another possible explanation for these observations is the strong M2 tide within Hudson Bay, with an amphidromic point near the Belcher Islands (Petrusevich et al., 2018). This tidal component creates a hotspot for internal wave activity towards the south east of the Belcher Islands, promoting vertical mixing due to the variability of seafloor bathymetry in the area (Petrusevich et al., 2018). Mixed layer depth observations from around the north and south-east of the Belcher Islands indicate a deeper mixed layer at these locations (Supplemental Figure B.4) supporting physical mixing processes as important drivers of pCO_2 variations.

3.5.2.3 Freshwater

Freshwater addition, either through sea ice melt or incoming river waters, can change surface ocean temperature, salinity, and alkalinity, potentially contributing to observations of heightened pCO_{2Net}. Freshwater addition to the surface ocean can dilute total alkalinity (TA) and dissolved inorganic carbon (DIC), impacting pCO_2 of the resulting mixture. For example, Burt et al. (2016) observed heightened TA (1870 µmol kg^{-1}, S = 0) within the Nelson River, while the TA of east Hudson Bay Rivers was considerably lower (689 µmol Kg^{-1}, S = 0). Assuming both rivers and sea surface are in equilibrium with the atmosphere (417 ppm, Figure 3.3), pCO_2 and TA can be used to determine DIC end-members for seawater (2096 µmol Kg^{-1}), the Nelson River (1879

µmol Kg^{-1}), and eastern Hudson Bay Rivers (710 µmol Kg^{-1}). Conservatively mixing equal parts of these two rivers with marine water from Hudson Bay (TA = 2251 µmol Kg^{-1}, S = 32) would result in two water masses: one with S = 16, TA = 2061 µmol Kg^{-1}, and DIC = 1988 µmol Kg^{-1} (Nelson River/seawater mixture) and one with S = 16, TA = 1470 µmol Kg^{-1}, and DIC = 1403 µmol Kg^{-1} (East Hudson Bay River/seawater mixture). Despite all three water masses beginning with the same pCO_2, the mixture has resulted in two greatly different pCO_2 values: 448 µatm for the eastern Hudson Bay mixture and 285 µatm for the east James Bay mixture. Because pCO_2 does not mix conservatively, under the right conditions freshwater mixing with seawater may decrease pCO_2. Alkalinity observations from the La Grande River mouth have been reported as low as ~26 µmol Kg^{-1} (Rosa et al., 2012), thus meteoric water mixing with seawater within this locale will result in in decreased surface water pCO_2, corresponding with increased pCO_{2Net} observations (Figure 3.7). This may help explain pCO_{2Net} observations near the centre of James Bay and near the La Grande River (Figure 3.7).

Although sea ice melt was not a major contributor to surface waters during our sampling, a non-proportional dilution of DIC and TA would be expected wherever there were SIM additions, akin to the effect of the La Grande River. Observations of first year sea ice indicates sea ice TA may average ~420 µmol Kg^{-1} and exceeds corresponding DIC concentrations of ~330 µmol Kg^{-1}, thereby diluting seawater TA and DIC disproportionately, ultimately contributing to a net decrease in pCO_2 (Burgers et al., 2023). Although not revealed by the freshwater fractions calculated in section 3.4.2, we suspect that additional sea ice melt was present in summer 2022 and, together with colder temperatures, offers some explanation for lower surface water pCO_2 across the entire sampling region in 2022 compared to the other two sampling years (Figure 3.3, Supplementary Figure B.1).

3.5.3 The Seasonal Cycle of pCO_2 in Hudson Bay and James Bay

Using Ahmed et al. (2021)'s spring observations and Else et al. (2008)'s fall observations, we propose a seasonal open-water cycle for pCO_2 in Hudson Bay and James Bay. Within this conceptual model, a central role is played by the high volumes of river discharge within the region and the long ice-free season, with allows pronounced surface heating (Bruneau et al., 2025; Soriot et al., 2025). While seasonal processes such as primary production within polynyas or freshwater addition through sea ice melt have been observed to drive down surface water pCO_2, river discharge has been observed to exert the opposite effect on surface water pCO_2 (Ahmed et al., 2021; Else et al., 2008). We propose that, within Hudson Bay estuaries and river plumes, increased temperatures and the delivery of riverine carbon drives pCO_2 oversaturation in the spring, summer, and fall (Ahmed et al., 2021; Else et al., 2008). As the water temperature increases in the summer, surface water pCO_2 increases accordingly, peaking in the late summer to early fall. This proposed seasonal trend of surface water pCO_2 in Hudson Bay (i.e., increasing during the summer months) is *opposite* what has reported for the Baltic Sea (Schernewski et al.,

2011), parts of the Canadian Arctic Archipelago (Geilfus et al., 2018), and the global ocean (Takahashi et al., 2002). Within these other Arctic and sub-Arctic shelf seas, spring algal blooms draw down pCO_2 in the early summer months, and nitrogen fixation contributes to further decrease in total CO_2 concentration in surface water as summer progresses (Schernewski et al., 2011). Geilfus et al. (2018) made a similar observation in surface water pCO_2 in Coronation Gulf in the southwestern CAA during the summer. Here they saw that pCO_2 increased above atmospheric levels, corresponding with an increase in temperature and a decrease in salinity due to river input, similar to the trends observed for Hudson Bay and James Bay.

3.6 Conclusions

Surface water pCO_2 within southern Hudson Bay and James Bay is highly variable in summer and the region acted as a CO_2 source to the atmosphere in all three years visited. The mean calculated CO_2 fluxes from the ocean to the atmosphere were +2.8 ±3.8, +1.5 ±3.3, and +3.7 ±3.7 mmol CO_2 m^{-2} d^{-1} for 2021, 2022, and 2023, respectively. These observations are in contrast to other Arctic shelf seas (Canadian Arctic Archipelago, Beaufort Sea) which have been shown to be CO_2 sinks in summer (August, Geilfus et al., 2018; Murata & Takizawa, 2003). Increased seawater temperatures (due to the influence of rivers) over our study period, relative to historical studies, may explain the region's status as a CO_2 source to the atmosphere during our study.

Surface water pCO_2 within southern Hudson Bay and James Bay is governed by many processes, as such, neither temperature nor salinity were found to be strong predictors for pCO_2 across this region. However, when combined with data from Hudson Strait and northern Hudson Bay, temperature described the bulk of the pCO_2 variation across the broader region. Despite temperature's strong influence over surface water pCO_2, additional physical and biological factors play important roles in the determination of surface water pCO_2, especially around the Belcher Islands and in James Bay. Physical mixing driven by wind and tides may be an important contributor to pCO_2 distributions around the Belcher Islands, resulting in increased pCO_2 around the Islands relative to nearby areas. Likewise biological activity within James Bay draws down pCO_2 in the surface water, contributing to decreased surface pCO_2 compared to Hudson Bay. As temperature exerts a strong influence on surface water pCO_2, it may occasionally mask other processes, thus high-resolution regional examinations of the carbonate system is warranted to properly understand local carbonate system drivers.

Due to their position further south than other arctic shelf seas, Hudson Bay and James Bay are experiencing the impacts of anthropogenic climate change (increased river runoff, permafrost thaw, shorter sea ice period) sooner than other regions (Déry et al., 2016; McLaughlin & Packalen, 2021; Soriot et al., 2025; Vonk et al., 2025). As such, Hudson Bay and James Bay may serve as model systems to better understand how these changes will impact higher Arctic regions as they experience warming. As evidenced by the variability of controls on surface water pCO_2 in Southern Hudson Bay and James Bay in the summer months, high resolution regional and seasonal carbonate system measurements will be needed to fully understand how the SHBJB carbon system will respond to further climate change. Future work within this region should seek to extend our knowledge of James Bay's carbonate system to spring and summer months. Additionally, future work should seek to solidify the causes of local mixing and to quantify the interaction of the Hudson Bay deep water on the surface water carbonate system of southern Hudson Bay and James Bay.

3.7 References

Ahmed, M., Else, B. G. T., Butterworth, B., Capelle, D. W., Guéguen, C., Miller, L. A., Meilleur, C., & Papakyriakou, T. (2021). Widespread surface water pCO_2 undersaturation during ice-melt season in an Arctic continental shelf sea (Hudson Bay, Canada). *Elementa*, *9*(1). https://doi.org/10.1525/elementa.2020.00130

Ahmed, M., Else, B. G. T., Capelle, D., Miller, L. A., & Papakyriakou, T. (2020). Underestimation of surface pCO_2 and air-sea CO_2 fluxes due to freshwater stratification in an Arctic shelf sea, Hudson Bay. *Elementa*, *8*(1). https://doi.org/10.1525/elementa.084

Arruda, R., Dariia Atamanchuk, Margot Cronin, Tobias Steinhoff, & Douglas W. R. Wallace. (2019). At-sea intercomparison of three underway pCO2 systems. *Limnology and Oceanography: Methods*, *18*(2), 63–76. https://doi.org/https://doi.org/10.1002/lom3.10346

Asuero, A. G., Sayago, A., & González, A. G. (2006). The Correlation Coefficient: An Overview. *Critical Reviews in Analytical Chemistry*, *36*(1), 41–59. https://doi.org/10.1080/10408340500526766

Ausen, E. L., Redirchuk, G., Mundy, C. J., Ehn, J., & Kuzyk, Z. (2023). James Bay Expedition 2022-Cruise Report July 20–August 24, 2022. *Centre for Earth Observation Science (CEOS), University of Manitoba*, 73 pp. and Appendices A-G. https://doi.org/https://doi.org/10.34992/v3a3-f760

Barber, D. G., Harasyn, M. L., Babb, D. G., Capelle, D., McCullough, G., Dalman, L. A., Matthes, L. C., Ehn, J. K., Kirillov, S., Kuzyk, Z., Basu, A., Fayak, M., Schembri, S., Papkyriakou, T., Ahmed, M. M. M., Else, B., Guéguen, C., Meilleur, C., Dmitrenko, I., … Sydor, K. (2021). Sediment-laden sea ice in southern Hudson Bay: Entrainment, transport, and biogeochemical implications. *Elementa: Science of the Anthropocene*, *9*(1), 00108. https://doi.org/10.1525/elementa.2020.00108

Bates, N. R., & Mathis, J. T. (2009). *The Arctic Ocean marine carbon cycle: Evaluation of air-sea CO2 exchanges, ocean acidification impacts and potential feedbacks*.

Bruneau, J. A., Ehn, J. K., Kuzyk, Z. Z. A., Crawford, A. D., & Leblanc, M. L. (2025). Step change in sea surface temperatures brings marine heat waves to sub-Arctic James Bay, Canada. *Frontiers in Marine Science*, *12*, 1549329. https://doi.org/10.3389/fmars.2025.1549329

Burgers, T. M., Miller, L. A., Rysgaard, S., Mortensen, J., Else, B., Tremblay, J. -É., & Papakyriakou, T. (2023). Distinguishing Physical and Biological Controls on the Carbon Dynamics in a High-Arctic Outlet Strait. *Journal of Geophysical Research: Oceans*, *128*(3), e2022JC019393. https://doi.org/10.1029/2022JC019393

Burgers, T. M., Miller, L. A., Thomas, H., Else, B. G. T., Gosselin, M., & Papakyriakou, T. (2017). Surface Water pCO_2 Variations and Sea-Air CO_2 Fluxes During Summer in the Eastern Canadian Arctic. *Journal of Geophysical Research: Oceans*, *122*(12), 9663–9678. https://doi.org/10.1002/2017JC013250

Burt, W. J., Thomas, H., Miller, L. A., Granskog, M. A., Papakyriakou, T. N., & Pengelly, L. (2016). Inorganic carbon cycling and biogeochemical processes in an Arctic inland sea (Hudson Bay). *Biogeosciences*, *13*(16), 4659–4671. https://doi.org/10.5194/bg-13-4659-2016

de Groot, P. A. (Ed.). (2004). *Handbook of Stable Isotope Analytical Techniques* (Vol. 1). Elsevier.

Déry, S. J., Stadnyk, T. A., MacDonald, M. K., & Gauli-Sharma, B. (2016). Recent trends and variability in river discharge across northern Canada. *Hydrology and Earth System Sciences*, *20*(12), 4801–4818. https://doi.org/10.5194/hess-20-4801-2016

Doney, S. C., Fabry, V. J., Feely, R. A., & Kleypas, J. A. (2009). Ocean Acidification: The Other CO_2 Problem. *Annual Review of Marine Science*, *1*(1), 169–192. https://doi.org/10.1146/annurev.marine.010908.163834

Else, B. G. T., Papakyriakou, T. N., Granskog, M. A., & Yackel, J. J. (2008). Observations of sea surface fCO_2 distributions and estimated air-sea CO_2 fluxes in the Hudson Bay region (Canada) during the open water season. *Journal of Geophysical Research: Oceans*, *113*(8). https://doi.org/10.1029/2007JC004389

Friedlingstein, P., O'Sullivan, M., Jones, M. W., Andrew, R. M., Bakker, D. C. E., Hauck, J., Landschützer, P., Le Quéré, C., Luijkx, I. T., Peters, G. P., Peters, W., Pongratz, J., Schwingshackl, C., Sitch, S., Canadell, J. G., Ciais, P., Jackson, R. B., Alin, S. R., Anthoni, P., … Zheng, B. (2023). Global Carbon Budget 2023. *Earth System Science Data*, *15*(12), 5301–5369. https://doi.org/10.5194/essd-15-5301-2023

Friedlingstein, P., O'Sullivan, M., Jones, M. W., Andrew, R. M., Hauck, J., Landschützer, P., Le Quéré, C., Li, H., Luijkx, I. T., Olsen, A., Peters, G. P., Peters, W., Pongratz, J., Schwingshackl, C., Sitch, S., Canadell, J. G., Ciais, P., Jackson, R. B., Alin, S. R., … Zeng, J. (2025). Global Carbon Budget 2024. *Earth System Science Data*, *17*(3), 965–1039. https://doi.org/10.5194/essd-17-965-2025

Gagnon, A., & Gough, W. (2006). Eastwest asymmetry in long-term trends of landfast ice thickness in the Hudson Bay region, Canada. *Climate Research*, *32*, 177–186. https://doi.org/10.3354/cr032177

Geilfus, N.-X., Pind, M. L., Else, B. G. T., Galley, R. J., Miller, L. A., Thomas, H., Gosselin, M., Rysgaard, S., Wang, F., & Papakyriakou, T. N. (2018). Spatial and temporal variability of seawater pCO2 within the Canadian Arctic Archipelago and Baffin Bay during the summer and autumn 2011. *Continental Shelf Research*, *156*, 1–10. https://doi.org/10.1016/j.csr.2018.01.006

Granskog, M. A., Kuzyk, Z. Z. A., Azetsu-Scott, K., & Macdonald, R. W. (2011). Distributions of runoff, sea-ice melt and brine using δ18o and salinity data—A new view on freshwater cycling in hudson bay. *Journal of Marine Systems*, *88*(3), 362–374. https://doi.org/10.1016/j.jmarsys.2011.03.011

Granskog, M. A., Macdonald, R. W., Mundy, C. J., & Barber, D. G. (2007). Distribution, characteristics and potential impacts of chromophoric dissolved organic matter (CDOM)

in Hudson Strait and Hudson Bay, Canada. *Continental Shelf Research*, *27*(15), 2032–2050. https://doi.org/10.1016/j.csr.2007.05.001

Henson, S. A., Humphreys, M. P., Land, P. E., Shutler, J. D., Goddijn-Murphy, L., & Warren, M. (2018). Controls on Open-Ocean North Atlantic Δ p CO_2 at Seasonal and Interannual Time Scales Are Different. *Geophysical Research Letters*, *45*(17), 9067–9076. https://doi.org/10.1029/2018GL078797

Jakobsson, M. (2002). Hypsometry and volume of the Arctic Ocean and its constituent seas. *Geochemistry, Geophysics, Geosystems*, *3*(5), 1–18. https://doi.org/10.1029/2001gc000302

Kamula, M., Kuzyk, Z., & Mundy, C. J. (2022). *James Bay Expedition abord the William Kennedy—Cruise Report 1—17 August 2021*. Centre for Earth Observation Science (CEOS).

Lan, X., Tans, P., & K.W. Thoning. (2025). *Trends in globally-averaged CO2 determined from NOAA Global Monitoring Laboratory measurements.* (Versions 2025-03) [Dataset]. https://doi.org/https://doi.org/10.15138/9N0H-ZH07

Landy, J. C., Ehn, J. K., Babb, D. G., Thériault, N., & Barber, D. G. (2017). Sea ice thickness in the Eastern Canadian Arctic: Hudson Bay Complex & Baffin Bay. *Remote Sensing of Environment*, *200*, 281–294. https://doi.org/10.1016/j.rse.2017.08.019

Legendre, L. (2024). Jigsaw puzzle of the interwoven biologically-driven ocean carbon pumps. *Progress in Oceanography*, *229*, 103338. https://doi.org/10.1016/j.pocean.2024.103338

MacGilchrist, G. A., Naveira Garabato, A. C., Tsubouchi, T., Bacon, S., Torres-Valdés, S., & Azetsu-Scott, K. (2014). The Arctic Ocean carbon sink. *Deep Sea Research Part I: Oceanographic Research Papers*, *86*, 39–55. https://doi.org/10.1016/j.dsr.2014.01.002

Markus, T., Stroeve, J. C., & Miller, J. (2009). Recent changes in Arctic sea ice melt onset, freezeup, and melt season length. *Journal of Geophysical Research: Oceans*, *114*(C12), 2009JC005436. https://doi.org/10.1029/2009JC005436

Martini, I. (1986). *Canadian Inland Seas* (1986th ed.). Elsevier.

McLaughlin, J. W., & Packalen, M. S. (2021). Peat Carbon Vulnerability to Projected Climate Warming in the Hudson Bay Lowlands, Canada: A Decision Support Tool for Land Use Planning in Peatland Dominated Landscapes. *Frontiers in Earth Science*, *9*, 650662. https://doi.org/10.3389/feart.2021.650662

Mesinger, F., DiMego, G., Kalnay, E., Mitchell, K., Shafran, P. C., Ebisuzaki, W., Jović, D., Woollen, J., Rogers, E., Berbery, E. H., Ek, M. B., Fan, Y., Grumbine, R., Higgins, W., Li, H., Lin, Y., Manikin, G., Parrish, D., & Shi, W. (2006). North American Regional Reanalysis. *Bulletin of the American Meteorological Society*, *87*(3), 343–360. https://doi.org/10.1175/BAMS-87-3-343

Mundy, C. J., Yezhova, Y., & Lengsavath, K. (2024). *RV William Kennedy Cruise Report July 31–September 1, 2023*. Centre for Earth Observation Science (CEOS).

Murata, A., & Takizawa, T. (2003). Summertime CO2 sinks in shelf and slope waters of the western Arctic Ocean. *Continental Shelf Research*, *23*(8), 753–776. https://doi.org/10.1016/S0278-4343(03)00046-3

Nielsen, D. M., Chegini, F., Maerz, J., Brune, S., Mathis, M., Dobrynin, M., Baehr, J., Brovkin, V., & Ilyina, T. (2024). Reduced Arctic Ocean CO2 uptake due to coastal permafrost erosion. *Nature Climate Change*, *14*(9), 968–975. https://doi.org/10.1038/s41558-024-02074-3

Ostlund, H. G., & Hut, G. (1984). Arctic Ocean Water Mass Balance from Isotope Data. *Journal of Geophysical Research*, *89*(C4), 6373–6381. https://doi.org/10.1029/JC089iC04p06373

Packalen, M. S., Finkelstein, S. A., & McLaughlin, J. W. (2014). Carbon storage and potential methane production in the Hudson Bay Lowlands since mid-Holocene peat initiation. *Nature Communications*, *5*. https://doi.org/10.1038/ncomms5078

Paustian, K., Six, J., Elliott, E. T., & Hunt, H. W. (2000). Management options for reducing CO_2 emissions from agricultural soils. *Biogeochemistry*, *48*(1), 147–163. https://doi.org/10.1023/A:1006271331703

Petrusevich, V. Y., Dmitrenko, I. A., Kozlov, I. E., Kirillov, S. A., Kuzyk, Z. Z. A., Komarov, A. S., Heath, J. P., Barber, D. G., & Ehn, J. K. (2018). Tidally-generated internal waves in Southeast Hudson Bay. *Continental Shelf Research*, *167*, 65–76. https://doi.org/10.1016/j.csr.2018.08.002

Prinsenberg, S. J. (1986). *The ciculation pattern and current structure of Hudson Bay*. *Elsevier Oceanography*, 187–204.

Prinsenberg, S. J. (1988). Ice-Cover and Ice-Ridge Contributions to the Freshwater Contents of Hudson Bay and Foxe Basin. *ARCTIC*, *41*(1), 6–11. https://doi.org/10.14430/arctic1686

Ridenour, N. A., Hu, X., Sydor, K., Myers, P. G., & Barber, D. G. (2019). Revisiting the Circulation of Hudson Bay: Evidence for a Seasonal Pattern. *Geophysical Research Letters*, *46*(7), 3891–3899. https://doi.org/10.1029/2019GL082344

Roch, M., Brandt, P., & Schmidtko, S. (2023). Recent large-scale mixed layer and vertical stratification maxima changes. *Frontiers in Marine Science*, *10*, 1277316. https://doi.org/10.3389/fmars.2023.1277316

Rosa, E., Gaillardet, J., Hillaire-Marcel, C., Hélie, J.-F., & Richard, L.-F. (2012). Rock denudation rates and organic carbon exports along a latitudinal gradient in the Hudson, James, and Ungava bays watershed. *Canadian Journal of Earth Sciences*, *49*(6), 742–757. https://doi.org/10.1139/e2012-021

Sarmiento, J. L., & Gruber, N. (2006). *Ocean biogeochemical dynamics*. Princeton University Press.

Schernewski, G., Hofstede, J., & Neumann, T. (Eds.). (2011). *Global Change and Baltic Coastal Zones*. Springer Netherlands. https://doi.org/10.1007/978-94-007-0400-8

Schuur, E. A. G., McGuire, A. D., Schädel, C., Grosse, G., Harden, J. W., Hayes, D. J., Hugelius, G., Koven, C. D., Kuhry, P., Lawrence, D. M., Natali, S. M., Olefeldt, D., Romanovsky, V. E.,

Schaefer, K., Turetsky, M. R., Treat, C. C., & Vonk, J. E. (2015). Climate change and the permafrost carbon feedback. *Nature*, *520*(7546), 171–179. https://doi.org/10.1038/nature14338

Soriot, C., Stroeve, J., & Crawford, A. (2025). Record Early Sea Ice Loss in Southeastern Hudson Bay in Spring 2024. *Geophysical Research Letters*, *52*(4), e2024GL112584. https://doi.org/10.1029/2024GL112584

Spreen, G., Kaleschke, L., & Heygster, G. (2008). Sea ice remote sensing using AMSR-E 89-GHz channels. *Journal of Geophysical Research: Oceans*, *113*(C2), 2005JC003384. https://doi.org/10.1029/2005JC003384

Takahashi, T., Sutherland, S. C., Sweeney, C., Poisson, A., Metzl, N., Tilbrook, B., Bates, N., Wanninkhof, R., Feely, R. A., Sabine, C., Olafsson, J., & Nojiri, Y. (2002). Global sea-air CO 2 flux based on climatological surface ocean pCO 2 , and seasonal biological and temperature effects. *Deep-Sea Research II*, *49*, 1601–1622.

Takahashi, T., Sutherland, S. C., Wanninkhof, R., Sweeney, C., Feely, R. A., Chipman, D. W., Hales, B., Friederich, G., Chavez, F., Sabine, C., Watson, A., Bakker, D. C. E., Schuster, U., Metzl, N., Yoshikawa-Inoue, H., Ishii, M., Midorikawa, T., Nojiri, Y., Körtzinger, A., … De Baar, H. J. W. (2009). Climatological mean and decadal change in surface ocean pCO2, and net sea–air CO2 flux over the global oceans. *Deep Sea Research Part II: Topical Studies in Oceanography*, *56*(8–10), 554–577. https://doi.org/10.1016/j.dsr2.2008.12.009

Tarnocai, C. (2006). The effect of climate change on carbon in Canadian peatlands. *Global and Planetary Change*, *53*(4), 222–232. https://doi.org/10.1016/j.gloplacha.2006.03.012

Virkkala, A.-M., Rogers, B. M., Watts, J. D., Arndt, K. A., Potter, S., Wargowsky, I., Schuur, E. A. G., See, C. R., Mauritz, M., Boike, J., Bret-Harte, M. S., Burke, E. J., Burrell, A., Chae, N., Chatterjee, A., Chevallier, F., Christensen, T. R., Commane, R., Dolman, H., … Natali, S. M. (2025). Wildfires offset the increasing but spatially heterogeneous Arctic–boreal CO2 uptake. *Nature Climate Change*, *15*(2), 188–195. https://doi.org/10.1038/s41558-024-02234-5

Vonk, J. E., Fritz, M., Speetjens, N. J., Babin, M., Bartsch, A., Basso, L. S., Bröder, L., Göckede, M., Gustafsson, Ö., Hugelius, G., Irrgang, A. M., Juhls, B., Kuhn, M. A., Lantuit, H., Manizza, M., Martens, J., O'Regan, M., Suslova, A., Tank, S. E., … Zolkos, S. (2025). The land–ocean Arctic carbon cycle. *Nature Reviews Earth & Environment*, *6*(2), 86–105. https://doi.org/10.1038/s43017-024-00627-w

Wanninkhof, R. (2014). Relationship between wind speed and gas exchange over the ocean revisited. *Limnology and Oceanography: Methods*, *12*(6), 351–362. https://doi.org/10.4319/lom.2014.12.351

Weiss, R. F. (1974). Carbon dioxide in water and seawater: The solubility of a non-ideal gas. *Marine Chemistry*, *2*(3), 203–215. https://doi.org/10.1016/0304-4203(74)90015-2

Yasunaka, S., Manizza, M., Terhaar, J., Olsen, A., Yamaguchi, R., Landschützer, P., Watanabe, E., Carroll, D., Adiwira, H., Müller, J. D., & Hauck, J. (2023). An Assessment of CO_2 Uptake in the Arctic Ocean From 1985 to 2018. *Global Biogeochemical Cycles*, *37*(11), e2023GB007806. https://doi.org/10.1029/2023GB007806

Chapter 4: Riverine controls on widespread carbonate mineral under-saturation in James Bay

N. Decker[1], T. Papakyriakou[1], K. Azetsu-Scott[2], D. Capelle[3], Z. Kuzyk[1], C.J. Mundy[1], K. Yezhova[1], K. Brown[1]*

**Corresponding Author (deckern@myumanitoba.ca)*

[1]Centre for Earth Observation Science (CEOS), Department of Environment and Geography, University of Manitoba, Winnipeg, Manitoba, Canada

[2]Bedford Institute of Oceanography, Fisheries and Oceans Canada, Dartmouth, Nova Scotia

[3]Freshwater Institute, Fisheries and Oceans Canada, Winnipeg, Manitoba, Canada

Please see appendix A for the contributions of each collaborating author.

Abstract

Anthropogenic ocean acidification, brought on by increasing atmospheric carbon dioxide (CO_2) concentrations, poses a threat to ocean ecosystems through changes to the ocean's inorganic carbon system. Within the Arctic Ocean, this threat is amplified due to cool temperatures and low salinity, as these features support an enhanced capacity for CO_2 uptake from the atmosphere. Moreover, the Arctic Ocean's coastal domain is particularly sensitive to increased CO_2 due to additional inputs of carbon from land such as coastal erosion, rivers, permafrost thaw. For example, the Canadian Arctic peripheral seas - Hudson Bay and James Bay - receive 12% of Arctic river runoff, with a significant portion draining from the Hudson Bay Lowlands (HBL), a permafrost laden peatland estimated to store ~30 Pg of carbon. The impacts of this carbon input to Southern Hudson Bay and James Bay have yet to be quantified, however, as only a handful of studies have examined the Hudson Bay inorganic carbon system, and none have been conducted in James Bay. In this study, we present the first high resolution measurements of the James Bay inorganic carbon system while building on the previous studies in Southern Hudson Bay. Saturation states (Ω) of carbonate minerals (aragonite and calcite) were calculated using dissolved inorganic carbon (DIC) and total alkalinity (TA) samples collected during the James Bay Expeditions (August 2021, 2022, and 2023). These data provide a baseline understanding of the carbonate system of James Bay and the first examination of drivers of carbonate mineral saturation conditions. Within James Bay, Ω varied with proximity to river inflow. The saturation state of aragonite ($\Omega_{Aragonite}$) was < 1 (undersaturated) throughout James Bay's entire water column, while calcite saturation ($\Omega_{Calcite}$) remained > 1 outside rivers, contrasting with what has been reported for Hudson Bay. North of James Bay, $\Omega_{Aragonite}$ increased in surface waters creating a saturated ($\Omega > 1$) layer, approaching $\Omega = 1$ at ~25 m depth. Undersaturated conditions ($\Omega < 1$) within James Bay were attributed to large quantities of river water entering the bay, altering the seawater carbonate system. This work provides a baseline understanding of the James Bay inorganic carbon system by identifying the main drivers of calcium carbonate saturation state. Future work should further examine eastern and western James Bay river inputs to better understand how projected changes in discharge will further impact the ocean's capacity for CO_2 uptake, and ultimately, its corrosiveness to calcium carbonate shell formation.

4.1 Introduction

4.1.1 Background Information

Anthropogenic CO_2 emissions have led to a 40% increase in atmospheric CO_2 concentration since the industrial revolution (~1750; Gulev et al. 2023). Consequently, the concentration of CO_2 within the global ocean has increased, as the atmosphere and ocean attempt to seek an equilibrium state. This has been particularly acute in the Arctic Ocean, where cool temperatures and low salinity support an enhanced capacity for CO_2 uptake from the atmosphere (Terhaar et al., 2021). As a result, recent studies have documented both a decline in seawater pH and the saturation state of biologically important calcium carbonate minerals (aragonite and calcite) in the Arctic Ocean and several of its peripheral seas (Mathis et al., 2015; Terhaar et al., 2021; Zhang et al., 2020). This response is symptomatic of ocean acidification (AMAP, 2018) and has resulted in a global ocean pH reduction of 0.11 since the beginning of the industrial revolution (Jiang et al., 2019).

The Arctic Ocean has the potential to acidify more quickly than other oceans due to cold water temperature and relatively low salinity, which contribute to increase CO_2 solubility, promoting CO_2 uptake from the atmosphere. As such, surface waters within the Arctic Ocean may see a pH reduction of up to 0.5 units by 2100 (IPCC RCP8.5; AMAP, 2018); a greater reduction than is expected of the global surface ocean (0.3; IPCC RCP8.5; Jiang et al., 2019). Ocean acidification (and by extension pH reduction) is thus linked to the health of the ecosystem through the saturation state (Ω) of carbonate minerals ($CaCO_3$), aragonite (Ω_{Arag}) and calcite (Ω_{Cal}), which calcifying organisms (such as invertebrates or plankton) use to form their hard structures (Azevedo et al., 2015; Mathis et al., 2015; Niemi et al., 2021).

Ocean acidification is not alone in impacting Arctic Ocean ecosystems, but other seasonal and regional factors, such as changing sea-ice extent (Steiner et al., 2015), freshwater input (Markus et al., 2009), and water temperature (Brand et al., 2014), also contribute to variability in marine carbonate chemistry. This high heterogeneity is even more challenging given the limited regional and seasonal extent of observations (Mathis et al., 2015), particularly in the Arctic Ocean's peripheral seas, such as Hudson Bay and James Bay. There have been only a handful of studies over the past two decades examining the seawater carbonate system in Hudson Bay (e.g. Ahmed et al., 2020; Azetsu-Scott et al., 2014; Burt et al., 2016), while James Bay remains unstudied. As such, increasing observations of inorganic carbon system parameters in this region is both critical to understanding present changes and to predicting future responses to continued anthropogenic CO_2 emissions (Steiner et al., 2015).

4.2 Study Area

Hudson Bay and James Bay receive 12% of pan-arctic river input, accounting for 46% of total Canadian river runoff to the Arctic (Déry et al., 2011, 2016). Several large river watersheds drain into Hudson and James Bay (Figure 4.1) contributing to low surface salinity (HB average ~29 g kg^{-1}; Déry et al., 2016; Prinsenberg, 1986). Within Hudson Bay, salinity increases rapidly with depth until reaching ~33 salinity at 30m (Prinsenberg, 1986). While both Hudson and James Bay receive similar amounts of freshwater (388 and 326 km^3 yr^{-1}, respectively), the drainage basin area of Hudson Bay (~2575x10^3 km^2) is substantially larger than that of James Bay (~718 x10^3 km^2; Déry et al., 2011). James Bay is considerably shallower than Hudson Bay; mean depth of James Bay is 20m while mean depth in Hudson Bay is 125m (Kuzyk & Candlish, 2019). Maximum depth in Hudson Bay reaches 220m whereas James Bay's maximum depth is 60m (Kuzyk & Candlish, 2019). Baseline hydrographic conditions of James Bay were not available prior to the James Bay Expeditions (August 2021, 2022, and 2023; Kamula et al., 2022).

Seawater circulation in Hudson Bay is cyclonic (counter-clockwise) during the summer; water enters northern Hudson Bay from Foxe Basin and the north Atlantic Ocean via the Foxe Channel and Hudson Strait (Figure 4.1, Ridenour et al., 2019). Seawater circulates counter-clockwise around Hudson Bay, mixing with river water at the mouth of James Bay before circulating northwards past the Becher Islands before finally exiting back to the Atlantic Ocean (Ridenour et al., 2019). Hudson Bay and James Bay are seasonally covered with sea ice from late October to early June, with peak ice thickness in May (Gagnon & Gough, 2006; Landy et al., 2017). Sea ice thickness begins declining in James Bay briefly before Hudson Bay (Gagnon & Gough, 2006; Landy et al., 2017). Sea ice reaches a maximum thickness of 1 m in James Bay and 1.5 m in Hudson Bay, increasing with latitude (south – north) in James Bay and longitude (east – west) in Hudson Bay (Gagnon & Gough, 2006; Martini, 1986).

Upstream of Hudson Bay and James Bay lie the Hudson Bay Lowlands (HBL), the world's second largest peatland complex, estimated to hold 33 Gt of carbon as partially decomposed vegetation (Figure 4.1; Packalen et al., 2014). Climate warming induced permafrost thaw may trigger a strong positive climate feedback loop, whereby permafrost thaw leads to increased carbon emissions from HBL through 1) direct evasion to the atmosphere as carbon dioxide (CO_2) and methane (CH_4), and/or 2) by relocation of organic and inorganic carbon to the ocean by riverine transport (Schuur et al., 2015; Vonk et al., 2025; Vonk & Gustafsson, 2013). Hudson Bay and James Bay receive 17% of total DIC delivery to the Arctic each year, the second most among Arctic shelf regions (Vonk et al., 2025). The microbial and mechanical degradation of terrestrial carbon in the coastal ocean not only weakens the ocean's carbon uptake capacity, but also elevates the risk of ocean acidification (Bauer et al., 2013; Duarte et al., 2013; McGuire et al., 2009; Vonk & Gustafsson, 2013).

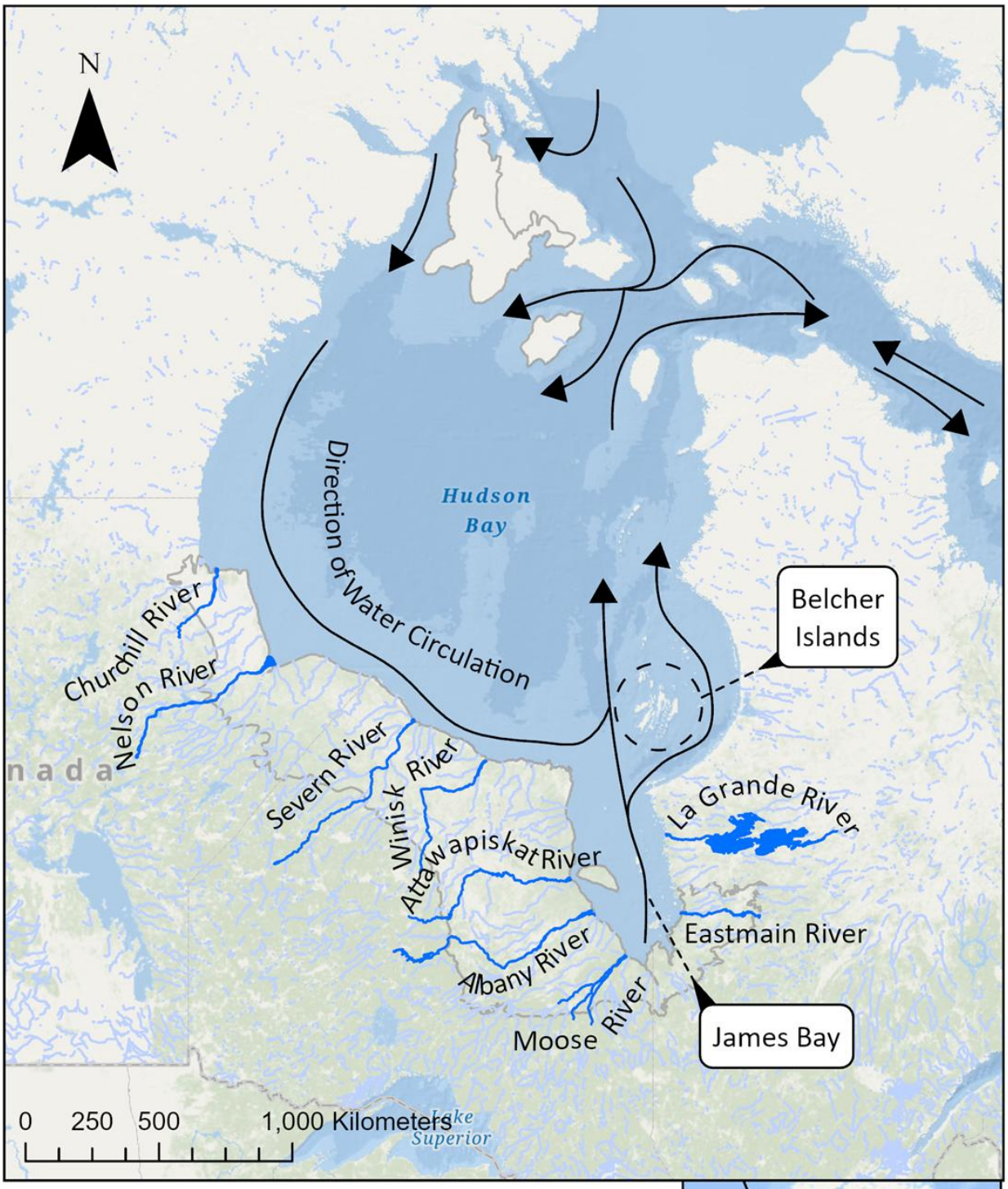

Figure 4.1: Hudson Bay, James Bay, and the Belcher Islands. Circulation pattern adapted from Ridenour et al., 2019. River boundaries adapted from Statistics Cananda 2016 census. Spatial Reference: Name: WGS 1984 Web Mercator Auxiliary Sphere, Map Units: Meter. Sources: Esri, TomTom, Garmin, GEBCO, National Geographic, NOAA, FAO, USGS, EPA, NRCan, Parks Canada, NaturalVue, and the GIS User Community

Both Hudson Bay and James Bay have experienced pronounced increases in air and water temperature (Brand et al., 2014; Bruneau et al., 2025), decreased sea ice cover period (Soriot et al., 2025), changing river inflow caused by climate change and damming (De Melo et al., 2022; Stadnyk et al., 2021), and elevated rates of shoreline permafrost erosion (Dredge & Dyke, 2020) that together with changing permafrost distribution and watershed hydrology can result in the mobilization and export of terrestrial carbon (organic and inorganic) to the marine system (Dredge & Dyke, 2020; Nielsen et al., 2024). These terrestrial inputs contribute to a highly heterogeneous marine carbonate system along Hudson Bay and James Bay coastlines. In particular, remineralization of organic carbon delivered by rivers can contribute to CO_2 accumulation and Ω undersaturation in coastal waters (Capelle et al., 2020). Marine primary production serves to offset the influx of inorganic carbon as autotrophic organisms (algae, phytoplankton) use nutrients, CO_2, and sunlight to produce organic matter within the upper water column. As this organic matter sinks and leaves the surface mixed layer, it is remineralized back into inorganic carbon, leading to CO_2 accumulation at depth.

Rivers draining into southern Hudson Bay and James Bay have different carbon chemistry depending on their geographic location. In particular, the rivers in the south and west of Hudson and James Bay drain the Hudson Bay Lowlands that contain vast peatlands underlain by glacio-lactustrine sediments over carbonate sedimentary formations (Dredge & Dyke, 2020). This gives rivers draining the south western section of HB & JB roughly three times the alkalinity relative to the rivers along the eastern coast that drain boreal soils over Precambrian Shield (Rosa et al., 2012; Azetsu-Scott et al., 2014; Burt et al., 2016). Azetsu-Scott et al. (2014) observed rivers flowing into the south-west of Hudson Bay contributed to decreased seawater Ω_{Arag} to an extent (1.50 vs 1.25) less than the rivers flowing into the south-east side of the bay and attributed these differences in river characteristics to differing watershed geology. Aragonite undersaturation ($\Omega_{Arag} < 1$) was observed in waters across Hudson Bay and Hudson Strait associated with surface waters with > 10% meteoric water, and in bottom waters, where organic matter remineralization rates were expected to be high (Azetsu-Scott et al., 2014). Azetsu-Scott et al. (2014) indicated that the Ω_{Arag} saturation horizon (i.e., the depth below which aragonite is undersaturated) for central Hudson Bay was estimated to be at ~50m depth but was observed to shoal within 20m-30m of the surface in southeastern Hudson Bay with this last observation based solely on one profile (Burt et al., 2016). While this previous research gives insights into river impacts on Hudson Bay, similar observations have yet to be documented in James Bay, as the most southerly sampling during previous studies extended only to the mouth of James Bay (e.g. Azetsu-Scott et al., 2014; Burt et al., 2016) .

In this study, we present the first high resolution measurements of the James Bay inorganic carbon system while building on the previous studies in Southern Hudson Bay. These data provide a baseline understanding of the carbonate system of James Bay and the first

examination of drivers of carbonate saturation conditions. Our goal is to determine the dominant controls on the saturation states (Ω) of carbonate minerals (aragonite and calcite) and ocean pH within the SHB & JB region, including the impacts of river input on marine carbonate chemistry. Establishing this observational baseline is essential to predict how ongoing climate change, including warming and increased river discharge, will impact the ocean's capacity for CO_2 uptake, and ultimately, its corrosiveness to calcium carbonate shell formation.

4.3 Methods

4.3.1 Collection

4.3.1.1 Bottled Water Collection

Sample collection took place in Southern Hudson Bay and James Bay on board the *RV William Kennedy* during the "James Bay Expeditions" (funded by NSERC, Oceans North, CMO-IOF, MEOPAR NCE, DFO, and ArcticNet NCE) carried out in August of 2021, 2022, and 2023 (detailed in Ausen et al., 2023; Kamula et al., 2022; Mundy et al., 2024). In all three years, water samples were collected either from 5L Niskin bottles arranged in a carousel (Sea-Bird Rosette) deployed off the ship's stern and equipped with a Sea-Bird 19+ V2 conductivity, temperature, and depth (CTD) profiler (see 2.1.2 below), or from single 5L Niskin bottles deployed from the zodiac. While the ship was underway, surface water samples were collected from a tap in the ship's laboratory that was continually fed from an intake on the ship's hull 2m below the sea surface.

Water sample collection followed practices outlined in Dickson et al. (2007). Collection from Niskin Bottles began immediately upon retrieval. Samples were collected using a clean piece of silicon tubing with any air bubbles removed. After rinsing each sample bottle with three times its volume, the bottles were filled carefully so as not to introduce any bubbles into the sample. Bottles were filled in the following order: pH (250ml Pyrex), total alkalinity (TA), and dissolved inorganic carbon (DIC; 500ml borosilicate glass bottle with ground stopper), then bulk water (500ml HDPE bottle). Bulk water was collected for subsampling of other physical and geochemical variables such as salinity and stable water isotopes ($\delta^{18}O$-H_2O).

DIC/TA bottles were immediately brought to the fume hood where 1% of the sample was removed to create a headspace, then the sample was preserved with 100 µL of saturated $HgCl_2$ solution. Using a 60ml syringe with silicon tubing, salinity and $\delta^{18}O$ were subsampled from the 500ml HDPE bottle into their respective bottles after three rinses. DIC/TA and salinity samples were stored in the dark at room temperature. Samples for the determination of $\delta^{18}O$ were stored at 4°C in the refrigerator. pH samples were protected from light and kept at room temperature for immediate analysis (2.2.1 *Water Sample Analysis*).

4.3.1.2 CTD Casts

The hydrography of Southern Hudson Bay, James Bay, and the Belcher Islands was determined using two Sea-Bird 19+ V2 CTDs, one mounted to the Rosette and one in a standalone configuration. Both CTDs were equipped with a Biospherical Instruments Inc. scalar photosynthetically active radiation (PAR) sensor (model QSP2350) and a Sea-Bird SBE 43 dissolved oxygen (DO) sensor. The Rosette mounted CTD included a SeaBird/WET Labs chlorophyll, CDOM, and phycoerythrin fluorometer (model FL3BAC), however, the fluorometer did not collect data during the 2023 field season. The CTD in standalone configuration was equipped with a WETStar fluorometer (WET Labs; model FLRT) for chlorophyll determination, a

model FLCDRT fluorometer (WETLabs) for CDOM determination, and a C-Star transmissometer (WETLabs; model CST) with a 25cm pathlength for transmissivity. The CTD in standalone configuration was deployed from the stern of the vessel between water collection casts to provide additional profile resolution. An RBRmaestro^3 Multi-Channel Logger and a SonTek CastAway CTD were also used to collect hydrographic data during zodiac operations.

4.3.2 Sample and Data Analysis

4.3.2.1 Water Sample Analysis

Samples for the determination of $\delta^{18}O$-H_2O (herein $\delta^{18}O$) were analysed at the University of Ottawa's Ján Veizer Stable Isotope Laboratory using a Finnigan MAT Delta plus XP + Gasbench (analysis precision ±2.0 ‰) following analytical methods outlined in de Groot (2004), $\delta^{18}O$ values are reported with respect to Vienna Standard Mean Ocean Water (V-SMOW). Salinity samples were analysed at the University of Manitoba (2021 and 2023) on a Guildline 8410A Portasal (± 0.003 accuracy) and at the University of Laval (Amundsen Science; 2022) on a Guildline 8400B Autosal (± 0.002 accuracy).

Inorganic carbon parameters, DIC and TA, were determined at Fisheries and Oceans Canada (2021 – Bedford Institute of Oceanography, Bedford, NS; 2022 and 2023 – Freshwater Institute, Winnipeg, MB) following procedures outlined in Dickson et al. (2007). Using a VINDTA 3C, DIC and TA were determined through titration of sample water. Precision of VINDTA 3C, based on replicate runs of seawater Certified Reference Material (CRM; Batches 206 & 214) provided by the Scripps Institute of Oceanography, was ± 2.8 µmol kg^{-1} for DIC, ± 1.1 µmol kg^{-1} for TA. Dickson et al. (2007)'s methodology was developed for typical ocean DIC (1800 - 2300 µmol kg^{-1}) and TA (2000 – 2500 µmol kg^{-1}) concentrations. However, the DIC and TA concentrations of some of our collected samples were well below this range. By lowering the VINDTA's initial and incremental acid additions it was possible to perform TA measurements below the VINDTA's intended range, however, if the buffering capacity of the sample was too low, even the lowest possible initial acid injection resulted in an over-titrated sample. Thus, we were unable to confidently determine TA ≤ 600 µmol kg^{-1}. With respect to DIC analysis, the same issue did not occur due to the incorporation of a coulometer; a hydroxide ion generator that maintains a specific transmittance value (Dickson et al., 2007).

Sample pH was determined in the field using Dickson et al. (2007)'s protocols for the determination of the pH of sea water using: 1) a glass/reference electrode cell (2022; SOP 6a) and 2) the indicator dye *m*-cresol purple (2023; SOP 6b). In 2022, pH was determined on the free scale using an Orion Star A121 Portable pH Meter (accuracy ± 0.01) calibrated once per day using a three-point calibration at ambient temperature (16°C ± 2°C). Sample pH measurements were made following instrument calibration, allowing the electrode sufficient time to equilibrate (7 min ± 6 min) within each sample before moving onto the next. Since this combination electrode was intended for freshwater pH measurements, it reports pH on the

freshwater scale. As such, sample pH measurements from 2022 were adjusted to the total scale using R package seacarb (See 2.2.3). In 2023, pH was determined using a spectrophotometer (Thermo Scientific Multiskan Spectrum, 1 nm resolution, ± 1 nm). Following Douglas & Byrne (2017) and Mosley et al. (2004), spectrophotometric pH was measured using the indicator m-cresol purple. A small volume of unpurified dye (40 µL) was added to seawater samples in a 1 cm pathlength quartz cuvette, and absorbance was recorded at the indicator wavelengths (434 and 578 nm) and a non-absorbing reference wavelength (730 nm). This process was repeated with a second addition of dye before absorbance ratios were corrected for background absorbance and dye perturbation. Finally, pH on the total scale was calculated using temperature- and salinity-dependent molar absorptivity ratios.

To assess the accuracy of the different pH determination methods, linear regression models were applied using calculated pH as the dependant variable and measured pH as the independent variable (summarized in Table 2). A linear regression developed using all pH measurements was strongly influenced by outlying data points made in the Churchill, Moose, and Eastmain River estuaries. To remedy this, all (4) points with a difference in pH greater than 0.25 were removed from the regression models. The resulting linear regression models are summarized within Table 1.

Table 4.1: Summary of linear regression models used to validate in-situ pH measurements. RMSE: root mean square error.

	slope	Slope s.d.	n	r	rmse
2021	n.d.				
2022 and 2023	0.28	±0.72	203	0.36	0.071
2022 and 2023 (no outliers)	0.46	±1.33	199	0.47	0.047
2022 (no outliers)	0.33	±1.77	111	0.29	0.058
2023 (no outliers)	0.79	±2.24	88	0.90	0.018

Linear regression models developed to compare measured pH with calculated pH provide insight into which pH method is the most accurate while simultaneously validating our pH calculations based on TA and DIC (Section 2.2.1). Both methods of pH determination, spectrophotometer and combination electrode, accurately reflect the pH as determined through seacarb with a RMSE of 0.05 pH units (Supplementary Figure C.1, Table 4.2). Linear regression models for these years independently can be used to assess the performance of the instruments relative to one another (Supplementary Figure C.7). The fit of the linear regression model using the combination electrode (2022; r = 0.29) is significantly poorer than that of the

spectrophotometer (2023; r = 0.90). Further, the spectrophotometer model's accuracy (rmse = 0.02) is better than the combination electrode model's accuracy (rmse = 0.06).

While both pH determination methods provide accurate representations of the total activity of hydrogen ions within the sample, the spectrophotometer performed consistently better. High degrees of accuracy and precision are required for accurate carbonate system calculations; thus, the spectrophotometer is the recommended method for shipboard pH determination in an estuarian environment as it was able to produce pH values close to those calculated using DIC and TA. In addition to being more accurate than the combination electrode, pH measurements provided by the spectrophotometer are accurate to 3 decimal places, whereas pH readings provided by the combination electrode are only accurate to 2 decimal places. Due to the lack of data in 2021 and the poor performance of the portable pH Meter in relation to the calculated pH values in 2022, only the 2023 pH measurements made using the spectrophotometer were examined.

4.3.3 Data Analysis

All data analyses were done using R (v 4.5.2), RStudio (v 2026.01.0+392), and Ocean Data View (ODV; v 5.8.1; Schlitzer, 2023). The difference between oxygen saturation concentration and observed dissolved oxygen, apparent oxygen utilization (AOU), was calculated in ODV from CTD-derived temperature, salinity, and dissolved oxygen measurements. Carbonate system calculations were performed using R package 'seacarb' (v 3.3.3; Gattuso et al. 2024). Definitions of the first and second dissociations constants of carbonic acid (K_1 and K_2) were selected to reflect the temperature and salinity ranges of our bottle samples (Millero, 2010; supplementary table C.1). While K1 and K2 definitions determined by Lueker et al. (2000) are recommended by Dickson et al., 2007, the K1 and K2 definitions determined by Millero (2010) perform similarly (Millero, 2010) and were developed specifically for estuary carbonate system calculations so they are best suited for our lower salinity data set. The R package "Tidyverse" was used to assist in data formatting and plot creation (Wickham et al., 2019).

Saturation state is calculated as a product of the concentration of calcium (Ca^{2+}) and carbonate (CO_3^{2-}) ions in solution divided by KSP, the equilibrium solubility product for a given carbonate mineral (aragonite or calcite) was determined as (Zeebe & Wolf-Gladrow, 2001):

Eq. 4.1 $$\Omega = \frac{[Ca^{2+}][CO_3^{2-}]}{K_{sp}^*}$$

K_{SP} may be estimated as a product of the saturation concentrations of Ca^{2+} and CO_3^{2-} for a given temperature, pressure, and salinity (AMAP, 2018):

Eq. 4.2 $$K_{SP} = [Ca^{2+}]_{sat}[CO_3^{2-}]_{sat}$$

Therefore, when $[Ca^{2+}]$ and $[CO_3^{2-}]$ are at their saturation concentrations (i.e. $[Ca^{2+}][CO_3^{2-}] = [Ca^{2+}]_{sat}[CO_3^{2-}]_{sat}$), Ω = 1. When seawater Ω is greater than one (Ω > 1), water is said to be 'saturated' with respect to $CaCO_3$. When seawater is 'undersaturated' with respect to $CaCO_3$ (Ω < 1), calcifers may struggle to form their hard structures. Measurement uncertainty propagated through the carbonate system calculations indicated a mean uncertainty of 0.04 ± 0.01 for aragonite and 0.08 ± 0.02 for calcite.

Water mass fractions were estimated using three linear equations in tandem with three end-members: seawater (SW), meteoric water (MW), and sea ice melt (SIM) as described by Ostlund & Hut (1984):

Eq. 4.3 $$f_{SW} + f_{MW} + f_{SIM} = 1$$

Eq. 4.4 $$f_{SW}S_{SW} + f_{MW}S_{MW} + f_{SIM}S_{SIM} = S_{Observed}$$

Eq. 4.5 $$f_{SW}\delta^{18}O_{sw} + f_{MW}\delta^{18}O_{MW} + f_{SIM}\delta^{18}O_{SIM} = \delta^{18}O_{Observed}$$

Where f denotes the fraction of the associated subscript, S is the salinity, and $\delta^{18}O$ is the stable isotope composition of the sample. Sea ice melt and seawater end-members used here were published in Ahmed et al., (2020), whereas the meteoric water end-member was altered to better reflect conditions observed in the Moose River estuary (Table 4.2). A Monte Carlo simulation was used to determine the sensitivity of the calculated water mass fraction to the uncertainty of the end-member values (Table 4.2) following Burgers et al., 2024. Coefficient of variation (CV = standard deviation/mean) may be used to estimate the relative uncertainty in any particular calculation (Burgers et al., 2024).

Table 4.2: Summary of water mass end-members. Seawater and sea ice melt end-members are from Ahmed et al., 2020). Meteoric water end-member determined from samples in the Moose River estuary.

	Salinity	$\delta^{18}O$ (‰)
Seawater (SW)	32.1 ±0.1	-2.5 ±0.2
Sea Ice Melt (SIM)	1.4 ±0.5	-0.8 ±0.2
Meteoric Water (MW)	0	-12.3 ±0.3

4.4 Results

4.4.1 Water Mass Fractions

The surface mixed layer extended on average 9.1 ± 6m, 7.5 ± 5m, and 7.1 ± 4m in 2021, 2022, and 2023, respectively (Bouchard et al., in prog.). Freshwater contributions increased towards the coasts, with high f_{SW} >0.90 surrounding the Belcher Islands and in Hudson Bay open waters, decreasing to f_{MW} greater than 0.50 in local estuaries, specifically the Churchill River, Winisk River, Moose River, and the Eastmain River (Figure 4.2). The high uncertainty associated with SIM end member (Table 4.2) reduces certainty in determining f_{SIM}, however, MW and SW end members are better defined (Table 4.2). Calculated CV, an estimate the relative uncertainty, indicates that f_{MW} estimations have lowest uncertainty within James Bay, where river inputs are high, however the CV increases northwards of the Belcher Islands (Supplementary Figure C.3). The CV of f_{SW} displays a slight inverse relationship with the CV of f_{MW}; the CV of f_{SW} increases with proximity the Winisk, Moose, and Eastmain Rivers. As the uncertainty of the f_{SIM} measurements was high, they were not used for further analysis.

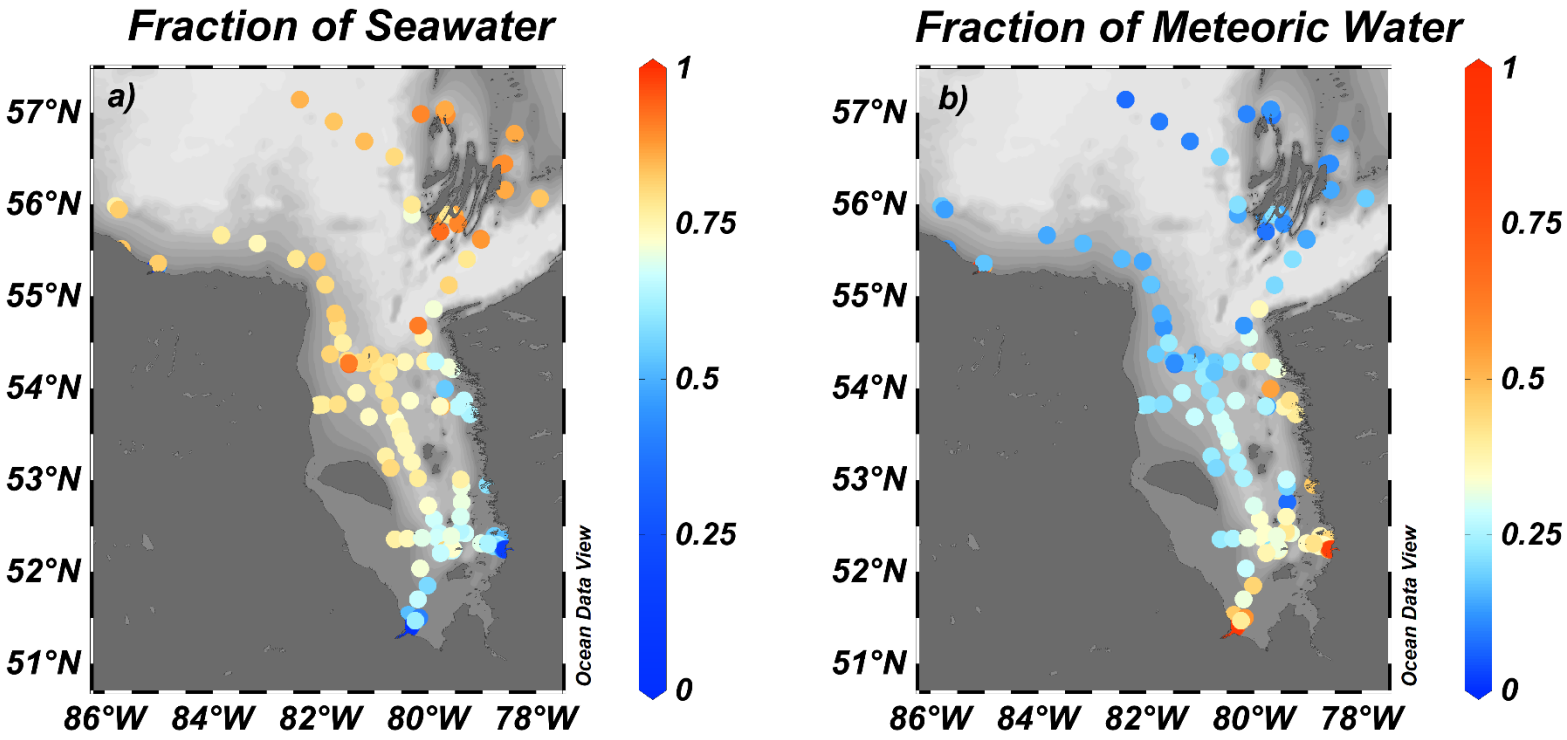

Figure 4.2: (a) Fraction of seawater within surface water samples, (b) fraction of meteoric water within surface water samples.

Generally speaking, the meteoric fractions of surface water in James Bay were higher than in southern Hudson Bay (Figure 4.2). Surface waters sampled within the shallow river deltas of James Bay were largely meteoric in origin and the fraction of meteoric water nears

100% within the Moose River estuary (Figure 4.3). Within the shallow deltas of the Eastmain, La Grande, and Moose Rivers, meteoric water concentration decreased rapidly moving from the coast into the bay along the cruise track (Figure 4.2). For example, moving northwards along the section in Figure 4.3, the fraction of meteoric water in the surface 35m decreases from 100% in the Moose River estuary, to about 30% at the centre of James Bay. Meteoric water concentration continues decreasing northwards to ~10% at the mouth of James Bay.

The presence of an underwater sill (~35m) south of 54°N (Figure 4.3), limits mixing at depth. South of the sill, the fraction of meteoric water deeper than the sill (below 35m) decreases from 30% to 20%. North of the sill, meteoric water fractions decrease to 15 – 10%, indicating that the sill serves to limit deeper water exchanges, retaining more freshwater in the southern end of James Bay, at least in summer. North of James Bay, meteoric water content of samples collected from the top 20m remained ~20%, before decreasing to ~13% in the Belcher Islands (Figure 4.2).

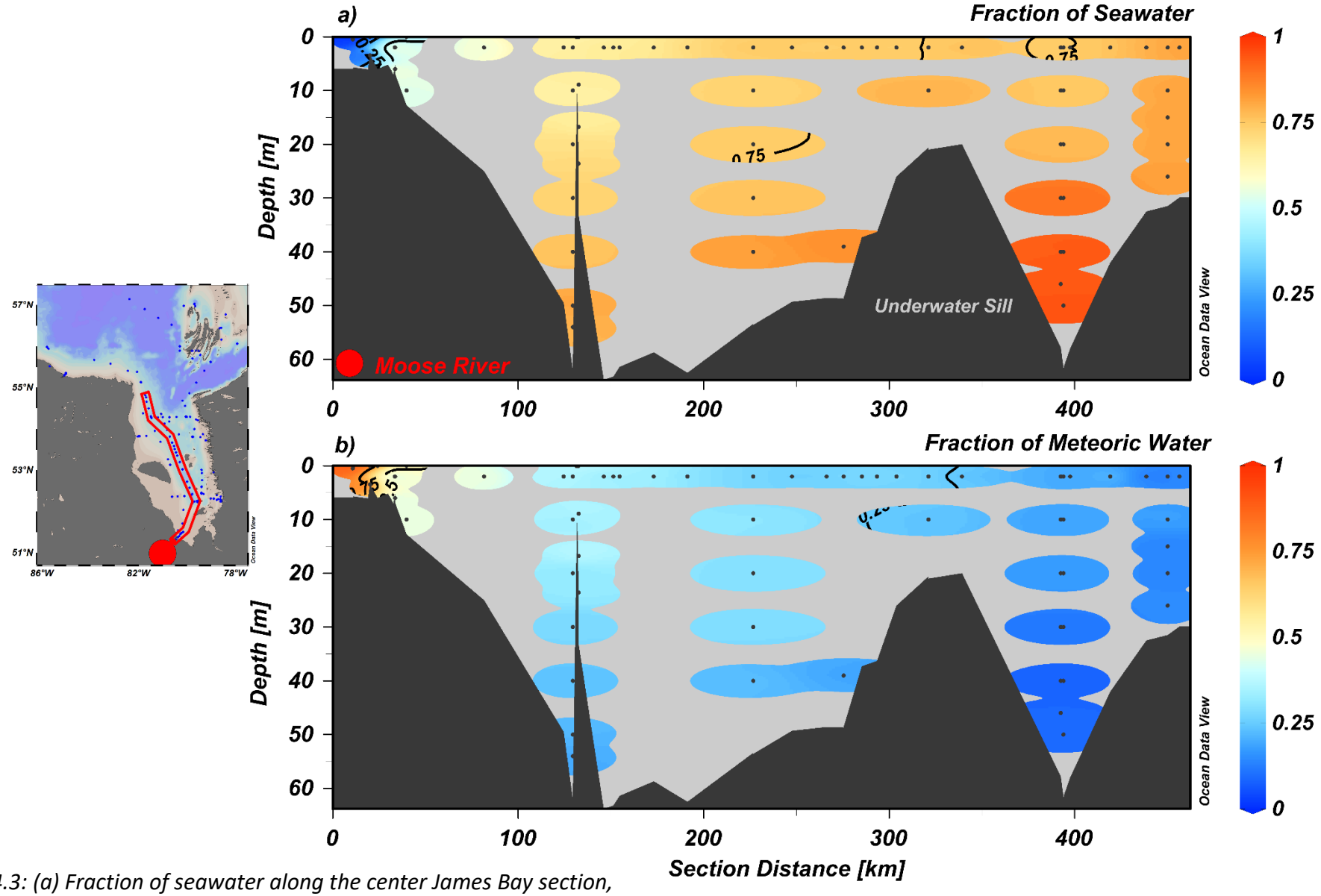

Figure 4.3: (a) Fraction of seawater along the center James Bay section, (b) fraction of meteoric water along the center James Bay section.

4.4.2 Total Alkalinity and Dissolved Inorganic Carbon

Measured TA ranged from 615 to 2263 µmol kg^{-1}, increasing with depth and with seawater fraction (f_{SW}). The lowest measurements of TA were made within the Eastmain River, while the most alkaline samples were collected from deep water (>60m) near the mouth of the Winisk River and surrounding the Belcher Islands (Figure 4.4). Measured DIC ranged from 762 to 2228 µmol kg^{-1} and followed a similar distribution to TA (i.e., increasing with f_{SW} and depth). The freshwater end-members of DIC and TA within the Moose River were substantially different from those within the Eastmain River (Supplementary Figure 4.4). Measurements of DIC and TA made at S = 0.09 in the Moose River correspond with DIC = 1218.0 and TA = 1280.7 µmol kg^{-1}, whereas in the Eastmain River, low salinity measurements (S = 4.73) were associated with DIC = 762.1 and TA = 614.8 µmol kg^{-1}. Samples collected at S = 0 in the Eastmain River had a TA value below the detection limit of our analytical methods (see methods). Across the study region, the ratio of TA:DIC was consistently >1, except for samples taken from a transect near the Eastmain River where DIC exceeded TA by 100 to 150 µmol kg^{-1} (TA:DIC = 1.09).

The distribution of carbonate system variables (DIC and TA) within James Bay follows that of meteoric water fraction (Figures 4.2 and 4.4), and correspondingly both DIC and TA in surface waters were generally lower in James Bay relative to southern Hudson Bay. Specifically, DIC and TA concentrations are lowest within the Eastmain and La Grande River estuaries, coinciding with meteoric water fractions of 50% or more. The presence of an underwater sill near 54°N in James Bay impacts observed DIC and TA concentrations at depth. South of the sill, where meteoric water (~20%) persists at depth, DIC and TA increase by ~200 µmol kg^{-1} with depth, while north of the sill, the influence of seawater is greater and DIC and TA increase by ~400 µmol kg^{-1} with depth.

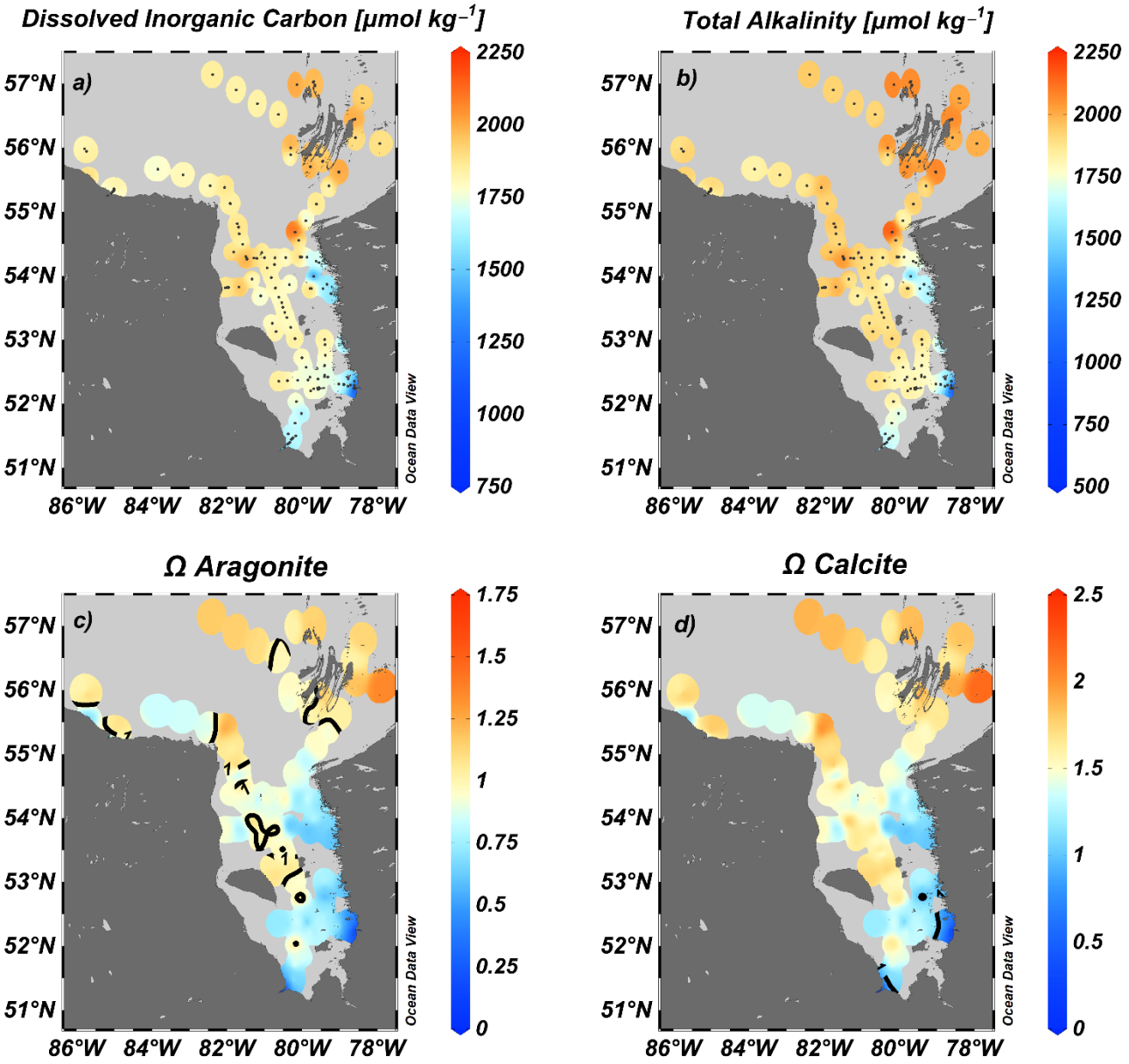

Figure 4.4: (a) Surface water dissolved inorganic carbon concentration, (b) Surface water total alkalinity, (c) Surface water saturation state of aragonite, (d) Surface water saturation state of calcite

4.4.3 pH

Calculated pH ranged from 6.7 to 9.0 with a mean pH of 7.9 (±0.2). The most acidic water samples (pH 6.7 – 7.2) were collected from the Eastmain River estuary, whereas the most basic water samples (pH 8.7 – 9.0) were collected from the Winisk and Moose River estuaries. Calculated pH was nearly constant within vertical depth profiles (7.9 ± 0.1; Figures 4.5 and 4.6).

4.4.4 Saturation State of Carbonate Minerals

The saturation state of aragonite (Ω_{Arag}) and calcite (Ω_{Cal}) in surface waters (Figure 4.4c and 4.4d) generally followed the distribution of meteoric water highlighted in Figure 4.2. As such, both saturation states were generally higher in southern Hudson Bay relative to James Bay. The saturation state of aragonite (Ω_{Arag}) ranged from 0.1 to 1.5, with a mean of 0.9 ± 0.3. Like pH, the lowest observations of Ω_{Arag} were found in the Eastmain River estuary; however, unlike pH, the Ω_{Arag} observations from rivers draining the HBL were similar to those from the Eastern rivers (Figure 4.6). The saturation state of aragonite was observed to be the highest in two places: 1) in surface water surrounding the Belcher Islands, and 2) in surface water near the Winisk estuary (Figure 4.4). A clear saturation horizon (i.e., depth where $\Omega_{Arag} = 1$) does not exist within James Bay, as the entire water column was observed to be undersaturated with respect to aragonite during the time of sampling. The saturation state of calcite (Ω_{Cal}) followed a similar distribution Ω_{Arag}, however Ω_{Cal} was notably higher (Figure 4.4). The pattern of undersaturation ($\Omega_{Cal} < 1$) near the river mouths of James Bay was also evident (Figures 4.5 and 4.6), however the gradient over which Ω approaches 1 is steeper for Ω_{Cal}. As such, Ω_{Cal} approaches 1 within river mouths resulting in much of James Bay being saturated with respect to Ω_{Cal}.

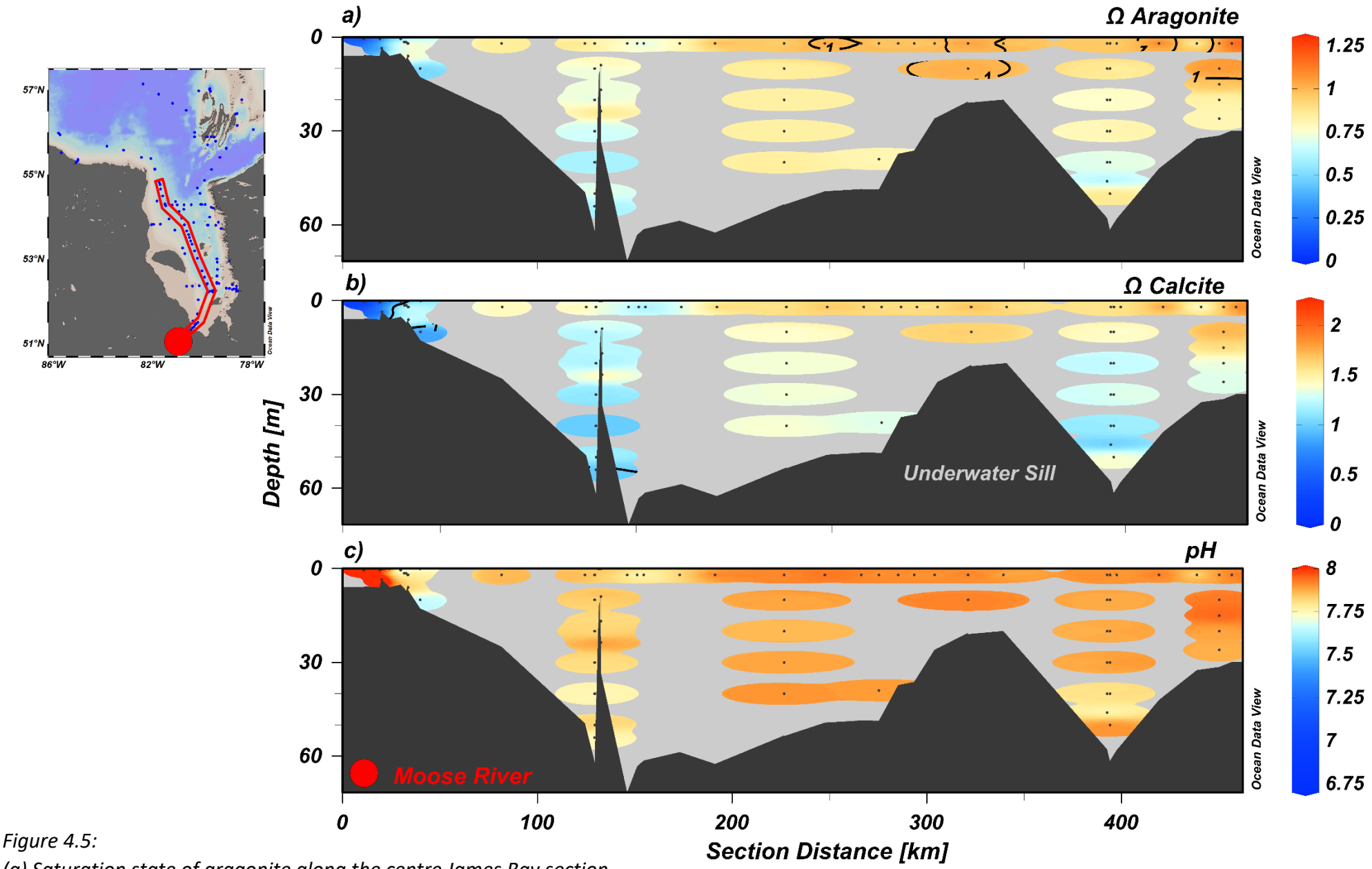

Figure 4.5:
(a) Saturation state of aragonite along the centre James Bay section,
(b) Saturation state of calcite along the centre James Bay section,
(c) pH (calculated using DIC and TA in seacarb) along the centre James Bay section

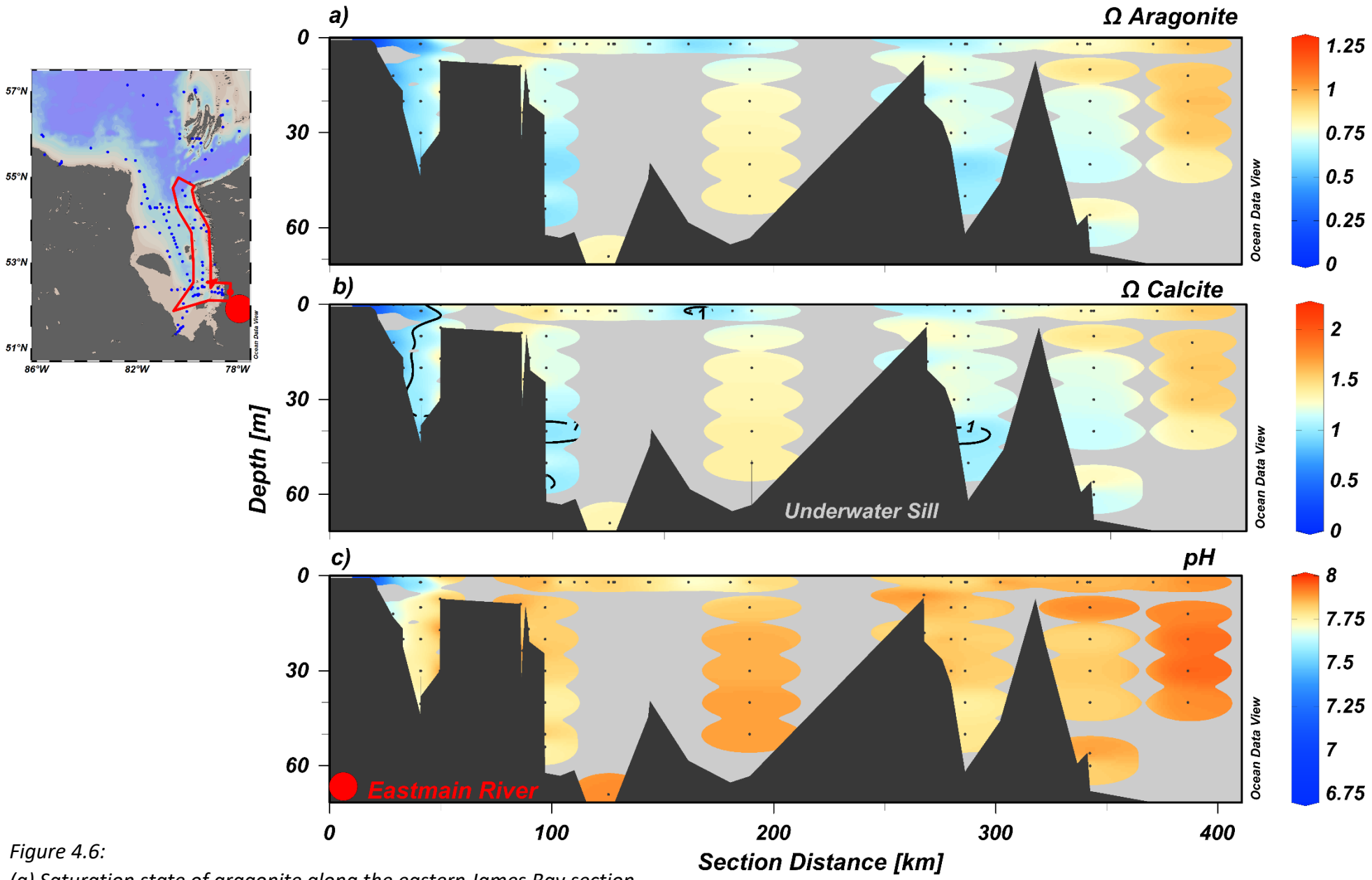

Figure 4.6:
(a) Saturation state of aragonite along the eastern James Bay section,
(b) Saturation state of calcite along the eastern James Bay section,
(c) pH (calculated using DIC and TA in seacarb) along the eastern James Bay section

4.5 Discussion

4.5.1 River water source drives marine aragonite saturation state in shallow James Bay estuaries

Within James Bay, the influence of meteoric water on the carbonate system varies by longitude, as rivers entering eastern James Bay dilute DIC and TA more strongly than the rivers entering western James Bay. As previously discussed, the minimum TA and DIC were found near the Eastmain River estuary, while TA and DIC observed in the Moose River estuary were substantially higher (Figure 4.4). Previous work within Hudson Bay identified two freshwater TA end-members: a high end-member (1870 µmol kg^{-1}, Burt et al., 2016) and a low end-member (754 µmol kg^{-1}, Azetsu-Scott et al., 2014). The higher TA end-member from Burt et al., (2016) was attributed to features of the Nelson River drainage basin; a combination of alkaline glacial deposits, alkaline bedrock, and increased weathering of organic rich soils relative to most tundra rivers (Azetsu-Scott et al., 2014; Burt et al., 2016; Mundy et al., 2010; Tank et al., 2012). The lower TA river end-member was attributed to the igneous bedrock of eastern Hudson Bay, where calcium ions are less abundant, lowering the buffering capacity of the rivers (Azetsu-Scott et al., 2014). Within James Bay, the high alkalinity end-member (1670 µmol kg^{-1}) is near to that of Burt et al. (2016) for Hudson Bay, likely due to the Moose river sharing many alkaline characteristics with the Nelson River. Glacial retreat has left high concentrations of glaciolacustrine sediment on in the watersheds of the Moose and Nelson Rivers, allowing for fast paced erosion due to climate warming (Kuzyk & Candlish, 2019).

In previous studies in Hudson Bay, zero salinity (river water) TA end-members were determined through linear regression, however the range of salinity over which the relationship was constructed was limited to salinities greater than 20 (Azetsu-Scott et al., 2014; Burt et al., 2016; Yamamoto-Kawai et al., 2005). In this study, a linear regression was applied to our Eastmain estuary samples yielding a freshwater TA end-member of 238.8 ±1.0 µmol kg^{-1} (Supplementary Figure C.5). Our “low” alkalinity end-member is lower than previous estimates for Hudson Bay (689, 710 µmol kg^{-1}, Burt et al., 2016; 754 µmol kg^{-1}, Azetsu-Scott et al. 2014) and five of the Arctic’s six largest rivers (Cooper et al., 2008). The low TA river water end-member observed within this study is similar to that of the Kolyma River (518 ±21 µmol kg^{-1}; Cooper et al., 2008). The Kolyma River was found to be enriched in rare earth elements associated with the weathering of acid crystalline magmatic and metamorphic rocks; a unique feature among rivers of the region (Gordeev et al., 2024). Thus, the low TA observed within the Kolyma River was attributed in part to basin lithology (Gordeev et al., 2024). Similarly, rare earth element concentrations within the Eastmain River coincide with metamorphic bedrock from the superior province of the Canadian Shield (Lafrenière et al., 2025), contributing to its low TA values.

The TA from rivers draining into James Bay impact seawater carbonate system to different degrees. To illustrate this effect, consider two individual systems where the TA end-members are mixing with seawater. If the mixture is one part seawater (TA = 2262.7 µmol kg^{-1}, S = 32) and one equal part meteoric water from Eastmain River (238.8 µmol kg^{-1}, S = 0), the resulting final composition would be S = 16 and TA = 1251 µmol kg^{-1}. For a second mixture, using river water from the Moose River (TA = 1670 µmol kg^{-1}, S = 0) a 1:1 final composition of S = 16 and TA = 1966 µmol kg^{-1} would result. Thus, the dilution of TA caused by eastern James Bay rivers is greater than that of the western rivers. Assuming similar conservative mixing of DIC, mixing of seawater (DIC = 2227.8 µmol kg^{-1}) with meteoric water from the Eastmain River (441 µmol kg^{-1}, determined through linear regression) yields a DIC value of 1334 µmol kg^{-1}, while mixing with meteoric water from the Moose River (1661.4 µmol kg^{-1}) yields a DIC value of 1945 µmol kg^{-1}. As such, these river-ocean mixtures have differing impacts on the buffering (CO_2 uptake) capacity of the surface ocean, where surface waters interacting with the Moose River exhibit greater capacity to buffer against CO_2 uptake, relative to the waters interacting wit the Eastmain River.

Patterns observed in surface meteoric water fractions and seawater TA are evident in the saturation states of both aragonite and calcite. Saturation states were lower in eastern James Bay in waters that receive low TA river inflow from boreal soils underlain by Precambrian shield. The response of $\Omega_{Aragonite}$ to river water mixing with seawater was assessed using the previously established mixtures (Moose River/Seawater; Eastmain River/Seawater) in Seacarb, assuming a water temperature of 7.5°C (mean observed water temperature). The seawater $\Omega_{Aragonite}$ decreased from 0.78 to 0.11 in the Eastmain mixture, and from 0.78 to 0.66 in the Moose River mixture. Using the previously described riverine & marine end-members for DIC, TA, and salinity, schematic mixing lines were drawn (Figure 4.7) to illustrate the differing impacts of the freshwater on $\Omega_{Aragonite}$ across a range of sea to freshwater ratios. Despite mixing with the same seawater, the two seawater mixtures (Moose and Eastmain) result in quite different $\Omega_{Aragonite}$ values, with the Mooser River mixture potentially resulting in weaker dilution of $\Omega_{Aragonite}$. The results suggest that eastern James Bay is more vulnerable to acidification in response to increased freshwater input, while western James Bay exhibits a degree of resilience towards acidification given the higher alkalinity of river inflow. Given the combination of the relatively small volume of James Bay, and large river inflow relative to Hudson Bay, James Bay appears more vulnerable to acidification relative to Hudson Bay.

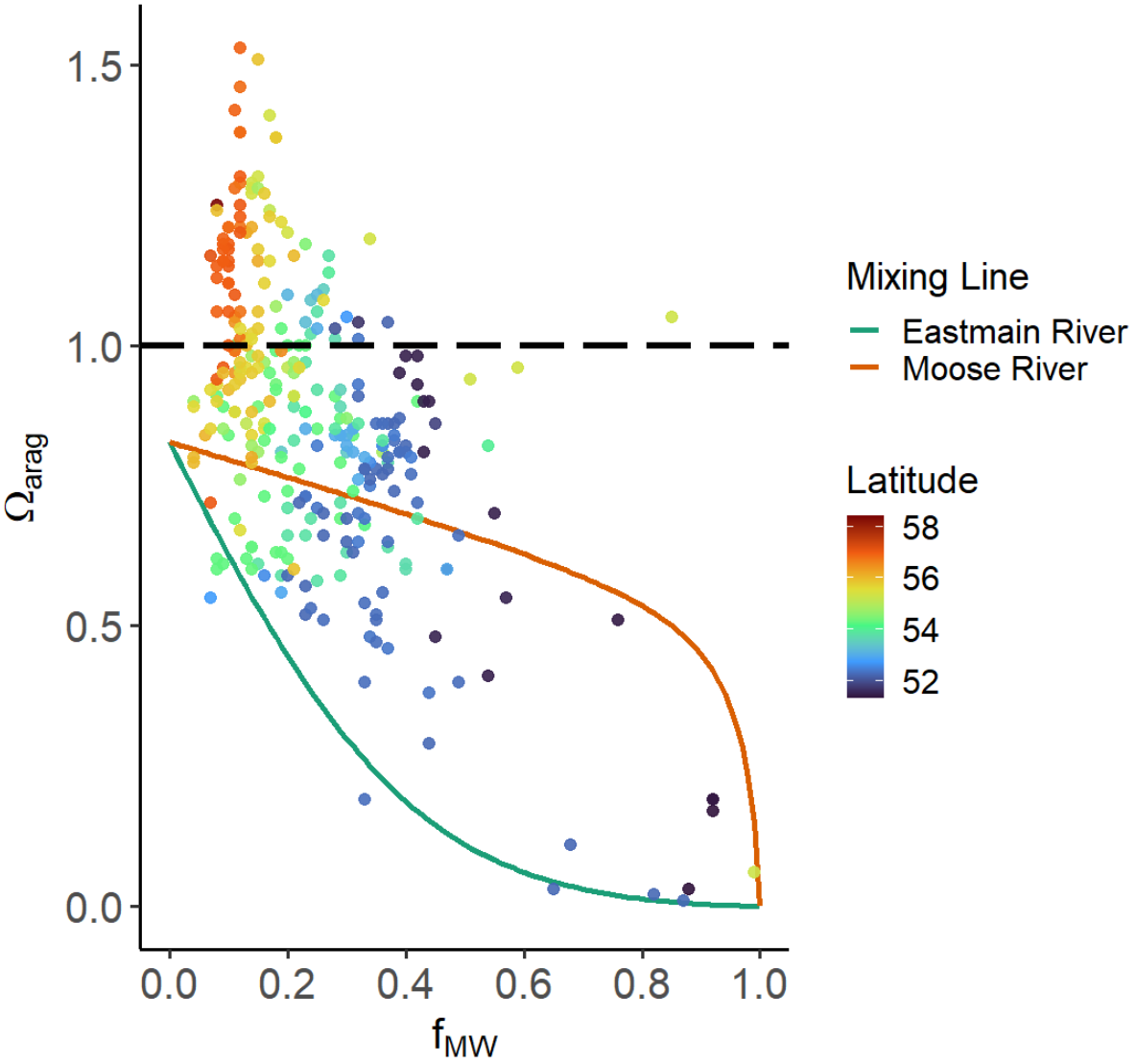

Figure 4.7: Fraction of meteoric water vs saturation state of aragonite. Schematic mixing lines are drawn for the Moose (Orange) and Eastmain (Green) Rivers. A two-endmember mixing model was constructed by conservatively mixing TA and DIC between the fresh and seawater end-members at 1% increments, from 0 to 100%. Aragonite saturation state was then calculated for each mixture using seacarb.

The thermal influence of these rivers interacting with the ocean should also be considered. Saturation state is affected by temperature because pH is dependant on temperature, but DIC and TA are conservative quantities; their absolute concentrations do not vary with temperature. Thus, freshwater delivery from rivers has an indirect impact on saturation state as well; warm water increases the amount of carbonate minerals that may be dissolved in solution, thus the amount of carbonate minerals capable of being dissolved in seawater may increase through temperature change alone. Our data indicate that Ω patterns are primarily governed by freshwater dilution within James Bay, however, the thermodynamic control on saturation state remains unclear and potentially significant.

4.5.2 Aragonite undersaturation persists throughout the water column in James Bay

In deeper waters away from the coastline, local bathymetry impacts the saturation state of aragonite ($\Omega_{Aragonite}$). Deep water south of the sill (located near 54°N) had a higher $\Omega_{Aragonite}$ (~0.8) compared to deep waters north of the sill (~0.6; Figures 4.5 and 4.6). Where aragonite saturation state decreases in deep water, both apparent oxygen utilization (AOU) and the ratio of TA:DIC increases (Supplementary Figure C.6), providing evidence of processes that increase DIC over TA (respiration, remineralization, etc.). Notably, there was no well-defined aragonite saturation horizon within James Bay. The surface water (0 – 10m) at the centre of James Bay was intermittently saturated with aragonite, with observations of saturation extending as far south as 52°N. Surface waters were observed to be saturated in $\Omega_{Aragonite}$ once exiting James Bay, near 55°N. North of James Bay, in the Belcher Island shelf sea, $\Omega_{Aragonite}$ remained undersaturated in bottom water, with a saturation horizon ~20 – 40m deep. Deep waters in James Bay are undersaturated with respect to aragonite, similar to the remineralized deep waters from Hudson Bay, which carry elevated DIC and TA relative to surface water (Azetsu-Scott et al., 2014). Under James Bay's circulation (Ridenour et al., 2019), these denser, saline waters flow into the deeper portions of James Bay, contributing to persistent $\Omega_{Aragonite}$ undersaturation in bottom waters (Figure 4.5 and 4.6; Azetsu-Scott et al., 2014; Burt et al., 2016).

4.5.3 James Bay as a sub-Arctic estuary

Arctic and sub-Arctic coastal regions influenced by large quantities of river discharge (e.g. Beaufort and Bering Seas) have been identified as areas where carbonate chemistry is particularly sensitive to freshwater forcing and atmospheric CO_2 uptake (Mathis et al., 2015; Qi et al., 2017). Along the coasts, where terrestrial influence is maximized, sub-Arctic seas such as the Baltic Sea have been observed to be sensitive to terrestrial weathering, which increases TA concentration (carbonate dominated catchments), and serves to offset atmospheric CO_2 driven acidification (Müller et al., 2016). These terrestrial inputs contribute to increasing both Ω and the overall CO_2 storage capacity (Müller et al., 2016).

The summer cruises in James Bay showed warmer water and lower salinity, TA, pH, and calcium carbonate saturation states than southern Hudson Bay based both on data reported here, and the greater Hudson Bay complex (including Fox Basin and Hudson Strait; Azetsu-Scott et al., 2014; Burt et al., 2016). Both Hudson Bay and James Bay are mediterranean seas, with the carbonate system in James Bay consistent with a water body more strongly influenced by river water inflow. Others have reported that sub-Arctic seas are predisposed to lower pH and a saturation state closer to one due to cold temperatures, enhanced solubility of CO_2, and increased freshwater inputs (Orr et al., 2005; Steinacher et al., 2009).

Similar conditions have been documented within Hudson Bay estuaries, where large riverine discharge and limited exchange with the open ocean result in naturally low saturation

state with links to local watershed geology (Azetsu-Scott et al., 2014; Burt et al., 2016). James Bay has been described as a strongly-stratified, mixed estuary in summer (Prinsenberg, 1978) which is characterized by stronger terrestrial influence and longer residence times (6.6 yr Hudson Bay; 10.2 months James Bay; Prinsenberg, 1984) than the Arctic Ocean (4.3 yr; Ekwurzel et al., 2001), which amplifies the effects of freshwater mixing and biogeochemical processing on carbonate chemistry (Burt et al., 2016; Carmack et al., 2016).

4.5.3.1 Influence of upstream Hudson Bay conditions

James Bay does not operate as an isolated estuary but rather as a southern extension of the Hudson Bay marine system, which is also estuary-like in character. Changes occurring upstream in Hudson Bay, therefore, dictate carbonate chemistry within James Bay, while changes in James Bay, in turn, alter the carbonate chemistry of Hudson Bay. Observations from this study indicate that deep waters north of the James Bay sill exhibit lower $\Omega_{Aragonite}$ and stronger evidence of remineralization-driven DIC accumulation, consistent with carbonate system processes documented in the Hudson Bay system (Azetsu-Scott et al., 2014; Burt et al., 2016). If Hudson Bay continues to experience increased stratification, reduced sea ice cover, enhanced respiration, and shallowing of the saturation horizon in subsurface waters, the inflowing marine end-member to James Bay will become progressively enriched in CO_2 and lower in saturation state (Soriot et al., 2025; Steiner et al., 2015; Terhaar et al., 2021). Lower saturation state source waters may compound the effects of freshwater dilution within James Bay, driving widespread undersaturation of $\Omega_{Calcite}$ throughout the water column. Thus, future carbonate chemistry within James Bay will reflect the combined influence of James Bay's local estuarine processes and basin wide changes in Hudson Bay.

4.5.4 Potential impacts of continued climate change to the inorganic carbon system of James Bay

Continued climate change is projected to impact both the physical and biogeochemical processes that control the inorganic carbon system of James Bay. Regional assessments such as Canada's Changing Climate Report project continued warming across northern Canada at rates exceeding the global average (Arctic amplification), resulting in air and surface temperature increases, reduced sea ice cover, changes in hydrology, and decreases in permafrost extent throughout the 21st century (Bush & Lemmen, 2019). Within the Hudson Bay and James Bay region, Arctic amplification manifests as deeper seasonal permafrost thaw, reduced snow and ice cover, and shifts in the timing and magnitude of freshwater discharge from watersheds flowing into Hudson and James Bay (Constable et al., 2022; Derksen et al., 2019). Additionally, warming, permafrost degradation, and increased frequency of forest fires serve to mobilize reservoirs of terrestrial organic carbon, increasing the delivery of organic matter to rivers, and ultimately the ocean (Schuur et al., 2015). Under these projected changes, James Bay may experience acidification, whereby the inorganic carbon system is pushed towards more acidic

conditions (AMAP, 2018; Steiner et al., 2015; Terhaar et al., 2021). Warmer waters and increased freshwater inflow to James Bay are expected to increase the uptake of atmospheric CO_2, lowering pH and reducing Ω, particularly in nearshore environments (Ahmed et al., 2020; Azetsu-Scott et al., 2014). Enhanced delivery of terrestrial organic matter may further increase microbial respiration and CO_2 production within coastal waters, contributing to a further decrease Ω due to remineralization (Bauer et al., 2013; Capelle et al., 2020; Vonk et al., 2025). This combination of drivers may serve to expand regions of $\Omega < 1$, increasing the risk of corrosive conditions for calcifying organisms, with other possible poorly understood ecosystem impacts.

Generally, when Ω is less than 1, the energetic cost of calcification increases, which can impair shell formation, particularly for organisms that require aragonite (Doney et al., 2009; Fabry et al., 2008). Aragonite is more soluble than calcite, leading undersaturation with respect to aragonite to occur at higher carbonate ion concentrations. As a result, the energetic cost of precipitating $CaCO_3$ is generally greater under aragonite undersaturation, making $\Omega_{Aragonite}$ a more sensitive indicator of biological stress than $\Omega_{Calcite}$ (AMAP, 2018). Studies of Arctic and sub-Arctic calcifying organisms (e.g. pteropods, bivalves, or benthic invertebrates) have shown that they are especially sensitive to prolonged exposure to $\Omega < 1$ conditions, affecting their shell integrity, growth rates, and survival (Comeau et al., 2012; Fabry et al., 2009). Organisms within James Bay may exhibit a degree of tolerance to future acidification due to naturally low Ω conditions (Figures 4.5, 4.6, and 4.7), however, chronic exposure to waters with $\Omega < 1$ may still pose risks, particularly during early life stages when calcification demands are highest (Waldbusser et al., 2015; Waldbusser & Salisbury, 2014). Our observations suggest that the James Bay ecosystem may already be operating near biological thresholds for calcification stress, particularly for organisms that form aragonite shells.

To track these changes and better predict their trajectory as the Arctic continues to warm, sustained monitoring of key physical and chemical variables is essential. Long-term observations of pH, temperature, salinity, TA, DIC, and Ω would provide the foundation for detecting trends and determining the if James Bay is becoming increasingly acidic (decreasing pH) and corrosive to carbonate. River discharge, terrestrial organic carbon composition, and permafrost thaw (including active layer depth and soil carbon mobilization) monitoring would also help link upstream watershed processes to coastal carbonate system dynamics (e.g., Capelle et al. 2020; De Melo et al. 2022; Vonk et al. 2025). This study provides only a snapshot of the ocean conditions in James Bay over three summers, continued studies will need to incorporate tools such as autonomous sensors, expanded shipboard surveys, and available remote sensing data to improve spatial and temporal coverage (e.g., Ahmed et al. 2020; Burt et al. 2016; Nielsen et al. 2024). Furthermore, the incorporation of Indigenous and local knowledge is crucial to enhancing understanding of ecosystem responses and environmental

change in the region, particularly where observation records are sparse and rapidly changing conditions challenge conventional monitoring approaches. These observations will inform models that predict future states of the carbonate system and associated ecosystem impacts under different climate scenarios, improving projections of the impacts of climate change in James Bay while supporting the James Bay communities in preparing for, and adapting to, their changing land and ocean.

4.6 Conclusion

This study provides the first high-resolution characterization of the southern Hudson Bay and James Bay inorganic carbon system. We found widespread undersaturation of aragonite within James Bay, while calcite was undersaturated only in proximity to river mouths. Saturation state of carbonate minerals was dictated primarily by freshwater (river) input, however, the watershed from which the freshwater originated strongly impacted the state of the carbonate system. Rivers draining the Hudon Bay Lowlands in western James Bay had higher total alkalinity and more basic conditions (pH > 7), whereas rivers draining into eastern James Bay were more acidic (pH < 7), with considerably lower total alkalinity. The difference in river water properties can be attributed to the differing watershed geology along eastern and western James Bay. In western James Bay, the HBL are situated over carbonate bedrock (high TA), whereas in eastern James Bay rivers are more influenced by silicate bedrock (lower TA).

Carbonate chemistry in James Bay strongly reflects the interaction of freshwater forcing. The large inflow of river water relative to the basin size causes the surface water in James Bay to be warmer and exhibiting lower salinity, TA, pH, and saturation states relative to southern Hudson Bay. The James Bay surface waters in river-influenced regions exhibited reduced buffering capacity and carbonate mineral undersaturation, while deeper waters display evidence of remineralization-driven CO_2 accumulation associated with Hudson Bay deep water. River water influenced surface waters persist northward into parts of southern Hudson Bay and the Belcher Islands shelf region, indicating that processes occurring within James Bay influence carbonate chemistry in the downstream marine environment. The observed east–west asymmetry in river chemistry establishes a spatial sensitivity within James Bay surface water. Freshwater inputs from eastern watersheds produced stronger dilution of alkalinity and more pronounced reductions in saturation state, whereas western river input partially offset dilution through enhanced alkalinity supply. The eastern and western freshwater plumes mix, resulting in the water reaching the Belcher Island shelf being less corrosive than it would be if eastern rivers dominated the input in James Bay. Consequently, changes in freshwater discharge, river chemistry, and marine end-member composition will not affect James Bay uniformly but will instead amplify existing spatial gradients in carbonate chemistry and will go on to impact Southern Hudson Bay.

Projected climate-driven changes across the Hudson Bay watershed (altered runoff, enhanced stratification, or evolving upstream conditions in Hudson Bay) are expected to reinforce the mechanisms that presently drive low saturation state in James Bay. Increased freshwater delivery will strengthen surface water dilution and stratification, while changes in riverine carbon and alkalinity export may further reduce buffering capacity. Enhanced stratification in Hudson Bay will further reduce the saturation state of carbonate minerals of the marine source water flowing into James Bay in both surface and deep water. Under these

conditions, carbonate mineral undersaturation may become more spatially extensive, in both local ecosystems and waters exported to southern Hudson Bay. This work highlights the sensitivity of James Bay's carbonate system to future ocean acidification. Continued monitoring of James Bays carbonate system is essential not only to understand how estuarine processes interact to drive changes in saturation state, but to understand changes impactful to local fisheries and coastal communities that rely on marine resources.

4.7 References

Ahmed, M., Else, B. G. T., Capelle, D., Miller, L. A., & Papakyriakou, T. (2020). Underestimation of surface pCO_2 and air-sea CO_2 fluxes due to freshwater stratification in an Arctic shelf sea, Hudson Bay. *Elementa*, *8*(1). https://doi.org/10.1525/elementa.084

AMAP. (2018). *AMAP Assessment 2018: Arctic Ocean Acidification*.

Ausen, E. L., Redirchuk, G., Mundy, C. J., Ehn, J., & Kuzyk, Z. (2023). James Bay Expedition 2022-Cruise Report July 20–August 24, 2022. *Centre for Earth Observation Science (CEOS), University of Manitoba*, 73 pp. and Appendices A-G. https://doi.org/https://doi.org/10.34992/v3a3-f760

Azetsu-Scott, K., Starr, M., Mei, Z. P., & Granskog, M. (2014). Low calcium carbonate saturation state in an Arctic inland sea having large and varying fluvial inputs: The Hudson Bay system. *Journal of Geophysical Research: Oceans*, *119*(9), 6210–6220. https://doi.org/10.1002/2014JC009948

Azevedo, L. B., De Schryver, A. M., Hendriks, A. J., & Huijbregts, M. A. J. (2015). Calcifying species sensitivity distributions for ocean acidification. *Environmental Science and Technology*, *49*(3), 1495–1500. https://doi.org/10.1021/es505485m

Bauer, J. E., Cai, W. J., Raymond, P. A., Bianchi, T. S., Hopkinson, C. S., & Regnier, P. A. G. (2013). The changing carbon cycle of the coastal ocean. *Nature 2013 504:7478*, *504*(7478), 61–70. https://doi.org/10.1038/nature12857

Brand, U., Came, R. E., Affek, H., Azmy, K., Mooi, R., & Layton, K. (2014). Climate-forced change in Hudson Bay seawater composition and temperature, Arctic Canada. *Chemical Geology*, *388*, 78–86. https://doi.org/10.1016/j.chemgeo.2014.08.028

Bruneau, J. A., Ehn, J. K., Kuzyk, Z. Z. A., Crawford, A. D., & Leblanc, M. L. (2025). Step change in sea surface temperatures brings marine heat waves to sub-Arctic James Bay, Canada. *Frontiers in Marine Science*, *12*, 1549329. https://doi.org/10.3389/fmars.2025.1549329

Burgers, T. M., Azetsu-Scott, K., Myers, P. G., Else, B. G. T., Miller, L. A., Rysgaard, S., Chan, W., Tremblay, J., & Papakyriakou, T. (2024). Unraveling the Biogeochemical Drivers of Aragonite Saturation State in Baffin Bay: Insights From the West Greenland Continental Shelf. *Journal of Geophysical Research: Oceans*, *129*(8), e2024JC021122. https://doi.org/10.1029/2024JC021122

Burt, W. J., Thomas, H., Miller, L. A., Granskog, M. A., Papakyriakou, T. N., & Pengelly, L. (2016). Inorganic carbon cycling and biogeochemical processes in an Arctic inland sea (Hudson Bay). *Biogeosciences*, *13*(16), 4659–4671. https://doi.org/10.5194/bg-13-4659-2016

Bush, E., & Lemmen, D. S. (2019). *Canada's changing climate report*. https://doi.org/10.4095/314614

Capelle, D. W., Kuzyk, Z. Z. A., Papakyriakou, T., Guéguen, C., Miller, L. A., & Macdonald, R. W. (2020). Effect of terrestrial organic matter on ocean acidification and CO_2 flux in an Arctic

shelf sea. *Progress in Oceanography*, *185*. https://doi.org/10.1016/j.pocean.2020.102319

Carmack, E. C., Yamamoto-Kawai, M., Haine, T. W. N., Bacon, S., Bluhm, B. A., Lique, C., Melling, H., Polyakov, I. V., Straneo, F., Timmermans, M. L., & Williams, W. J. (2016). Freshwater and its role in the Arctic Marine System: Sources, disposition, storage, export, and physical and biogeochemical consequences in the Arctic and global oceans. *Journal of Geophysical Research: Biogeosciences*, *121*(3), 675–717. https://doi.org/10.1002/2015JG003140

Cooper, L. W., McClelland, J. W., Holmes, R. M., Raymond, P. A., Gibson, J. J., Guay, C. K., & Peterson, B. J. (2008). Flow-weighted values of runoff tracers (δ^{18} O, DOC, Ba, alkalinity) from the six largest Arctic rivers. *Geophysical Research Letters*, *35*(18), 2008GL035007. https://doi.org/10.1029/2008GL035007

de Groot, P. A. (Ed.). (2004). *Handbook of Stable Isotope Analytical Techniques* (Vol. 1). Elsevier.

De Melo, M. L., Gérardin, M.-L., Fink-Mercier, C., & Del Giorgio, P. A. (2022). Patterns in riverine carbon, nutrient and suspended solids export to the Eastern James Bay: Links to climate, hydrology and landscape. *Biogeochemistry*, *161*(3), 291–314. https://doi.org/10.1007/s10533-022-00983-z

Déry, S. J., Mlynowski, T. J., Hernández-Henríquez, M. A., & Straneo, F. (2011). Interannual variability and interdecadal trends in Hudson Bay streamflow. *Journal of Marine Systems*, *88*(3), 341–351. https://doi.org/10.1016/j.jmarsys.2010.12.002

Déry, S. J., Stadnyk, T. A., MacDonald, M. K., & Gauli-Sharma, B. (2016). Recent trends and variability in river discharge across northern Canada. *Hydrology and Earth System Sciences*, *20*(12), 4801–4818. https://doi.org/10.5194/hess-20-4801-2016

Dickson, A., Sabine, C., & Christian, J. (2007). *Guide to best practices for ocean CO_2 measurements*. North Pacific Marine Science Organization.

Douglas, N. K., & Byrne, R. H. (2017). Achieving accurate spectrophotometric pH measurements using unpurified meta-cresol purple. *Marine Chemistry*, *190*, 66–72. https://doi.org/10.1016/j.marchem.2017.02.004

Dredge, L. A., & Dyke, L. D. (2020). Landscapes and Landforms of the Hudson Bay Lowlands. In O. Slaymaker & N. Catto (Eds.), *Landscapes and Landforms of Eastern Canada* (pp. 211–227). Springer International Publishing. https://doi.org/10.1007/978-3-030-35137-3_8

Duarte, C. M., Hendriks, I. E., Moore, T. S., Olsen, Y. S., Steckbauer, A., Ramajo, L., Carstensen, J., Trotter, J. A., & McCulloch, M. (2013). Is Ocean Acidification an Open-Ocean Syndrome? Understanding Anthropogenic Impacts on Seawater pH. *Estuaries and Coasts*, *36*(2), 221–236. https://doi.org/10.1007/s12237-013-9594-3

Ekwurzel, B., Schlosser, P., Mortlock, R. A., Fairbanks, R. G., & Swift, J. H. (2001). River runoff, sea ice meltwater, and Pacific water distribution and mean residence times in the Arctic

Ocean. *Journal of Geophysical Research: Oceans*, *106*(C5), 9075–9092. https://doi.org/10.1029/1999JC000024

Gagnon, A., & Gough, W. (2006). Eastwest asymmetry in long-term trends of landfast ice thickness in the Hudson Bay region, Canada. *Climate Research*, *32*, 177–186. https://doi.org/10.3354/cr032177

Gattuso, J.-P., Epitalon, J.-M., Lavigne, H., & Orr, J. (2024). *seacarb: Seawater Carbonate Chemistry*. https://doi.org/10.32614/CRAN.package.seacarb

Gordeev, V. V., Pokrovsky, O. S., Zhulidov, A. V., Filippov, A. S., Gurtovaya, T. Y., Holmes, R. M., Kosmenko, L. S., McClelland, J. W., Peterson, B. J., & Tank, S. E. (2024). Dissolved Major and Trace Elements in the Largest Eurasian Arctic Rivers: Ob, Yenisey, Lena, and Kolyma. *Water*, *16*(2), 316. https://doi.org/10.3390/w16020316

Gulev, S. K., Peter W. Thorne, Jinho Ahn, Frank J. Dentener, Catia M. Domingues, Sebastian Gerland, Daoyi Gong, Darrell S. Kaufman, Hyacinth C. Nnamchi, Johannes Quaas, Juan A. River, Shubha Sathyendranath, Sharon L. Smith, Blair Trewin, Karina von Schuckmann, & Russell S. Vose. (2023). *Climate Change 2021 – The Physical Science Basis: Working Group I Contribution to the Sixth Assessment Report of the Intergovernmental Panel on Climate Change* (1st ed.). Cambridge University Press. https://doi.org/10.1017/9781009157896

Jiang, L.-Q., Carter, B. R., Feely, R. A., Lauvset, S. K., & Olsen, A. (2019). Surface ocean pH and buffer capacity: Past, present and future. *Scientific Reports*, *9*(1), 18624. https://doi.org/10.1038/s41598-019-55039-4

Kamula, M., Kuzyk, Z., & Mundy, C. J. (2022). *James Bay Expedition abord the William Kennedy—Cruise Report 1—17 August 2021*. Centre for Earth Observation Science (CEOS).

Kuzyk, Z., & Candlish, L. (2019). *From Science to Policy in the Greater Hudson Bay Marine Region: An Integrated Regional Impact Study (IRIS) of Climate Change and Modernization* (p. 424). ArcticNet.

Lafrenière, M.-C., Alam, M. S., Lapierre, J.-F., Ponton, D. E., Wauthy, M., Fink-Mercier, C., Marginson, H., Giorgio, P. D., & Amyot, M. (2025). Drivers and riverine fluxes of rare earth elements to coastal ecosystems across temperate, boreal, and subarctic ecoregions in Eastern Canada. *Environmental Science: Processes & Impacts*, *27*(9), 2740–2754. https://doi.org/10.1039/D5EM00391A

Landy, J. C., Ehn, J. K., Babb, D. G., Thériault, N., & Barber, D. G. (2017). Sea ice thickness in the Eastern Canadian Arctic: Hudson Bay Complex & Baffin Bay. *Remote Sensing of Environment*, *200*, 281–294. https://doi.org/10.1016/j.rse.2017.08.019

Lueker, T., Dickson, A., & Keeling, C. (2000). Ocean pCO calculated from dissolved inorganic carbon, 2 alkalinity, and equations for K and K : validation based on 1 2 laboratory measurements of CO in gas and seawater at 2 equilibrium. *Marine Chemistry*, *70*, 105–119.

Markus, T., Stroeve, J. C., & Miller, J. (2009). Recent changes in Arctic sea ice melt onset, freezeup, and melt season length. *Journal of Geophysical Research: Oceans*, *114*(C12), 2009JC005436. https://doi.org/10.1029/2009JC005436

Martini, I. (1986). *Canadian Inland Seas* (1986th ed.). Elsevier.

Mathis, J., Cross, J., Evans, W., & Doney, S. (2015). Ocean Acidification in the Surface Waters of the Pacific-Arctic Boundary Regions. *Oceanography*, *25*(2), 122–135. https://doi.org/10.5670/oceanog.2015.36

McGuire, A. D., Anderson, L. G., Christensen, T. R., Dallimore, S., Guo, L., Hayes, D. J., Heimann, M., Lorenson, T. D., Macdonald, R. W., & Roulet, N. (2009). Sensitivity of the carbon cycle in the Arctic to climate change. *Ecological Monographs*, *79*(4), 523–555. https://doi.org/10.1890/08-2025.1

Millero, F. J. (2010). Carbonate constants for estuarine waters. *Marine and Freshwater Research*, *61*(2), 139–142. https://doi.org/10.1071/MF09254

Mosley, L. M., Husheer, S. L. G., & Hunter, K. A. (2004). Spectrophotometric pH measurement in estuaries using thymol blue and m-cresol purple. *Marine Chemistry*, *91*(1–4), 175–186. https://doi.org/10.1016/j.marchem.2004.06.008

Mundy, C. J., Gosselin, M., Starr, M., & Michelc, C. (2010). Riverine export and the effects of circulation on dissolved organic carbon in the Hudson Bay system, Canada. *Limnology and Oceanography*, *55*(1), 315–323. https://doi.org/10.4319/lo.2010.55.1.0315

Mundy, C. J., Yezhova, Y., & Lengsavath, K. (2024). *RV William Kennedy Cruise Report July 31–September 1, 2023*. Centre for Earth Observation Science (CEOS).

Nielsen, D. M., Chegini, F., Maerz, J., Brune, S., Mathis, M., Dobrynin, M., Baehr, J., Brovkin, V., & Ilyina, T. (2024). Reduced Arctic Ocean CO2 uptake due to coastal permafrost erosion. *Nature Climate Change*, *14*(9), 968–975. https://doi.org/10.1038/s41558-024-02074-3

Niemi, A., Bednaršek, N., Michel, C., Feely, R. A., Williams, W., Azetsu-Scott, K., Walkusz, W., & Reist, J. D. (2021). Biological Impact of Ocean Acidification in the Canadian Arctic: Widespread Severe Pteropod Shell Dissolution in Amundsen Gulf. *Frontiers in Marine Science*, *8*, 600184. https://doi.org/10.3389/fmars.2021.600184

Orr, J. C., Fabry, V. J., Aumont, O., Bopp, L., Doney, S. C., Feely, R. A., Gnanadesikan, A., Gruber, N., Ishida, A., Joos, F., Key, R. M., Lindsay, K., Maier-Reimer, E., Matear, R., Monfray, P., Mouchet, A., Najjar, R. G., Plattner, G.-K., Rodgers, K. B., … Yool, A. (2005). Anthropogenic ocean acidification over the twenty-first century and its impact on calcifying organisms. *Nature*, *437*(7059), 681–686. https://doi.org/10.1038/nature04095

Ostlund, H. G., & Hut, G. (1984). Arctic Ocean Water Mass Balance from Isotope Data. *Journal of Geophysical Research*, *89*(C4), 6373–6381. https://doi.org/10.1029/JC089iC04p06373

Packalen, M. S., Finkelstein, S. A., & McLaughlin, J. W. (2014). Carbon storage and potential methane production in the Hudson Bay Lowlands since mid-Holocene peat initiation. *Nature Communications*, *5*. https://doi.org/10.1038/ncomms5078

Prinsenberg, S. J. (1978). *Analytical Study of the Circulation of James Bay* (Manuscript Report Series). Fisheries and Environment Canada.

Prinsenberg, S. J. (1984). Freshwater contents and heat budgets of James Bay and Hudson Bay. *Continental Shelf Research*, *3*(2), 191–200.

Prinsenberg, S. J. (1986). Chapter 9 Salinity and Temperature Distributions of Hudson Bay and James Bay. In *Elsevier Oceanography Series* (Vol. 44, pp. 163–186). Elsevier. https://doi.org/10.1016/S0422-9894(08)70902-4

Ridenour, N. A., Hu, X., Sydor, K., Myers, P. G., & Barber, D. G. (2019). Revisiting the Circulation of Hudson Bay: Evidence for a Seasonal Pattern. *Geophysical Research Letters*, *46*(7), 3891–3899. https://doi.org/10.1029/2019GL082344

Schlitzer, R. (2023). *Ocean Data View* [Computer software]. odv.awi.de

Schuur, E. A. G., McGuire, A. D., Schädel, C., Grosse, G., Harden, J. W., Hayes, D. J., Hugelius, G., Koven, C. D., Kuhry, P., Lawrence, D. M., Natali, S. M., Olefeldt, D., Romanovsky, V. E., Schaefer, K., Turetsky, M. R., Treat, C. C., & Vonk, J. E. (2015). Climate change and the permafrost carbon feedback. *Nature*, *520*(7546), 171–179. https://doi.org/10.1038/nature14338

Soriot, C., Stroeve, J., & Crawford, A. (2025). Record Early Sea Ice Loss in Southeastern Hudson Bay in Spring 2024. *Geophysical Research Letters*, *52*(4), e2024GL112584. https://doi.org/10.1029/2024GL112584

Stadnyk, T. A., Tefs, A., Broesky, M., Déry, S. J., Myers, P. G., Ridenour, N. A., Koenig, K., Vonderbank, L., & Gustafsson, D. (2021). Changing freshwater contributions to the Arctic. *Elementa: Science of the Anthropocene*, *9*(1), 00098. https://doi.org/10.1525/elementa.2020.00098

Steinacher, M., Joos, F., Frölicher, T. L., Plattner, G.-K., & Doney, S. C. (2009). Imminent ocean acidification in the Arctic projected with the NCAR global coupled carbon cycle-climate model. *Biogeosciences*, *6*(4), 515–533. https://doi.org/10.5194/bg-6-515-2009

Steiner, N., Azetsu-Scott, K., Hamilton, J., Hedges, K., Hu, X., Janjua, M. Y., Lavoie, D., Loder, J., Melling, H., Merzouk, A., Perrie, W., Peterson, I., Scarratt, M., Sou, T., & Tallmann, R. (2015). Observed trends and climate projections affecting marine ecosystems in the Canadian Arctic. *Environmental Reviews*, *23*(2), 191–239. https://doi.org/10.1139/er-2014-0066

Tank, S. E., Raymond, P. A., Striegl, R. G., McClelland, J. W., Holmes, R. M., Fiske, G. J., & Peterson, B. J. (2012). A land-to-ocean perspective on the magnitude, source and implication of DIC flux from major Arctic rivers to the Arctic Ocean. *Global Biogeochemical Cycles*, *26*(4). https://doi.org/10.1029/2011GB004192

Terhaar, J., Torres, O., Bourgeois, T., & Kwiatkowski, L. (2021). Arctic Ocean acidification over the 21st century co-driven by anthropogenic carbon increases and freshening in the CMIP6

model ensemble. *Biogeosciences*, *18*(6), 2221–2240. https://doi.org/10.5194/bg-18-2221-2021

Vonk, J. E., Fritz, M., Speetjens, N. J., Babin, M., Bartsch, A., Basso, L. S., Bröder, L., Göckede, M., Gustafsson, Ö., Hugelius, G., Irrgang, A. M., Juhls, B., Kuhn, M. A., Lantuit, H., Manizza, M., Martens, J., O'Regan, M., Suslova, A., Tank, S. E., … Zolkos, S. (2025). The land–ocean Arctic carbon cycle. *Nature Reviews Earth & Environment*, *6*(2), 86–105. https://doi.org/10.1038/s43017-024-00627-w

Vonk, J. E., & Gustafsson, Ö. (2013). Permafrost-Carbon Complexities. *Nature Geoscience*, *6*, 675–676.

Waldbusser, G. G., Hales, B., Langdon, C. J., Haley, B. A., Schrader, P., Brunner, E. L., Gray, M. W., Miller, C. A., & Gimenez, I. (2015). Saturation-state sensitivity of marine bivalve larvae to ocean acidification. *Nature Climate Change*, *5*(3), 273–280. https://doi.org/10.1038/nclimate2479

Waldbusser, G. G., & Salisbury, J. E. (2014). Ocean Acidification in the Coastal Zone from an Organism's Perspective: Multiple System Parameters, Frequency Domains, and Habitats. *Annual Review of Marine Science*, *6*(1), 221–247. https://doi.org/10.1146/annurev-marine-121211-172238

Wickham, H., Averick, M., Bryan, J., Chang, W., McGowan, L., François, R., Grolemund, G., Hayes, A., Henry, L., Hester, J., Kuhn, M., Pedersen, T., Miller, E., Bache, S., Müller, K., Ooms, J., Robinson, D., Seidel, D., Spinu, V., … Yutani, H. (2019). Welcome to the Tidyverse. *Journal of Open Source Software*, *4*(43), 1686. https://doi.org/10.21105/joss.01686

Yamamoto-Kawai, M., Tanaka, N., & Pivovarov, S. (2005). Freshwater and brine behaviors in the Arctic Ocean deduced from historical data of δ^{18} O and alkalinity (1929–2002 A.D.). *Journal of Geophysical Research: Oceans*, *110*(C10), 2004JC002793. https://doi.org/10.1029/2004JC002793

Zeebe, R. E., & Wolf-Gladrow, D. (2001). *CO_2 in seawater: Equilibrium, Kinetics, Isotopes* (D. Halpern, Ed.). Elsevier.

Zhang, Y., Yamamoto-Kawai, M., & Williams, W. J. (2020). Two Decades of Ocean Acidification in the Surface Waters of the Beaufort Gyre, Arctic Ocean: Effects of Sea Ice Melt and Retreat From 1997–2016. *Geophysical Research Letters*, *47*(3), e60119. https://doi.org/10.1029/2019GL086421

Chapter 5: Summary and Conclusions

Hudson Bay and James Bay are at the forefront of climate change with the global rise in atmospheric CO_2 concentrations having led to increased water temperatures, permafrost thaw, and increased rates of coastal erosion. Motivated by our lack of understanding of the James Bay carbonate system, this thesis sought to identify the dominant physical and biogeochemical controls of carbon cycling within this sub-Arctic sea. This thesis provides new insights into how freshwater inputs, carbon cycling, and air–sea gas exchange shapes the carbonate system of James Bay and Southern Hudson Bay by combining existing Hudson Bay carbonate system data with three years of new data collected across James Bay.

5.1. Summary of Major Contributions

The first research paper titled *CO_2 evasion from a shallow sub-arctic sea during August (2021 – 2023)* (chapter 3), focused on the distribution of surface water pCO_2 across southern Hudson Bay and James Bay, and the region's net air-sea CO_2 exchange (flux) budget. Our surface water pCO_2 observations demonstrated strong spatial variability in surface pCO_2 driven by local processes. While freshwater input and biological processes (respiration, primary production) were responsible for considerable variation in surface water pCO_2, the physical conditions (temperature) contributed to the bulk of the pCO_2 variability in James Bay and Southern Hudson Bay. Additionally, biological process and tidal mixing were identified as important drivers of surface water pCO_2 surrounding the Belcher Islands in Southern Hudson Bay. Air–sea CO_2 exchange calculations revealed that during the late summer study period, the region was a net source of CO_2 to the atmosphere in all three years visited, contrasting with what was observed in central Hudson Bay. Due to the regional, seasonal, and inter-annual variation in discharge from large rivers locally draining into southern Hudson Bay and James Bay and associated variation in the delivery of terrestrial carbon, continued monitoring of pCO_2 is necessary to adequately capture the impacts of on-going climate change on pCO_2 and the systems CO_2 source (or sink) status. This work highlights the importance of including seasonally and regionally extensive observations when assessing the role of coastal seas in the global carbon cycle.

The second research paper titled *Riverine controls on widespread carbonate mineral undersaturation in James Bay* (Chapter 4), examined the distribution and controls on key carbonate system variables including pH, total alkalinity (TA), dissolved inorganic carbon (DIC), and the saturation state (Ω) of carbonate minerals aragonite and calcite (Ω_{Arag} and Ω_{Cal}). Using TA and DIC to calculate other ocean carbonate system variables, this study documented low ocean pH (< 7.9) and low saturation state for aragonite and calcite, particularly aragonite, which was observed to be largely undersaturated (mean Ω_{Arag} of 0.88). Notably, this work presents the first observations of surface water aragonite undersaturation in James Bay during late summer.

The prevalence of $\Omega_{Arag} < 1$ in surface waters in James Bay was greater than observed in southern Hudson Bay; this is an important indicator of ecosystem health for calcifying organisms who use aragonite (and calcite) to form their hard structures. These potentially corrosive conditions were attributed to significant inputs of low alkalinity river water relative to the James Bay basin size, which reduced the capacity of seawater to buffer against the impacts of rising CO_2 concentrations. The watershed from which the freshwater originates strongly impacted the state of the carbonate system. Rivers draining the Hudon Bay Lowlands in western James Bay had higher total alkalinity and more basic pH (> 7), whereas rivers draining into eastern James Bay were more acidic pH (< 7), with considerably lower total alkalinity. The differences in calcium carbonate saturation state may result in differences in biological communities of calcifying organisms between the two bays. A potential consequence of observed carbonate undersaturation ($\Omega < 1$) is further enhanced corrosive conditions as warming and CO_2 uptake continues. Future increases in temperature, river discharge, and accompanied load of terrestrial carbon from the peatland dominated surrounding watersheds may further decrease the saturation state, endangering the local ecosystems. This study extends observations of carbonate system parameters to new sub-Arctic coastal environments; as climate change progresses, these sub-arctic ecosystems will be the bellwethers of change informing predictions for regions even further north. Therefore, a detailed understanding of the James Bay carbonate system will also provide valuable insight into future change across the Arctic Ocean.

5.2. Limitations and Recommendations for future work

While this thesis provided novel and useful insights into carbon cycling in sub-Arctic seas, it was not without limitations. Foremost, as sampling was conducted by ship, observations were only collected in August in each of the three years, limiting insights to the summer (ice free) conditions only. Although the three-year dataset provides a robust estimation of southern Hudson Bay and James Bay's carbonate system in the summer, seasonal processes such as sea ice formation and retreat, brine rejection, and the influence of peak runoff in the early spring are not captured in this dataset. As these processes are known to influence carbon sources and sinks in marine systems, an examination is incomplete without a complete open water season study. Another limitation of this study was due to the shallow nature of the region. Near-shore oceanographic sampling poses significant challenges; in particular, access to the shallow waters of James Bay is limited. For vessels as large as the *RV William Kennedy*, observations in the shallow shelf are impossible, particularly the western shore of James Bay. Additionally, the 'best practices' for carbonate system oceanography were developed for open ocean research. As previously stated, standard methodology for the determination of DIC and TA are intended to suit higher inorganic carbon concentrations. While these operating procedures have been used for Arctic research in the past, the low salinity of James Bay estuaries posed challenges for TA

determination. Additionally, the low temperature and salinity observed in James Bay also impacts the stoichiometric equilibrium constants, thus selecting the proper K_1^* and K_2^* definitions is imperative for accurate calculations. Millero (2010)'s equilibrium constant definitions were used within this study to best represent the range and salinity of the dataset. While this formulation is applicable for most of the dataset, our least saline samples were fresher than the salinity limit of the Millero (2010) constants. Thus, the use of the Dickson et al. (2007) standard operating procedures in estuarian environments introduces uncertainty to our results.

Overall, future studies examining the carbonate system of southern Hudson Bay and James Bay should seek to build on this work by prioritizing year-round observations to capture the full variability of the carbonate system's seasonal patterns. Additionally, future studies should seek to connect the marine carbonate system with biological impacts spatially across the nearshore and off-shore environments providing a land-ocean carbon cycle assessment, complete with implications on ecosystem processes including food web structure. With respect to the carbonate system, future work should seek to develop a set of standard methodologies for estuary carbonate system sampling and calculation. Finally, integrating observational datasets with regional biogeochemical models will enable improved projections of how continued climate warming and hydrological change will affect the region's carbonate system.

5.3. Closing Comments

This thesis provides the first comprehensive, multi-year, late-summer assessment of the carbonate system and carbonate mineral saturation state in southern Hudson Bay and James Bay. Through documenting air-sea CO_2 exchange and freshwater-driven carbonate mineral undersaturation, this work underscores the vulnerability of sub-Arctic coastal waters to ongoing environmental change. These findings fill a critical regional knowledge gap and also contribute to a broader understanding of how high-latitude coastal systems respond to increasing atmospheric anthropogenic CO_2, with implications for both marine ecosystems and global carbon cycling.

Appendix A: Contributions of Collaborating Authors

Chapters 3 and 4 have the same authorship, with identical contributions to the respective chapters. All work was analyzed, written, and edited by N. Decker under the supervision of Drs. K. Brown and T. Papakyriakou. The original draft of both manuscripts was conceptualized by N. Decker and refined by Drs. K. Brown and T. Papakyriakou. Data collection for both chapters was performed by K. Yezhova in 2021 and both K. Yezhova and N. Decker in 2022 and 2023. 2021 sample analysis was performed by K. Yezhova under the supervision of Dr. K. Azetsu-Scott at Fisheries and Oceans Canada Bedford Institute of Oceanography. 2022 and 2023 sample analysis was performed by N. Decker under the supervision of Dr. D. Capelle. Conceptualization, project design, and initial funding requests were performed by Drs. Z. Kuzyk, C.J. Mundy, and T. Papakyriakou. All authors have read and contributed comments to this thesis.

Appendix B: Supplemental Figures for CO_2 evasion from a shallow sub-arctic sea during August (2021-2023)

Table B.1: Total Uncertainty associated with pCO_2 measurements. Sources of uncertainty include instrument error and the error associated with the TSG's temperature correction. Note: mean pCO_2 values deviate from results table as TSG data was synced with CTD data.

Year	Mean pCO_2 (µatm)	Instrument Error (µatm)	Temperature Correction Error (µatm)	Temperature Correction Error (%)	Total Error (µatm)	Total Relative Error (%)
2021	471.20	5	4.91	1.04	7.01	1.49
2022	446.99	5	15.86	3.55	16.63	3.72
2023	470.26	5	3.25	0.69	5.96	1.27

Table B.2: Interpretation of PPMCC results, per Asuero et al. (2006).

Strength of Correlation	
r	*Interpretation*
0.00 to 0.29	Little to no correlation
0.30 to 0.49	Low correlation
0.50 to 0.69	Moderate correlation
0.70 to 0.89	High correlation
0.90 to 1.00	Very high to perfect correlation

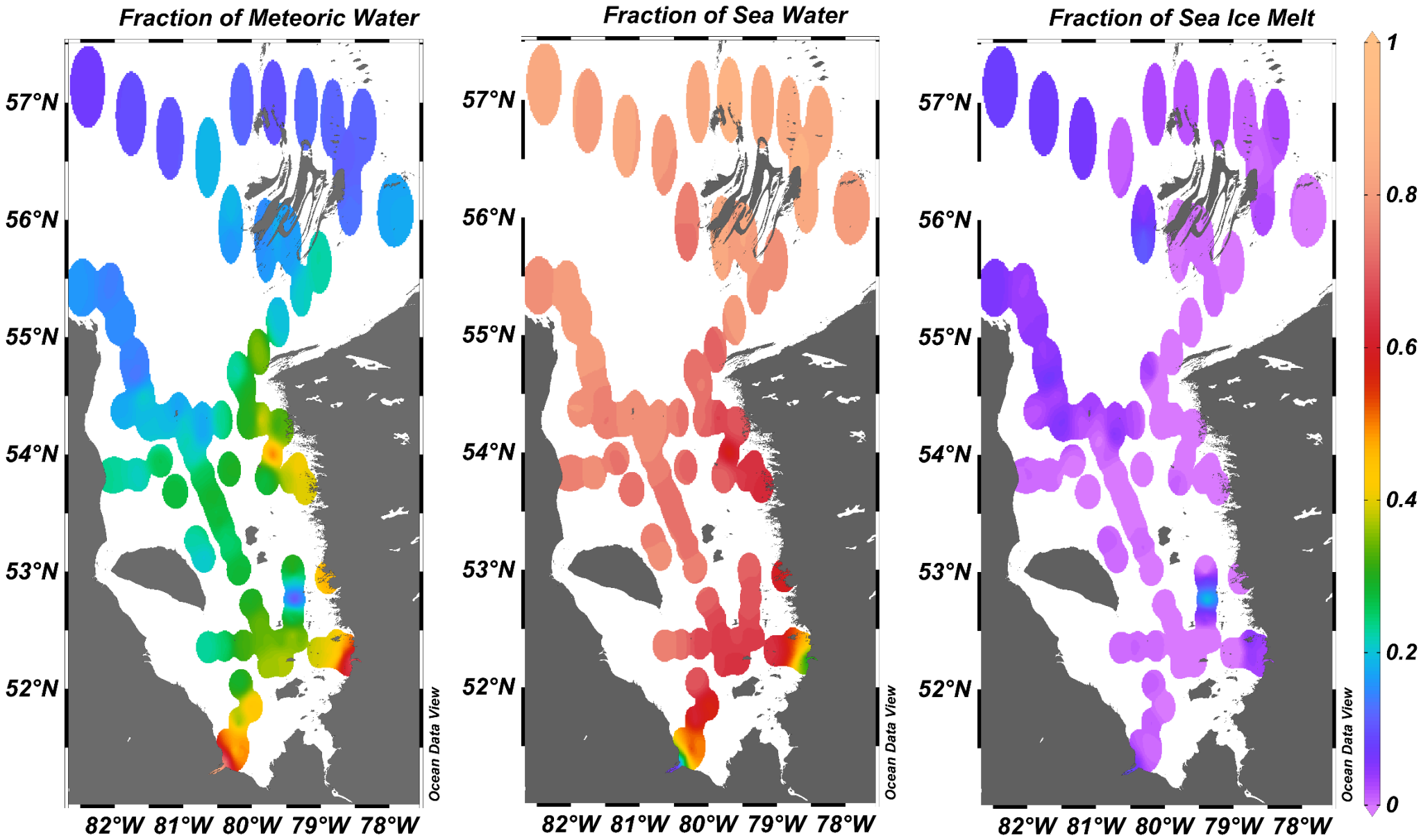

Figure B.1: Estimated surface water composition using a three end-member mixing model. Endmembers used are summarized within Table 1.

Table B.3: ANOVA Post Hoc test (Tukey HSD) results. Bold rows are statistically different differences.

Tukey HSD Post-hoc Comparisons for CO_2

			95% Confidence Interval		
	Comparison	Mean Difference (µatm)	Lower CI	Upper CI	Adj. p
Region (all years)	**SHB-JB**	**−38.6**	**−40.5**	**−36.8**	**0.00**
	JB-BI	**31.3**	**29.5**	**33.0**	**0.00**
	SHB-BI	**−7.3**	**−9.3**	**−5.4**	**0.00**
Within Region over Years	**BI 2022–2023**	**−50.9**	**−54.4**	**−47.4**	**0.00**
	SHB 2022–2023	**−47.6**	**−52.0**	**−43.1**	**0.00**
	JB 2021–2023	**−33.4**	**−38.2**	**−28.5**	**0.00**
	SHB 2021–2023	**−30.9**	**−35.6**	**−26.3**	**0.00**
	JB 2022–2023	**−18.2**	**−22.6**	**−13.9**	**0.00**
	SHB 2021–2022	**16.7**	**11.8**	**21.5**	**0.00**
	JB 2021–2022	**−15.2**	**−18.8**	**−11.5**	**0.00**
Within Year across Regions	**2022 SHB–JB**	**−63.2**	**−67.1**	**−59.3**	**0.00**
	2022 JB–BI	**62.5**	**59.1**	**66.0**	**0.00**
	2023 SHB–JB	**−33.8**	**−38.7**	**−28.9**	**0.00**
	2021 SHB–JB	**−31.3**	**−36.0**	**−26.7**	**0.00**
	2023 JB–BI	**29.9**	**25.4**	**34.3**	**0.00**
	2023 SHB–BI	**−3.9**	**−7.7**	**−0.2**	**0.03**
	2022 SHB–BI	−0.6	−4.9	3.6	1.00
Year (all regions)	**2023-2022**	**34.6**	**33.0**	**36.3**	**0.00**
	2023-2021	**32.5**	**30.4**	**34.7**	**0.00**
	2022-2021	**−2.1**	**−4.1**	**0.0**	**0.05**

Bold = significant ($p < 0.05$).

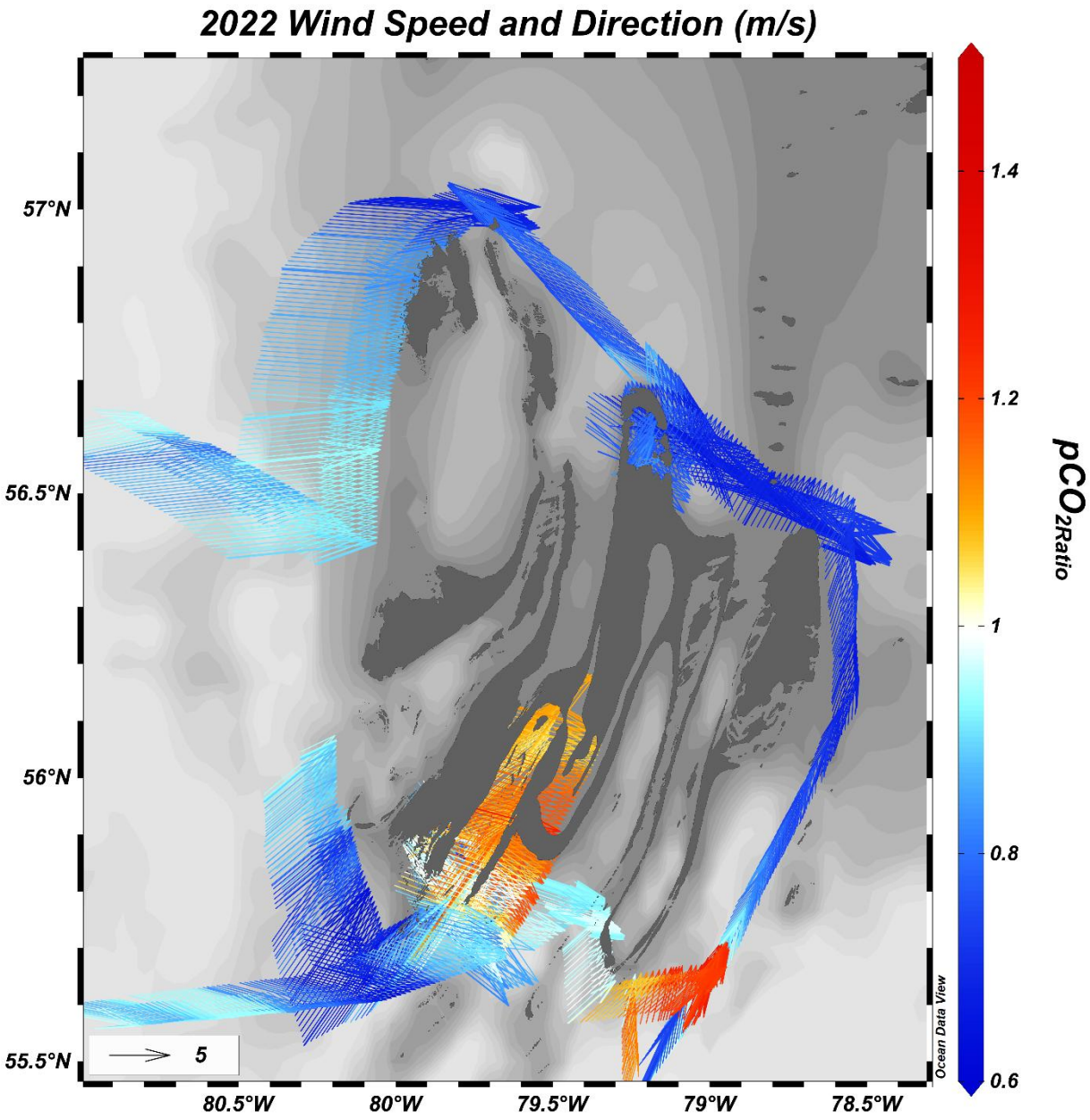

Figure B.2: Wind speed and direction during the 2022 cruise, in m/s. Arrow direction indicates wind direction, arrow size indicates wind speed, and arrow colour is pCO_{2Ratio}. Upwelling occurs 90 degrees from wind direction.

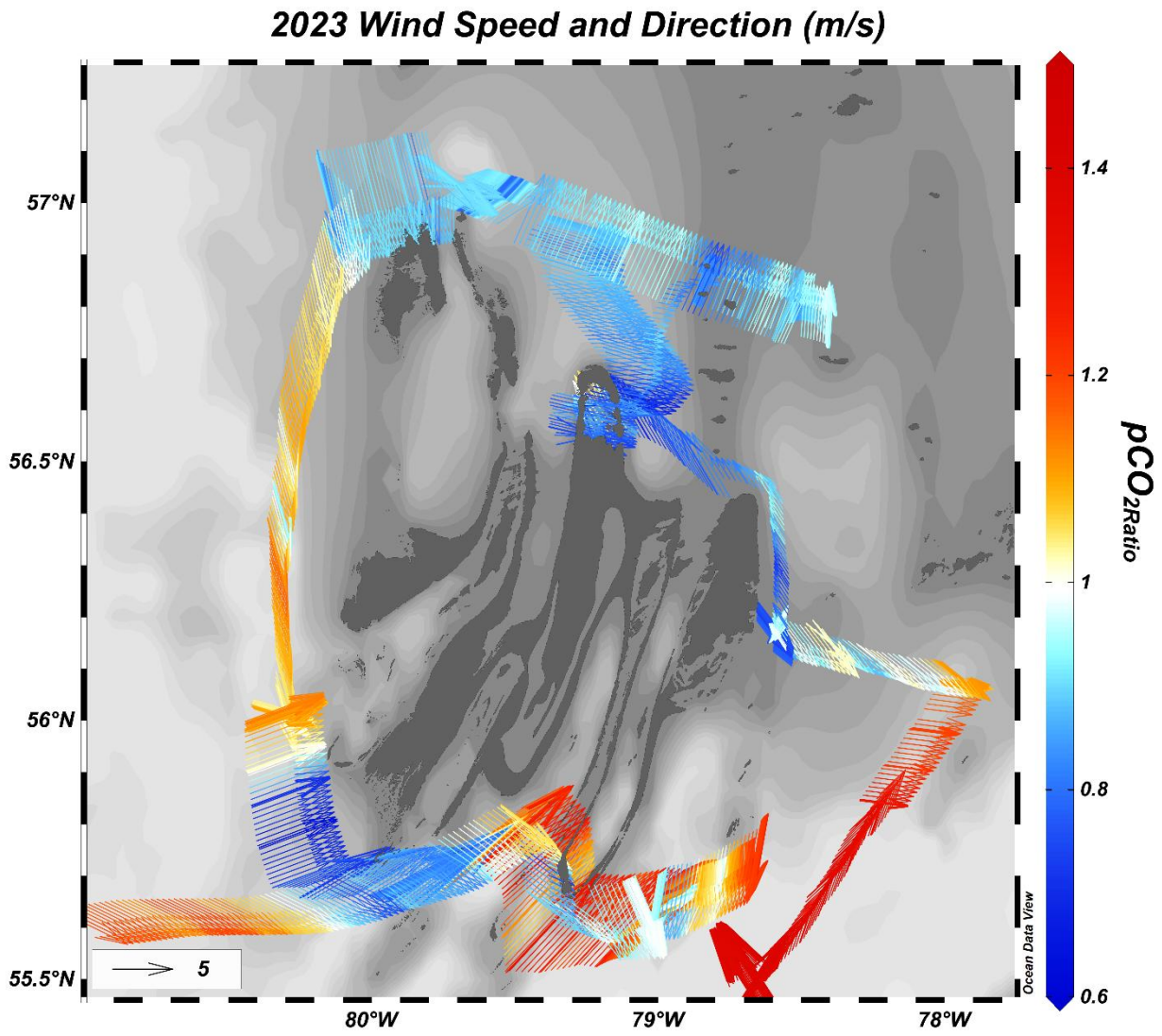

Figure B.3: Wind speed and direction during the 2023 cruise, in m/s. Arrow direction indicates wind direction, arrow size indicates wind speed, and arrow colour is pCO_{2Ratio}. Upwelling occurs 90 degrees from wind direction.

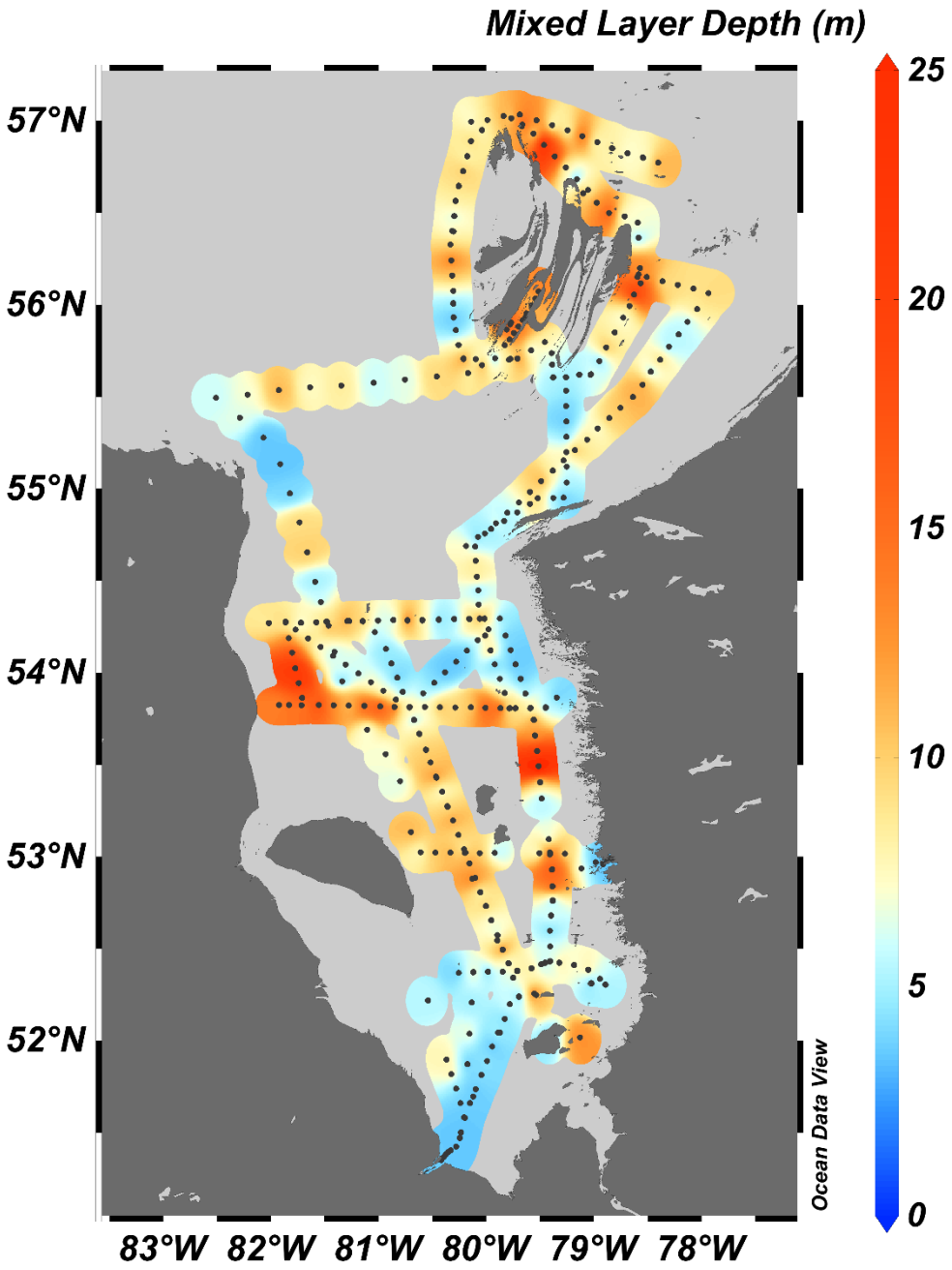

Figure B.4: Mixed layer depth in meters. Mixed layer depth was estimated in ODV. The depth of the maximum Brunt-Visala frequency was used as the bottom of the mixed layer.

Appendix C: Supplemental Figures for *Riverine controls on widespread carbonate mineral undersaturation in James Bay*

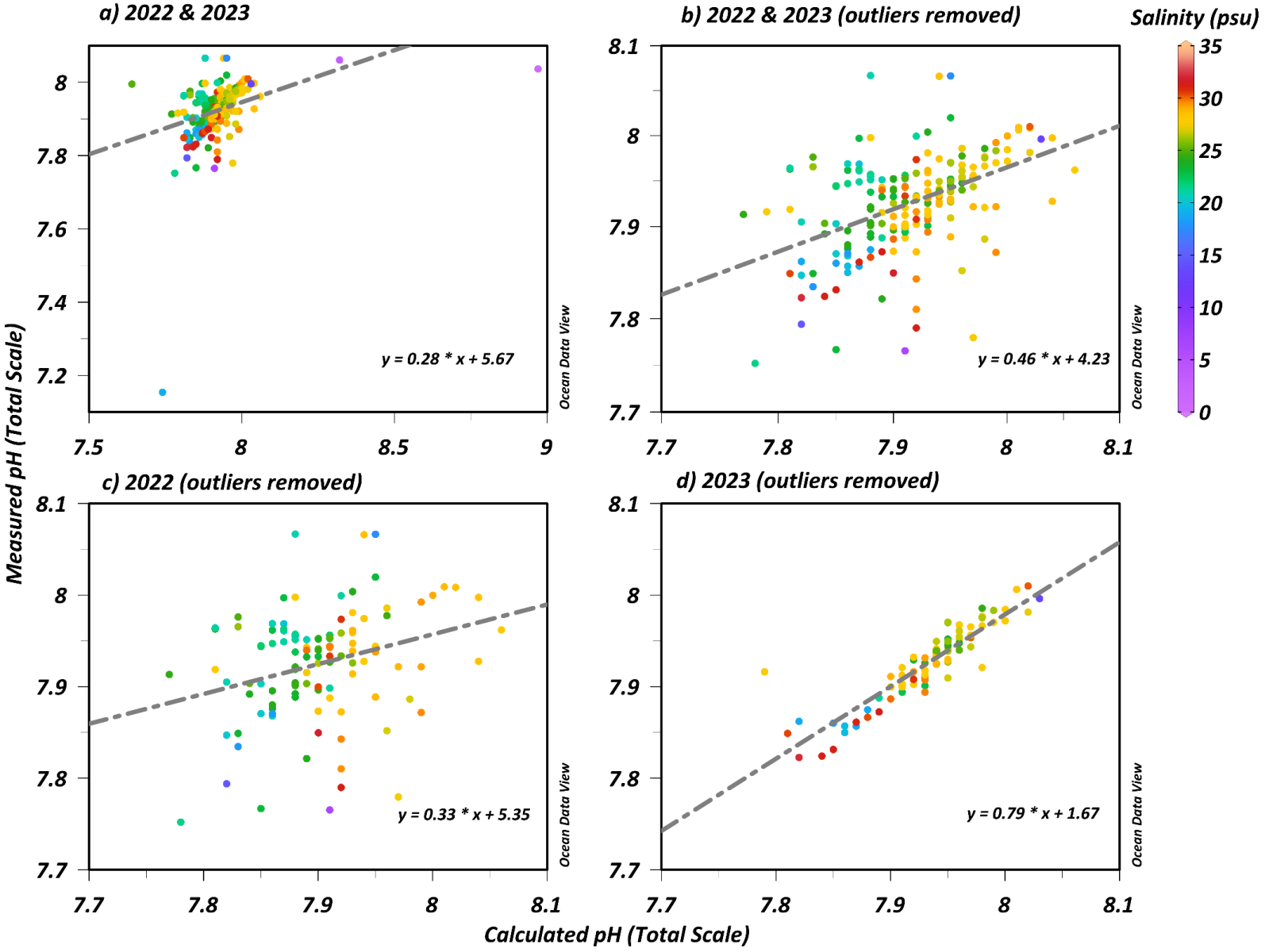

Supplemental Figure C.1: (a) Calculated pH vs measured pH, all points; (b) Calculated pH vs measured pH, outliers removed; (c) Calculated pH vs measured pH using the electrode and reference cell, 2022 (d) Calculated pH vs measured pH using the spectrophotometer, 2023

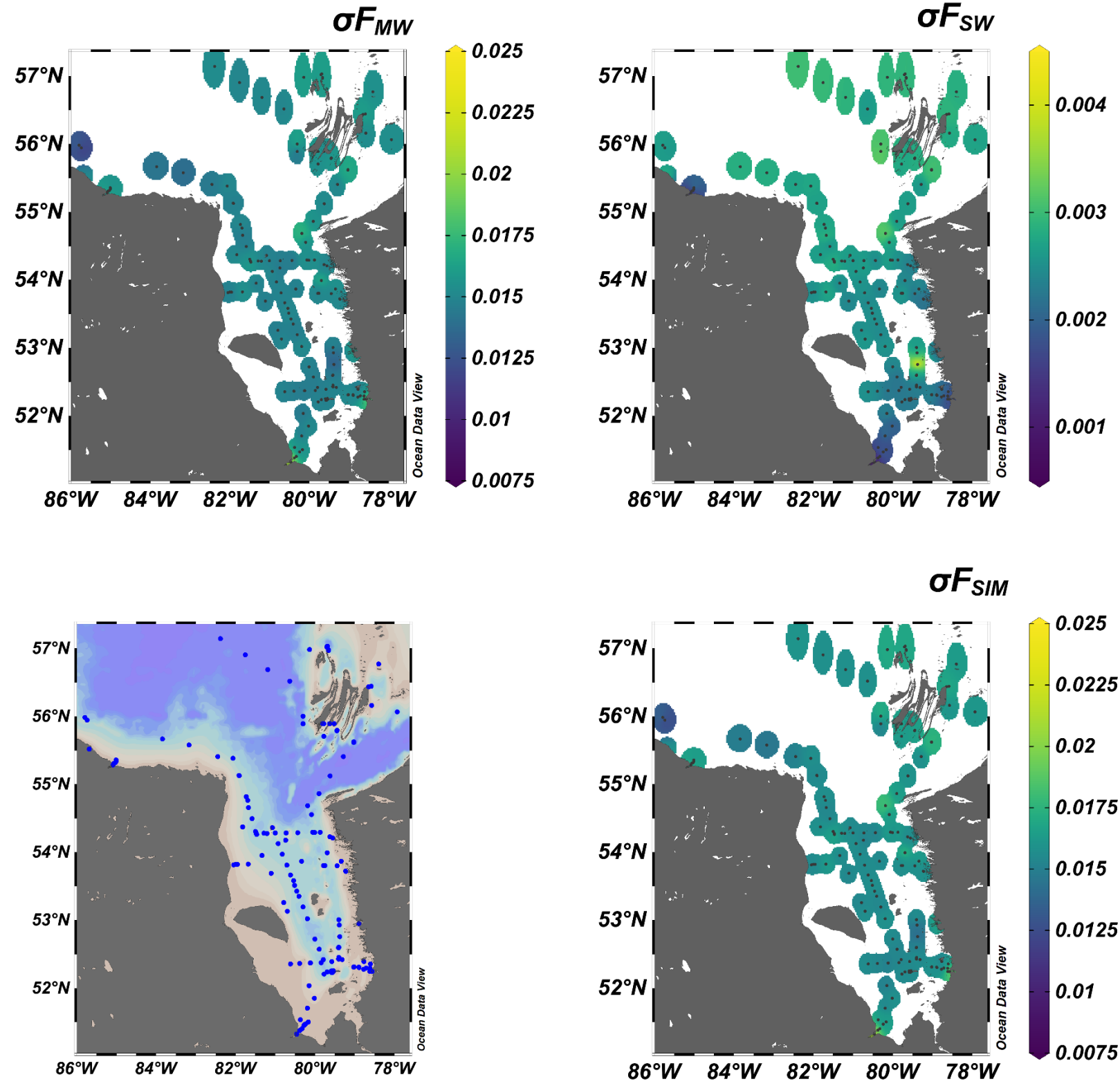

Supplemental Figure C.2: Standard deviations (σ) of surface water mass fractions from Monte Carlo uncertainty analysis. Standard deviations represent the absolute uncertainty of a given water mass fraction (means: $\sigma_{sw} = 0.01$; $\sigma_{mw} = 0.02$; $\sigma_{sim} = 0.02$).

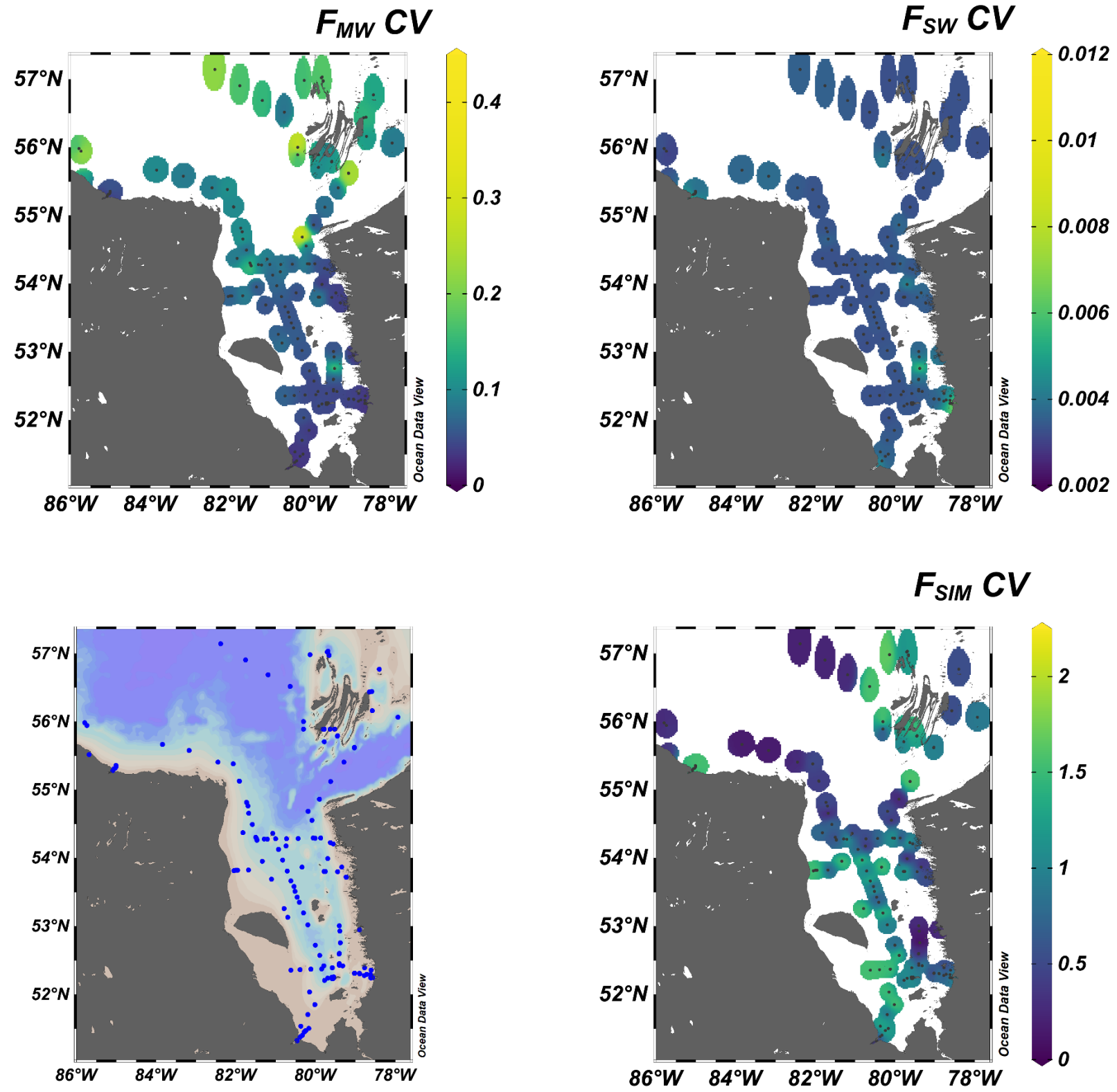

Supplemental Figure C.3: Coefficient of variation (CV = σ/mean) of surface water mass fractions from Monte Carlo uncertainty analysis. CV represents the relative uncertainty of a calculated water mass fraction (means: CV F_{sw} = 0.01; CV F_{mw} = 0.10; CV F_{sim} = 0.90).

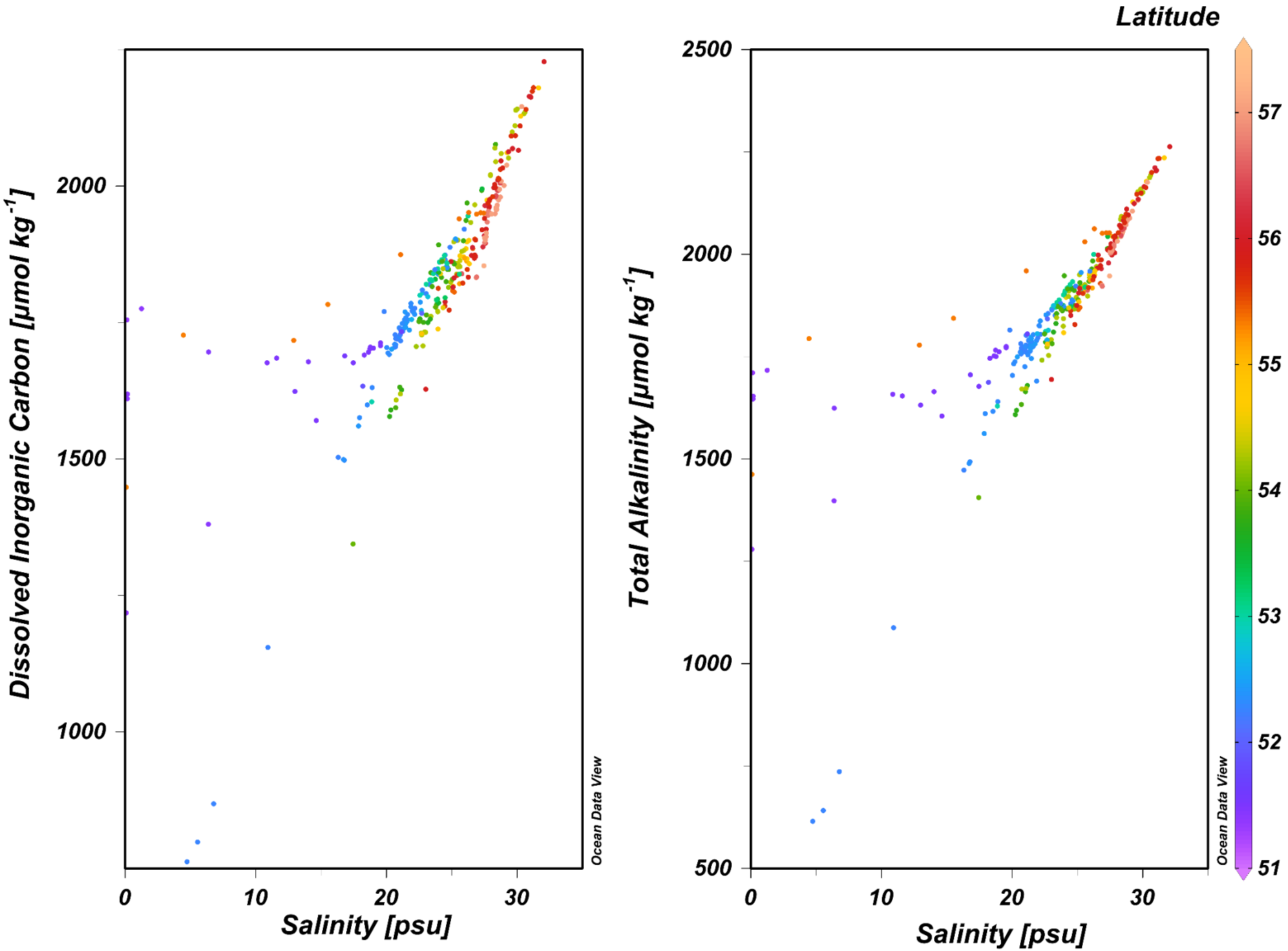

Supplemental Figure C.4:
(a) relationship between salinity and total alkalinity,
(b) relationship between salinity and dissolved inorganic carbon.
Both plots are coloured based on latitude.

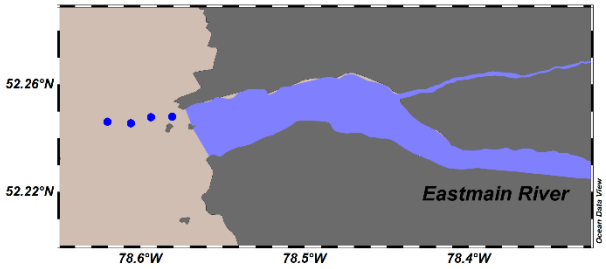

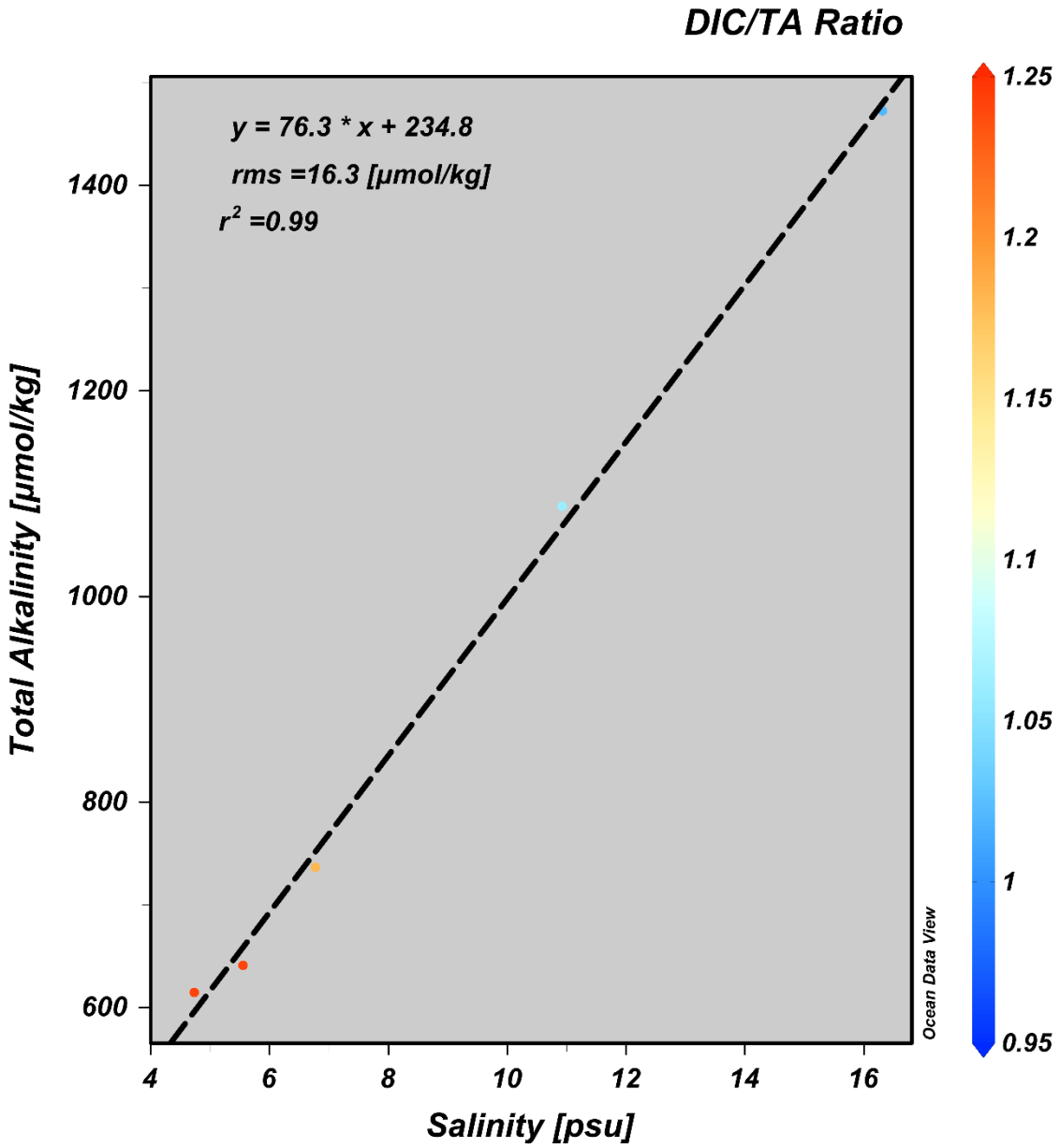

Supplemental Figure C.5: Linear regression model of Eastmain River estuary samples.

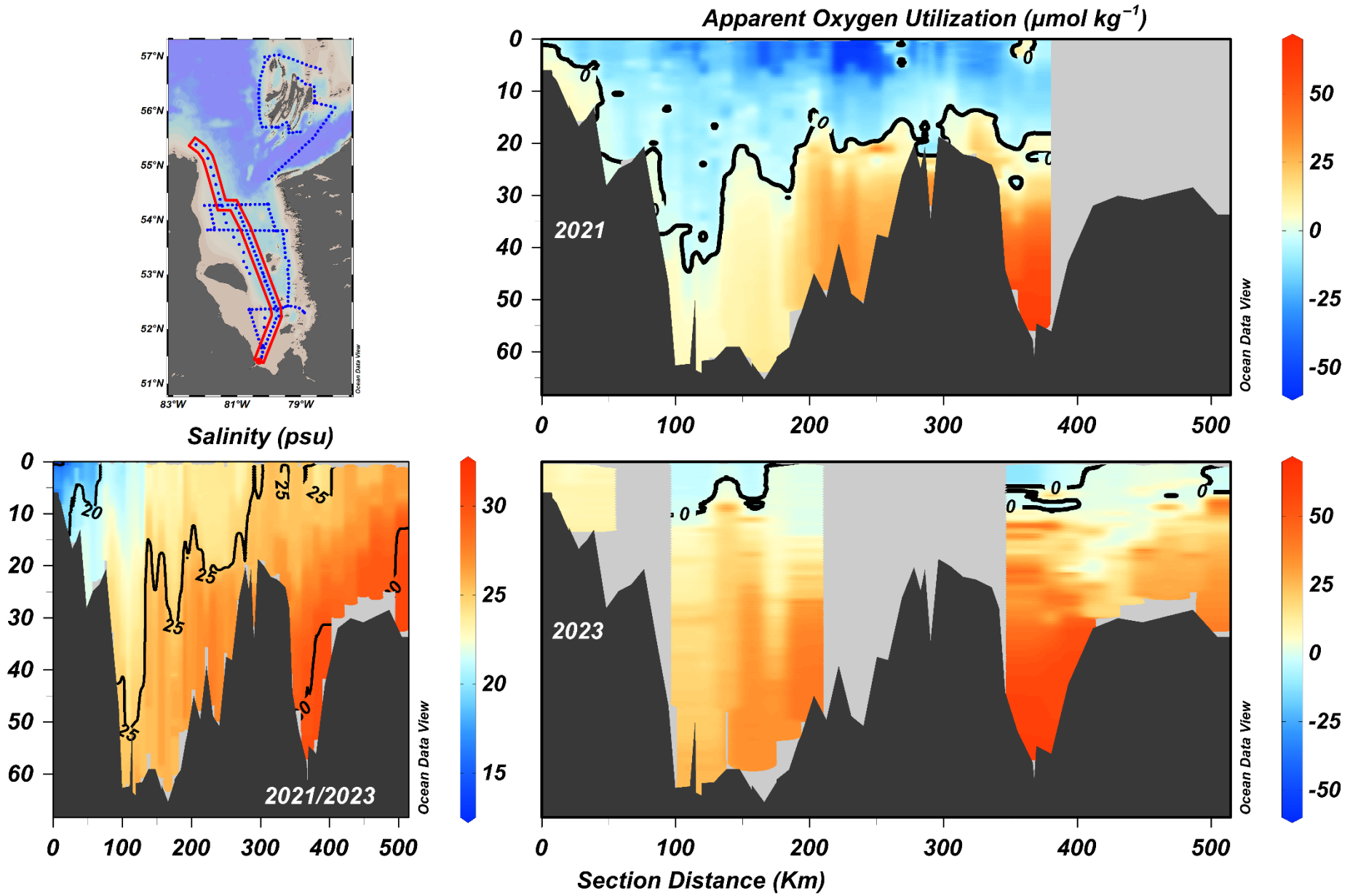

Supplemental Figure C.6: Apparent Oxygen Utilization as determined from CTD casts in 2021 & 2023. Data from JBE 2022 is excluded. Note, the transect begins (0 km) at the Moose River.